Stress-deformation analysis of Denis-Perron dam: verification and validation for better prediction of rockfill response

by

Boris Nikolaev Kolev

BEng, The University of Edinburgh, 2014

A THESIS SUBMITTED IN PARTIAL FULFILLMENT
OF THE REQUIREMENTS FOR THE DEGREE OF

MASTER OF APPLIED SCIENCE

in

THE FACULTY OF GRADUATE AND POSTDOCTORAL STUDIES
(Civil Engineering)

The University of British Columbia
(Vancouver)

April 2017

Abstract

Rockfill dams present a challenge for engineers due to the many uncertainties revolving around the behaviour of rockfill. A governing factor in the behaviour of rockfill is the particle breakage due to change of moisture, which was observed in laboratory and field conditions. Alonso and Oldecop have proposed a rockfill model (RM), where the suction inside the cracks of the rockfill is a state variable that controls the breakage mechanism. This research focuses on verification and validation of stress-deformation analysis methodologies, for better prediction of rockfill response. It involves application of the RM in numerical simulation of a benchmark case study on the well instrumented Denis-Perron dam (SM3). Denis-Perron dam is a rockfill dam with a central till core, 171 metres high and 378 metres long, located on the Sainte-Marquerite river in northern Quebec, Canada. The instrumentation data was made available by Hydro-Québec, for a period of six years of construction, impoundment, and operation of the dam. Numerical simulations are conducted using Code_Bright – a fully coupled three phase finite element program for unsaturated porous media. A validation stage was first carried out through modelling of Beliche dam – a well studied case by Alonso et al. The numerical model of the SM3 dam captures the staged construction, reservoir impoundment and rainfall history recorded. Model parameters for the till core and rockfill shoulders were either calibrated using limited available laboratory and field data, adopted from literature, or assumed with some rationale. Deformations measured by the inclinometers during construction and impoundment, both upstream and downstream, are simulated successfully. Piezometer and pressure cell measurements are replicated to a very good extent. Post-construction deformations are reproduced with reasonable success, given the limited data for detailed characterization of the various zones in the dam. Some important challenges around characterization of the rockfill compressibility and the related scaling issues for model calibration are presented and discussed. An attempt is made to quantify the amount of scaling observed through a back analysis of field measurements. Finally, the effect of permeability on rockfill in the development of deformations is discussed.

Preface

Early in 2015, Hydro-Québec invited the UBC Theoretical & Applied Geomechanics group to participate in a numerical analysis workshop that was to be held in parallel to the Sixty Eight Canadian Geotechnical Conference, in September 2015 in Québec, QC, Canada. The workshop was aimed to evaluate the state of the art on constitutive and numerical modeling of rockfill dams, and provide means for Verification & Validation of the numerical tools for better predictions. Contributing to this workshop shaped the beginning of this research project. The project was then continued beyond the workshop with interest and support from Hydro-Québec and the Natural Sciences & Engineering Research Council of Canada (NSERC).

The research was lead by my supervisor Professor Mahdi Taiebat. I, Boris Nikolaev Kolev, am the principle contributor to all seven chapters and two appendices of this thesis. My contribution to different elements of the project that lead to this thesis included i) studying the background information about the SM3 dam, ii) including the reports and data provided by Hydro-Québec, iii) learning about the fundamental aspects of response in rockfill materials, iv) getting familiar with the state of the art of constitutive modelling of rockfill material and numerical modelling of rockfill dams accounting for various stages of construction, reservoir impoundment, and rainfall history, v) verification of my modelling methodology by comparing my simulation of Beliche dam with the previous study by the group of Alonso at UPC in Spain, vi) detailed simulation of SM3 for various stages of construction and operation, vii) fine tuning the numerical model and material parameter calibration, viii) detailed comparison of the numerical results with the instrumentation data provided by Hydro-Québec, ix) sensitivity analyses on rockfill compressibility and permeability, and x) packaging and reporting the research outcomes.

Some outcomes of my thesis are published in form of a conference paper in Kolev et al. (2016). A more extensive journal paper is now in preparation covering various outcomes of this thesis.

Table of Contents

Abstract . . . . **ii**

Preface . . . . **iii**

Table of Contents . . . . **iv**

List of Tables . . . . **viii**

List of Figures . . . . **x**

Acknowledgements . . . . **xv**

1 Introduction **1**

1.1 Motivation 1

1.2 Goals 3

1.3 Thesis structure 3

2 Denis-Perron Dam – case description **5**

2.1 Project background 5

2.2 Field instruments 8

2.2.1 Inclinometers 9

2.2.2 Pressure cells 11

2.2.3 Observation terminals 13

2.2.4 Piezometers 14

2.3 Laboratory data 15

2.3.1 Central till core 15

2.3.2 Rockfill shells 17

2.4 Previous Denis-Perron dam analyses 19
2.4.1 Pre-construction FE analysis using a hyperbolic model (1990) 19
2.4.2 FE analysis using the Rockfill Model (2012) 22

3 Mechanical and hydraulic models used in the analysis of Denis-Perron 23
3.1 Introduction 23
3.2 Mechanical models 24
3.2.1 Barcelona basic model (BBM) 24
3.2.2 Rockfill compressibility model (RM) 30
3.3 Hydraulic models 38
3.3.1 Van Genuchten hydraulic model 38
3.3.2 Liquid phase relative permeability 39

4 Description of the numerical model 41
4.1 Finite element software 41
4.2 Geometry and zoning 41
4.2.1 Geometry and model layers 42
4.2.2 Constitutive models assigned to material zones 42
4.3 Material parameters 43
4.3.1 Till core 44
4.3.2 Rockfill material 48
4.3.3 Drain, filter and alluvial foundation 53
4.3.4 Bedrock, concrete and water 57
4.4 Initial and boundary conditions 58
4.4.1 Boundary conditions 59
4.4.2 Initial conditions 60
4.5 Time intervals 61
4.5.1 Construction stages 61
4.5.2 Impoundment stages 64
4.5.3 Rainfall stages 64
4.6 FE mesh 67
4.6.1 Mesh description 67
4.6.2 Mesh quality 68
4.7 Solution scheme 69

5 Base case simulation results . . . **71**
5.1 Introduction . . . 71
5.2 Pore water pressure . . . 72
5.2.1 General results . . . 72
5.2.2 Comparison with instrument data . . . 75
5.3 Degree of saturation . . . 76
5.3.1 General results . . . 76
5.4 Vertical total stress . . . 80
5.4.1 General results . . . 80
5.4.2 Comparison with instrument data . . . 82
5.5 Vertical displacements . . . 82
5.5.1 General results . . . 82
5.5.2 Comparison with instrument data . . . 84
5.6 Horizontal displacements . . . 86
5.6.1 General results . . . 86
5.6.2 Comparison with instrument data . . . 88
5.7 Summary . . . 88

6 Complementary simulations . . . **90**
6.1 Introduction . . . 90
6.2 Sensitivity analysis on rockfill compressibility . . . 90
6.2.1 Effect of particle scale on rockfill compressibility . . . 91
6.2.2 Simulation results . . . 91
6.2.3 Quantification of size effect . . . 94
6.3 Sensitivity analysis on rockfill permeability . . . 98
6.3.1 Simulation results . . . 98
6.3.2 Discussion . . . 98

7 Summary and future research . . . **102**
7.1 Summary of research . . . 102
7.2 Recommendations for future research . . . 103

Bibliography . . . **105**

A Validation Problem – Beliche dam simulation . . . 108
A.1 Problem information . . . 108
A.2 Simulation results comparison . . . 112
A.3 Simulation method differences . . . 114

B Rockfill mechanics . . . 115
B.1 Field and laboratory observations . . . 115
B.2 Particle breakage . . . 119
B.3 Testing apparatus . . . 124

List of Tables

Table 2.1 Available instruments along the whole body of the dam(Hammamjil, 2003). . . 8
Table 2.2 Till core dry density measurements (Péloquin, 2015). 17
Table 2.3 Results of triaxial permeability tests (Lafleur, 1998). 17
Table 2.4 Hyperbolic model material parameters for all dam zones. 20

Table 3.1 Summary of BBM parameters and calibration methods. 29
Table 3.2 Basic relationships for BBM and RM*. Table adopted from Alonso et al. (2005). 36
Table 3.3 Summary of RM parameters and calibration methods. 37

Table 4.1 Assigned constitutive models to dam zones. 43
Table 4.2 Comparison of H-06 glacial till material physical characteristics with SM3 glacial till material. 45
Table 4.3 Hydraulic parameters for the till core. 46
Table 4.4 Mechanical parameters for the till core. 49
Table 4.5 Hydraulic parameters for the rockfill shells. 51
Table 4.6 Mechanical parameters for the rockfill shells. 54
Table 4.7 Hydraulic parameters for the drain, filter and the alluvial foundation. 55
Table 4.8 Mechanical parameters for drain, filter and alluvial foundation. 56
Table 4.9 Hydraulic parameters for bedrock, concrete and water. 58
Table 4.10 Mechanical properties for bedrock, concrete and water. 59
Table 4.11 Description of time intervals details and impoundment boundary condition associated with each interval. 66
Table 4.12 Solution scheme data. 70

Table A.1 Mechanical parameters for rockfill. 110

Table A.2 Mechanical parameters for the till core. 111
Table A.3 Hydraulic parameters for rockfill, till core and foundation 112

List of Figures

Figure 1.1 Deformations durign operation of multiple rockfill dams. The numbers in brackets represent the height of the respective dam. Data obtained from Oldecop and Alonso (2013*a*). 2

Figure 2.1 Location of Denis-Perron 5
Figure 2.2 Aerial view of Denis-Perron Dam (Péloquin, 2015) 6
Figure 2.3 Analyzed cross section A-A of Denis-Perron dam (Péloquin, 2015). 7
Figure 2.4 Analyzed cross section A-A visualized in 2D. 7
Figure 2.5 Locations of upstream and downstream inclinometers INB1 and INB5, respectively. 9
Figure 2.6 Vertical settlement measurement for INB1 and INB5 during construction for end of time intervals [A] to [C]. 10
Figure 2.7 Vertical settlement measurement for INB1 and INB5 after construction for end of time intervals [D] to [F]. 11
Figure 2.8 Location of total pressure cells CPB 251 and CPB 255. 12
Figure 2.9 Total pressure cell measurements of CPB 251 and CPB 255, ... 12
Figure 2.10 Downstream horitonztal displacement gauges measurements of B0-28, B0-9 and B0-5. 13
Figure 2.11 Downstream vertical displacement gauges measurements of B0-28, B0-9 and B0-5. 13
Figure 2.12 Location of piezometer cells PPB 272, 302, 342 and 381. 14
Figure 2.13 Piezometer cells measurements for PPB 272, 302, 342 and 381. 15
Figure 2.14 Grain size distribtuion of the Denis-Perron till core material (Hammamjil (2003)) and the grain size distribution of a till sample from Northern Québec (dashed red line) (Watabe et al., 2000). 16

Figure 2.15 Oedometer rockfill data for dry and saturated samples (Errecalde, 2012). 18
Figure 2.16 (a) Grain size distribution of inner shell (b) Grain size distribution of outer shell (Hammamjil, 2003). 19
Figure 2.17 Contour plots of the simulation results for (a) Vertical displacements [m] (b) Horizontal displacements [m] (c) Vertical total stress [tonne/m^2] (d) Horizontal total stress [tonne/m^2]. 21
Figure 2.18 Vertical displacements at (a) Upstream inclinometer INB1 (b) Downstream inclinometer INB5 for different dates. Adapted from Errecalde (2012). 22

Figure 3.1 Strains assosiated with loading and suction changes in BBM. 25
Figure 3.2 The dimensional view of the BBM yield surfaces in (p,q,s) space. Adapted from Alonso et al. (1990). 25
Figure 3.3 (a) Representation of the S.I. and L.C. curve in (s,p) space (b) Compression curves in v,s,p space (c) Compression curves for saturated and unsaturated soils in v,p space (d) Compression curves in v,s space for BBM (Alonso et al., 1990). 27
Figure 3.4 (a) Idealized model response for different stress paths (b) Yield surface (L.C. curve) for different values of p_0^* for RM. 31
Figure 3.5 The dimensional view of the yield surfaces in (p,q,s) space for RM. 32
Figure 3.6 Water retetion curves with varying P_0 and λ_{van} parameters. 38
Figure 3.7 Varying relative permeability for clay and rockfill materials (Alonso et al., 2005). 40

Figure 4.1 Construction sequence of dam for model calculations. 42
Figure 4.2 Denis-Perron dam material zones. 43
Figure 4.3 (a) Standard Proctor compaction curve for all samples tested (b) Hydraulic conductivity as a function of the compaction degree of saturation. Figures modified from Watabe et al. (2000). 44
Figure 4.4 (a) Soil characteristic curves for till samples in Watabe et al. (2000). Red line shows an average curve. (b) Fitted curve (blue) to averaged soil characteristic curve using van Genuchten (1980). 46
Figure 4.5 Oedometer test on compacted till from Northern Quebec, sample H-06 (Watabe et al., 2000). 47
Figure 4.6 Water retention curves for rockfill material: Beliche Dam (Alonso et al. (2005)), Lechago Dam (Alonso et al. (2012)) and Denis-Perron Dam (Errecalde (2012)). 50

Figure 4.7 Oedometer test data and model results for wet ($S_r = 100\%$) and dry ($S_r = 30\%$) rockfill samples. 52
Figure 4.8 Calibration of parameters μ and β^c based on data from Figure B.8 (a). 53
Figure 4.9 Mechanical and hydrauilic boundary conditions. 60
Figure 4.10 Initial suction values for the material zones. 60
Figure 4.11 Initial porosity values for the material zones. 61
Figure 4.12 Construction sequence of the dam between 1996 and 1998 according to Péloquin (2015). 62
Figure 4.13 Dam construction and impoundment sequence in real life and the numerical model. 62
Figure 4.14 The average and standard deviation of critical parameters 63
Figure 4.15 Precipitation data recorded in the field. Data digitized from Hammamjil (2003). 65
Figure 4.16 Finite element mesh of Denis-Perron dam. 67
Figure 4.17 (a) Shape quality (b) Maximum edge cumulative distrobution. 68

Figure 5.1 Summary of instruments and selected monitoring points used in analysis of simulation results. 72
Figure 5.2 Evolution of: (a) Construction and impoundment sequence (b) Water pressure for upstream points B0-28, 1 and 2; (c) Water pressure for downstream points B0-9, 3 and 4: Base case. 73
Figure 5.3 (a) Porosity-Mean net stress (b) Suction-Mean net stress for rockfill shells. . . 75
Figure 5.4 Pore water pressures in the till core of the dam: comparison of measured and calculated values for base case. 76
Figure 5.5 (a) Construction and impoundment sequence. Evolution of degree of saturation for (b) upstream points A, 1 and 2; (c) downstream points C, 3 and 4: Base case. 78
Figure 5.6 Contour plots for degree saturation at (a) end of time [A] (b) end of time [C] (c) end of time [E] (d) end of time [F]. 79
Figure 5.7 Vertical stresses during construction and impoundment on a horizontal plane at elevation 60 m above the bottom boundary of till core for Times [A] to [F]. . 80
Figure 5.8 Contour plots for vertical total stress in MPa at (a) end of time [A] (b) end of time [C] (c) end of time [E] (d) end of time [F]. 81
Figure 5.9 Vertical stress in MPa at the bottom of the till core for points CPB 251 and CPB 255: comparison of measured and calculated values for base case. 82

Figure 5.10 Contour plots for vertical displacements (settlement) at (a) end of time [A] (b) end of time [C] (c) end of time [E] (d) end of time [F]. 83
Figure 5.11 Calculated and measured vertical settlement for inclinometers INB1 and INB5 after construction for stages [A] to [D]: base case. Elevation 260 corresponds to bottom of the rockfill shell. 85
Figure 5.12 Calculated and measured vertical settlement for inclinometers INB1 and INB5 after construction for stages [E] to [G]: base case. Elevation 260 corresponds to bottom of the rockfill shell. 85
Figure 5.13 Vertical displacements for points B0-28, B0-9 and B0-5 along the dam crest: comparison of measured and calculated values for base case. 86
Figure 5.14 Contour plots for horizontal displacements in metres at (a) end of time [A] (b) end of time [C] (c) end of time [E] (d) end of time [F]. 87
Figure 5.15 Horizontal displacements for points B0-28, B0-9 and B0-5 along the dam crest: comparison of measured and calculated values for base case. 88

Figure 6.1 Calculated and measured vertical displacements for INB1 and INB5 at Time [B] for four differen values for λ_0^d. 92
Figure 6.2 Calculated and measured vertical displacements for INB1 and INB5 at Time [C] for four differen values for λ_0^d. 93
Figure 6.3 Calculated and measured vertical displacements for INB1 and INB5 at Time [E] for four differen values for λ_0^d. 93
Figure 6.4 Calculated and measured vertical displacements for INB1 and INB5 at Time [F] for four differen values for λ_0^d. 94
Figure 6.5 Variation of compressibility parameter λ^d for different α_{scaling} values. 95
Figure 6.6 (a) Compressibility for samples with different maximum particle size at two different void ratios (b) Corrected compressibility of limestone material to account for scale effect. Modified from Oldecop and Alonso (2013*a*). 96
Figure 6.7 Variability of parameter α_{scaling} based on void ratio for laboratory data. Data from Oldecop and Alonso (2013*a*) and simulation results of Denis-Perron and Beliche Dam. 97
Figure 6.8 (a) Construction sequence (b) Water pressure for upstream points (c) Water pressure for downstream points. 99
Figure 6.9 Vertical displacements for markers B0-28, B0-9 and B0-5 for the Base case, Low Permeability and High permeability cases. 100

Figure 6.10 Horizontal displacements for markers B0-28, B0-9 and B0-5 for the Base case, Low Permeability and High permeability cases. 101

Figure A.1 (a) Simulation layers and (b) Mesh from (Alonso et al., 2005) 109
Figure A.2 (a) Simulation layers and (b) Mesh from validation problem 109
Figure A.3 Vertical displacements at position for extensometers (a) I1, (b) I3 and (c) I6 for construction stages [A] to [E]. Validation simulation results and computed results from Alonso et al. (2005) 112
Figure A.4 Validation simulation and Alonso et al. (2005) simulation of vertical stresses for stages [A], [B] and [E] on a horizontal plane at elevation 13 m above boundary of clay core. 113

Figure B.1 (a) Particles of an unsaturated low-plasticity soil, adopted from Oldecop and Alonso (2004) (b) Rockfill particle with a crack (pore), modified from Oldecop and Alonso (2001). 116
Figure B.2 Sketch of a simplified volume of rockfill and a rockfill particle containing a crack that eventually propagates and causes particle breakage. Modified from Oldecop and Alonso (2013*a*). 117
Figure B.3 Typical stress intensity curve. Modified from Oldecop and Alonso (2007). . . . 118
Figure B.4 (a) Water vapour entering an idealised crack, modified from Oldecop and Alonso (2013*b*) (b) Reaction between a water molecule and a strained silicium dioxide molecule. Modified from Michalske and Freiman (1982). 119
Figure B.5 Rockfill particle with contact crushing zone and a single fracture surface, Alonso et al. (2013). 120
Figure B.6 Rockfill particle with contact crushing zone and a single fracture surface, Alonso et al. (2013). 121
Figure B.7 Variation of breakage index with change of the coefficient of uniformity, adapted from Cristian (2011). 122
Figure B.8 (a) Time-dependent compressibility index against applied stress for different constant suction values (b) Correlation between time-dependent compressibility index and compressibility index for tested rockfill. Adopted from Oldecop and Alonso (2007). 124
Figure B.9 Relative humidity (RH) controlled oedometer test and water transport scheme circulation inside rockfill particle, adopted from Oldecop and Alonso (2004). . 126

Acknowledgements

I offer my sincerest gratitude to my supervisor, Professor Mahdi Taiebat, who has supported me with his guidance throughout my research. His encouragement and high level of competence inspired me to explore the subject. I am truly indebted and thankful to him for the time he devoted to discussions on the subject matter and for his moral support. His comments helped me to become a better researcher. My sincere thanks are extended to Dr. Arcesio Lizcano and Professor Ali Pak for providing technical support during various stages of this research project, giving me the momentum to keep going, and providing feedback on the final manuscript. I would also like to thank Dr. Nuria Pinyol for assisting with the use of the finite element software, and Dr. Ruth Derksen for patiently helping me improve my technical writing skills, and Annick Bigras, Éric Péloquin, and Daniel Verret of Hydro-Québec for providing technical insight to the instrumentation data.

I would like to thank my girlfriend Cecillya Sumono for always being patient, supportive and loving. Her positivity and love helped me go through the tough times and gave me strength and energy to persevere. Thanks will not be enough for my parents, Violeta and Nikolay Kolevi, without whose support none of my accomplishments would be possible. Even with a long distance between us, their support remains as strong as ever.

Financial support for the project was provided in part by the Natural Sciences & Engineering Research Council of Canada (NSERC).

Chapter 1

Introduction

1.1 Motivation

Rockfill has gradually become a significant part of the construction industry since the beginning of the nineteenth century. Some of the first larger construction projects were mining dams in California (Oldecop and Alonso, 2001). An understanding of rockfill behaviour has been a challenge due to difficulties of constructing large scale testing devices. Another source of information for rockfill, is records of already existing structures as presented on Figure 1.1. The long term deformations of the structures can be seen on Figure 1.1, where the crest settlement of a number of dams is presented over the span of five to thirty years.

The purpose of the design of earth and rockfill structures is to ensure the stability and operational requirements of the structure throughout its entire life-span. In the case of dams, the upstream and downstream slopes must be stable during construction and impoundment as well as in the long term operation of the dam (Cardoso and Alonso, 2010). Another consideration is reduction of settlement or creating compatible compressibility between the shells and core in order to avoid cracking of the core (Parkin, 1977). A key factor for concrete-faced compacted rockfill dams is the determination of deformations induced during construction and impoundment (Saboya Jr. and Byrne, 1993). Some other rockfill structures that support railways need detailed prediction of long term settlements due to an operation criterion of the facilities (Oldecop and Alonso, 2001).

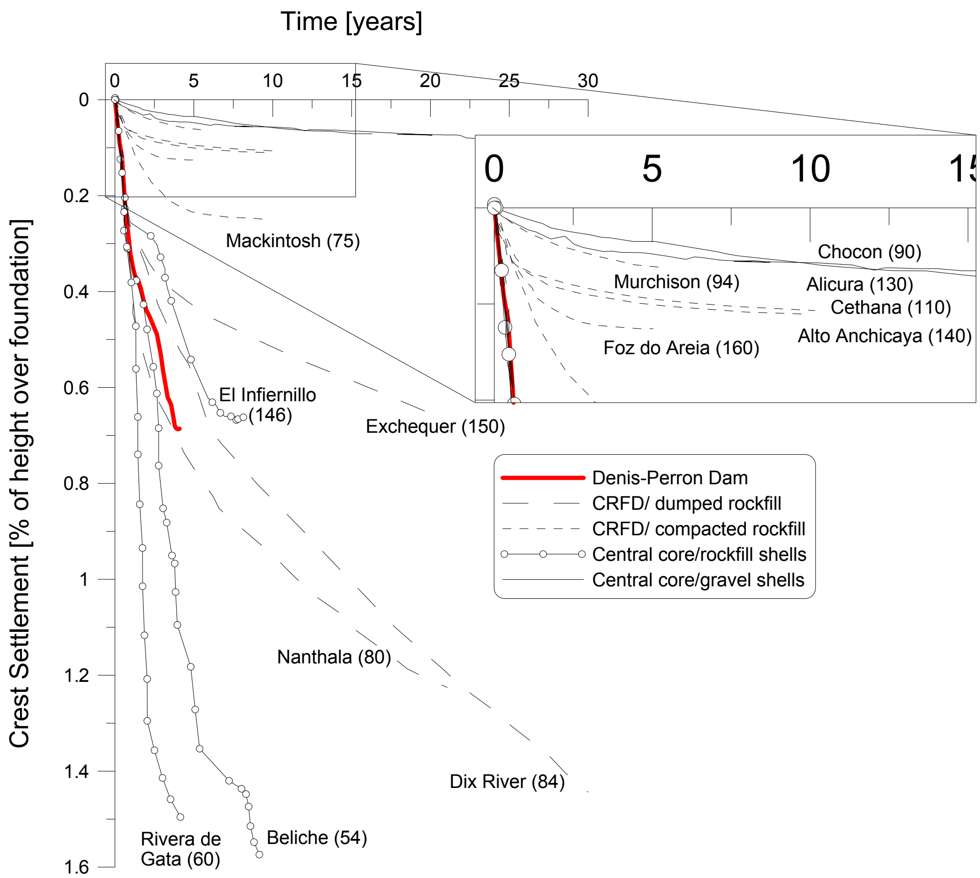

Figure 1.1: Deformations durign operation of multiple rockfill dams. The numbers in brackets represent the height of the respective dam. Data obtained from Oldecop and Alonso (2013*a*).

Oldecop and Alonso (2001) have tackled the complex behavioural patterns of rockfill response in the framework of continuum mechanics by introducing an elasto-plastic constitutive model using the concept of “compressibility despite the fact that rockfills usually consist of very large discrete particles. Obtaining the model parameters presents a challenge due to having particles in the field with sizes as large as 2 m, whereas laboratory tests are limited to samples with much smaller size of up to 0.2 m (Saboya Jr. and Byrne, 1993). Another way of exploring the behaviour of rockfill is by observation of already existing structures and analysing field measurements, such as the analysis of Beliche dam described in the work of Alonso et al. (2005).

1.2 Goals

Although a lot of studies have been conducted in the area of rockfill mechanics, no comprehensive guide and methodology for modelling of rockfill structures has been provided. Therefore, one of the major goals of the current thesis is to address this deficit and create a framework for the analysis of rockfill dams. A numerical study on the well instrumented Denis-Perron dam is conducted using the constitutive model developed by Oldecop and Alonso (2001). The dam consists of rockfill shoulders and a central clay core, and has experienced settlement due to impoundment and rainfall as seen on Figure 1.1. The instrumentation data provide an excellent opportunity to examine the state-of-the-art modelling techniques for settlement response of rockfill dams. The simulation of the stage construction and impoundment phase is conducted using the above model in Code_Bright (2015), which is a fully coupled three-phase finite element program for unsaturated porous media.

The second goal is to explore the theory of rockfill behaviour and test it against a comprehensive set of field measurements like settlements, displacements, water pressures and stresses via a numerical simulation. Environmental effects like rainfall are explored as well as some microscopic ones like particle size and "creep" effects. An interesting outcome of the work is to quantify the particle size effect based on the available field measurement. Such quantification via a large scale numerical simulation potentially opens doors for researchers to explore other existing dams in the same way and further investigate this effect.

1.3 Thesis structure

This thesis is separated in multiple different Chapters. Chapter 2 describes the Denis-Perron dam in detail. It includes the background of the project, available field instrumentation data and laboratory tests carried out on the different materials.

Chapter 3 explores the different constitutive models used to capture the behaviour of the dam materials. Higher attention is placed on the constitutive model for the rockfill in particular.

Chapter 4 describes the process of creating the Finite Element model. This includes a detailed description of calibration of the material parameters for each zone of the dam. Initial and boundary conditions are also explored. Finally, information regarding the finite element mesh is included.

Following the numerical model description, Chapter 5 explores the outcomes of the simulation from Chapter 4. This is considered the "base case" and is later used for sensitivity analysis purposes. Simulation results of the base case are compared with available field measurements such as vertical and horizontal displacements, total stresses and water pressures.

Chapter 6 builds on top of the base case by exploring different aspects of the rockfill behaviour.

The first half of the chapter aims to quantify the effect of particle size on rockfill compressibility. The second half explores the effect of rockfill permeability on the response.

The thesis leads to a summary and conclusions of the findings and recommendations for future research.

Appendix A summarizes a validation stage conducted prior to the analysis of the Denis-Perron Dam. It has been completed through reproducing the results of Alonso et al. (2005). Exploration of the key factors influencing the rockfill behaviour are presented in Appendix B.

Chapter 2

Denis-Perron Dam – case description

2.1 Project background

The Denis-Perron Dam is a rockfill embankment dam spanning the Sainte-Marguerite River, part of the lower Saint Lawrence River, in eastern Québec, Canada. The geographical location of the dam can be seen on Figure 2.1 and the cross section on Figure 2.2. The dam is the second highest in Québec and the hydraulic head of its power plant is also the largest in the province.

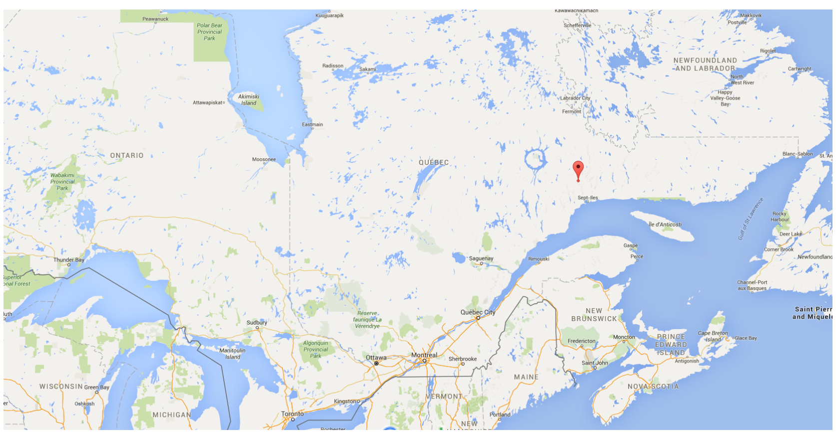

Figure 2.1: Location of Denis-Perron

Construction on the dam began in 1994. Prior to dam construction, a 19 m high co er-dam was built to direct the river through a tunnel west of the site according to Hydro-Québec (1999). The dam began to impound water in 1998 and finally reached full capacity in 2001. The dam

Figure 2.2: Aerial view of Denis-Perron Dam (Péloquin, 2015)

and reservoir lies in a very remote region, and a 86 km long access road was built to facilitate transportation to the construction site (Péloquin, 2015).

Project completion occurred in 2002 and the cost is estimated to be around CA$2.4 billion. This makes the dam one of the most significant 21st century hydroelectric developments in North America. As of 2003, the dam was projected to generate about 2.73 TWh of electricity per year, or an average output of just over 310 megawatts (MW) (Hydro-Québec, 1999).

The dam impounds a 140 km long, 253 km^2 reservoir with a capacity of about 12.5 km^3. Excess water is released through a set of outlets at the base of the dam, with a capacity of 1,440 m^3/s, and an emergency spillway about 1 km north-west of the dam. Standing 171 meters (561 ft) high and 378 meters (1,240 ft) long, the dam is the primary component of Hydro-Québec's Sainte-Marguerite 3 hydroelectric project (Péloquin, 2015). The dam has a central till core, filters and transitions that rest on concrete. The rockfill shoulders of the river portion are built on alluvial deposit. On the abutments, the entire dam section rests on bedrock. The crest level is at 410 m and its width is 10 m. Downstream slope of the dam is approximately 1.65H : 1V and the upstream slope is 1.75H : 1V (Bigras and Tournier, 2000). The dam is analysed in 2D and the chosen section

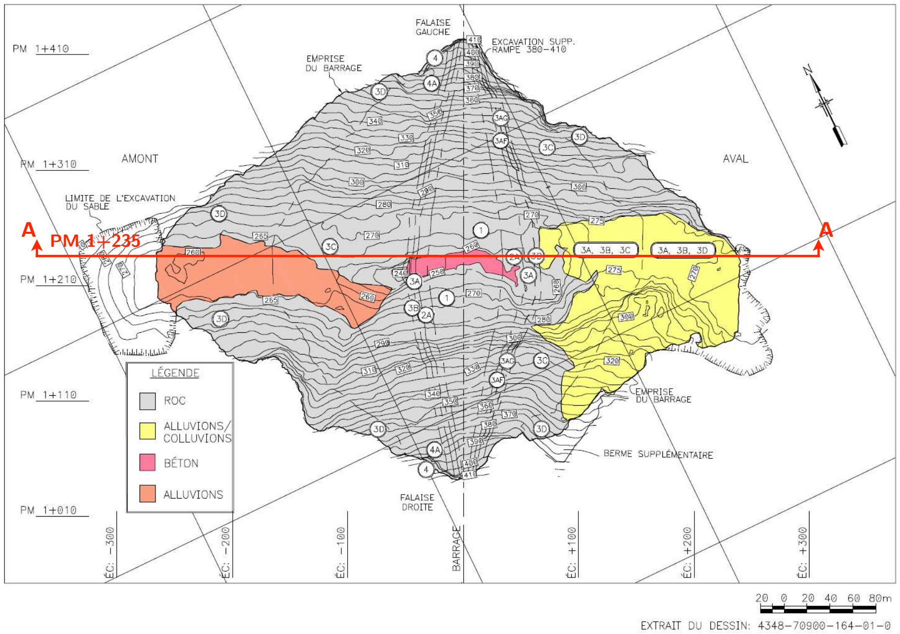

Figure 2.3: Analyzed cross section A-A of Denis-Perron dam (Péloquin, 2015).

for the analysis is shown in Figure 2.3 annotated with *PM 1+235*.

The simplified geometry in 2D is shown on Figure 2.4 and the dam materials are marked appropriately.

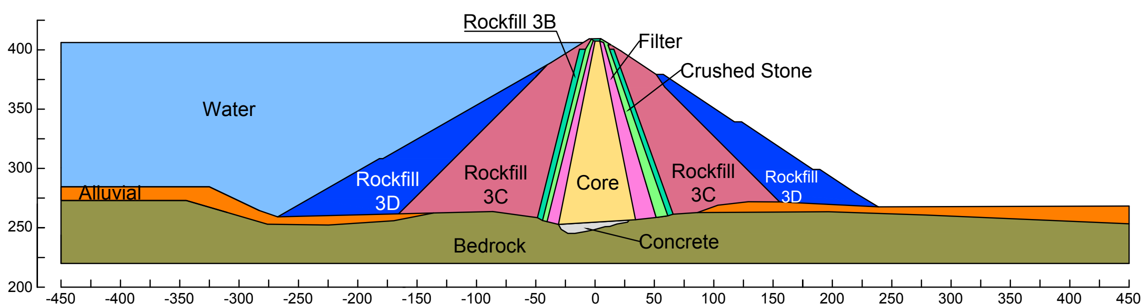

Figure 2.4: Analyzed cross section A-A visualized in 2D.

2.2 Field instruments

The Denis-Perron Dam has several types of auscultation devices to monitor its behaviour. The instruments mainly aim to measure pore pressures, infiltration rates and deformation. A total of 238 instruments were installed to monitor the dam. For the analysis of the dam, only instruments with proximity to the analysed cross section and instruments that were not reported to be defected are used. All of the instruments available and the ones chosen for the analysis are summarized in Table 2.1. More details about each instrument are presented in the next sub-sections of this chapter.

Table 2.1: Available instruments along the whole body of the dam(Hammamjil, 2003).

Type of instruments	Number of instruments		Instruments used in analysis
	Total	Defect	
Electrical piezometers	56	5	—
Open tube piezometers	3	2	—
Pneumatic piezometers	23	1	PPB272; PPB302; PPB342; PPB381;
Total pressure cells	4	—	CPB251; CPB255;
Relative settlement gauges	13	13	—
Total settlement gauges	3	3	—
Inclined inclinometers	6	1	INB1
Vertical inclinometers	3	1	INB5
Horizontal inclinometers	2	1	—
Individual thermometers	27	8	—
Chain thermometers	40	10	—
Observation terminals	33	—	BO-28; BO-9; BO-5
Settlement marks uphill	17	17	—
Weirs	6	—	—
Accelerometers	2	—	—

Some of the instrumentation data is presented in terms of a simulation time interval, correlating simulation time with real time. The time intervals are presented bellow.

A Construction to elevation 320 m
$t = 0 - 400$ days
B Construction to elevation 360 m; Impounding of the reservoir to elevation 292 m
$t = 400 - 610$ days
C Completion of construction to elevation 410 m; Impounding of the reservoir to elevation 343 m
$t = 610 - 760$ days
D Impounding of the reservoir to elevation 350 m
$t = 760 - 980$ days
E Impounding of the reservoir to elevation 382 m
$t = 980 - 1500$ days
F Completion of reservoir impoundment to elevation 405 m
$t = 1500 - 2320$ days

2.2.1 Inclinometers

Dam deformations are measured by vertical, inclined and horizontal inclinometers and by surveys of observation terminals. A cut in the centre of the river is instrumented by a few inclinometers: two vertical inclinometers, located in upstream recharge areas; an inclined inclinometer in the downstream filter and a horizontal inclinometer in the downstream shell. The inclinometer installed in the upstream shell aims to detect of rockfill subsidence when impoundment occurs. Two more cuts are equipped with inclinometers inclined in the downstream filter only. The vertical and inclined inclinometers are anchored in the rock end to create a reference point. Terminals are the standard type used by Hydro-Québec. The movements of these benchmarks are measured two to four times per year from the reference points in the riverbanks.

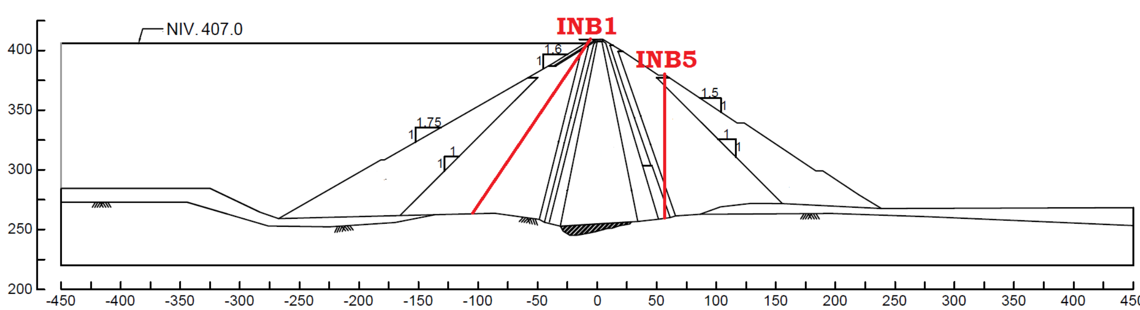

Figure 2.5: Locations of upstream and downstream inclinometers INB1 and INB5, respectively.

The inclinometers used in this study are INB1 and INB5, shown on Figure 2.5. INB1 is located in the upstream side of the dam, where the rockfill gets gradually impounded. This inclinometer aims to capture the effect of the impoundment and provide valuable information about the occurring settlements. INB5 is located downstream, where the rockfill does not get flooded due to the core action. This inclinometer helps to capture the "dry" behaviour of rockfill and allows for re-calibration of the material parameters. Both INB1 and INB5 measurements used are relevant to the end of the construction phase. Figure 2.6 shows the field measurements of both inclinometers for three different points in time during construction. For INB1, the black line represents construction up to elevation 325m with no impoundment; the green line represents construction up to 360m and partial impoundment to elevation 293m (blue line shows reservoir level); and the orange line shows the end of construction with partial impoundment to elevation 334m (blue line shows reservoir level). For INB5, the dates of measurement are chosen to be as close as possible to the ones of INB1 for consistency purposes.

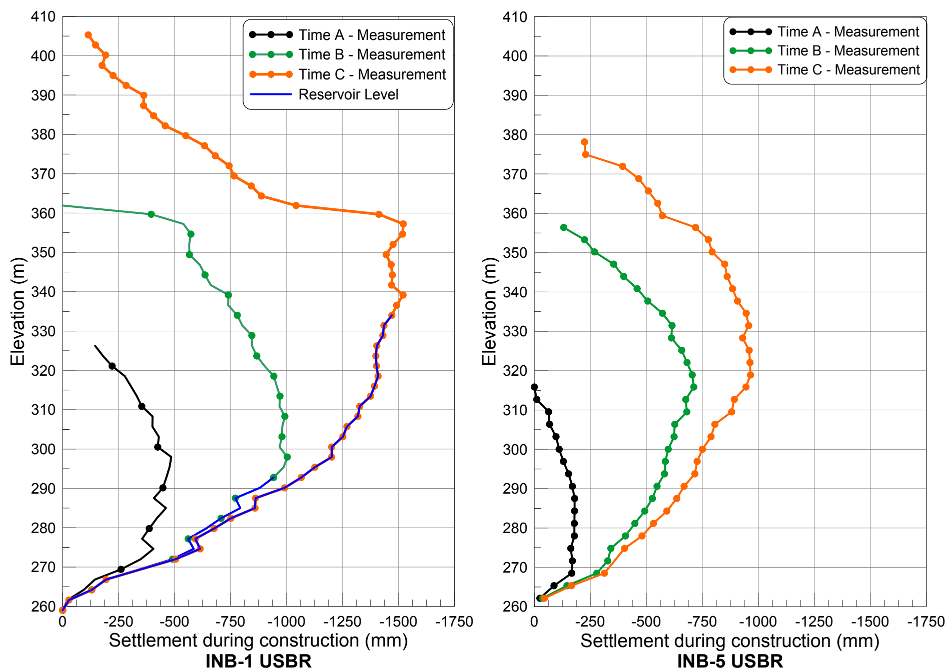

Figure 2.6: Vertical settlement measurement for INB1 and INB5 during construction for end of time intervals [A] to [C].

Data for settlements of INB1 and INB5 after construction is provided as well. Initial data show large settlements of both inclinometers at elevation 260 m, where they attach to the bedrock. The reason for such settlements are unclear. The data has been processed by subtracting the settlements of elevation 260 m to every data point, making elevation 260 m as the reference point. This approach could yield the data unusable due to the unclear circumstances which lead to high settlements (in the range of 0.5 m) close to the bedrock. The processed data is shown on Figure 2.7. From the plot of INB1, it can be seen that at the already impounded area, little settlements occur as expected. From the plot of INB5, settlements occur at all elevations due to creep effects and rainfall.

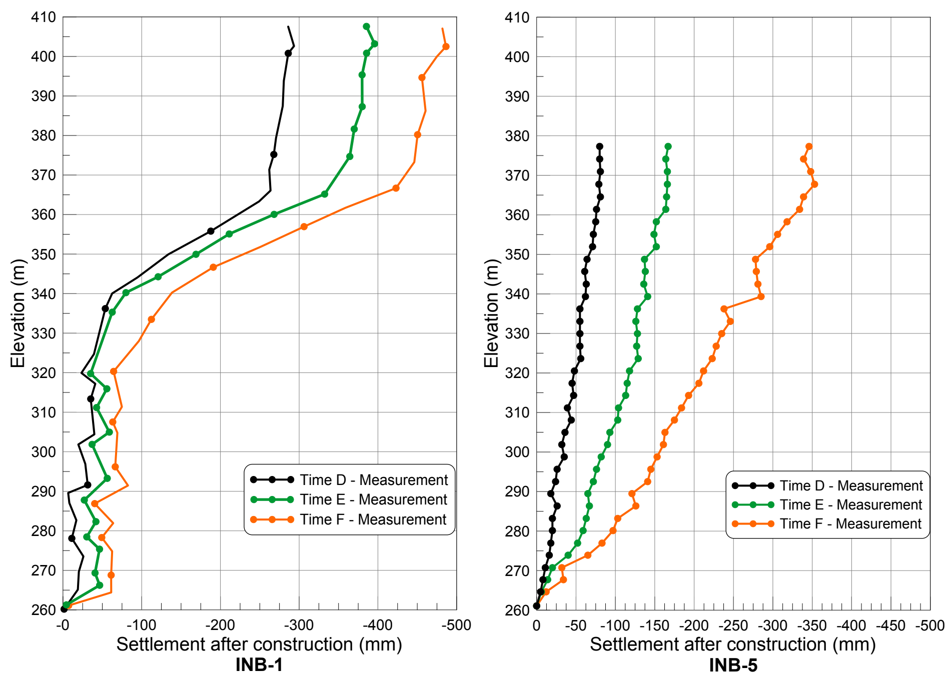

Figure 2.7: Vertical settlement measurement for INB1 and INB5 after construction for end of time intervals [D] to [F].

2.2.2 Pressure cells

Four pressure cells have been placed on the concrete surface at the bottom of the till core to monitor the development of vertical stresses and detect the magnitude of the arching effect. These instruments are very sensitive to variations in compressibility of the backfill around them. They are located near the piezometers in order to calculate effective stresses. Only two pressure cells are used for the analysis: one in both ends of the core as seen on Figure 2.8.

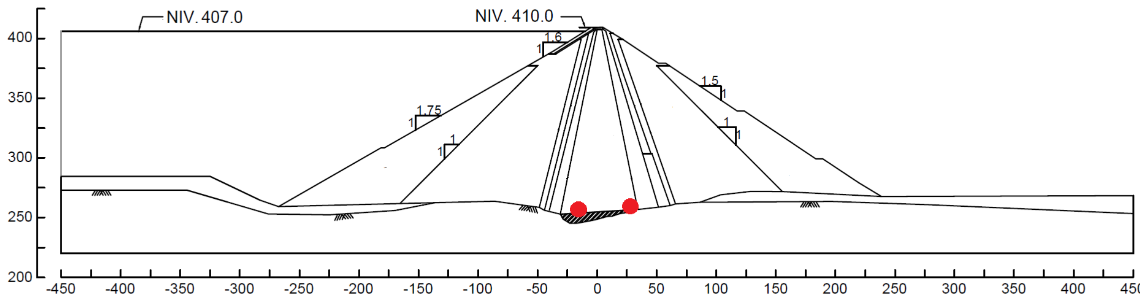

Figure 2.8: Location of total pressure cells CPB 251 and CPB 255.

The plotted pressure readings can be seen on Figure 2.9. The top X axis shows the measurement dates. The bottom X axis shows the corresponding time in days, where time "0 days" represents 8/27/1996. The reason for showing this axis is to relate the numerical simulation time to real life time. Those X axes are used in the plots of observation terminals and piezometers data as well

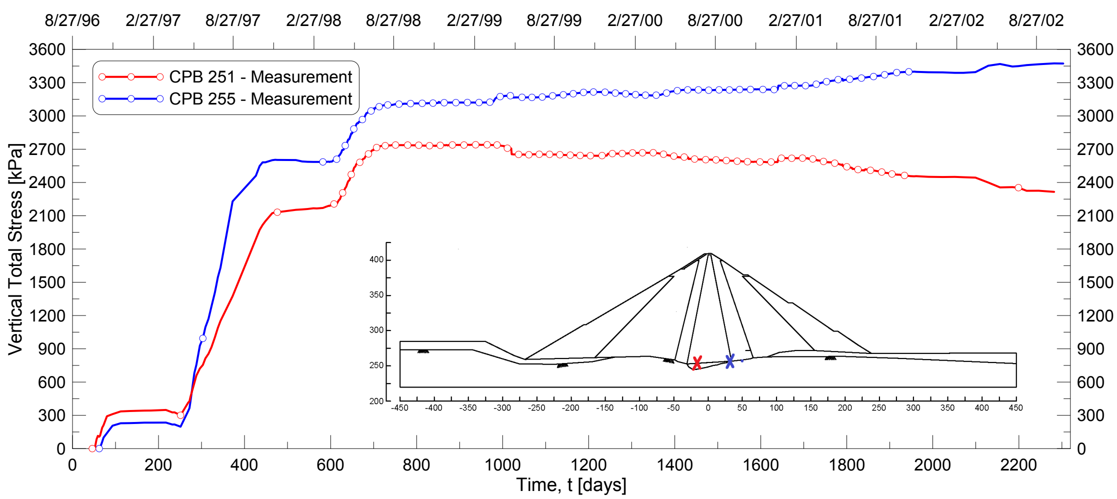

Figure 2.9: Total pressure cell measurements of CPB 251 and CPB 255,

2.2.3 Observation terminals

The observation terminals are concrete buildings with a total length of 2 m, partially inserted in the embankment. The survey has a total of 33 observation terminals in the whole dam (BO-1 to BO-33) which periodically measure cumulative horizontal and vertical displacements. Three stations are selected that are in proximity to the cross section *PM 1+235* and are labelled BO-28, BO-9 and BO-5.

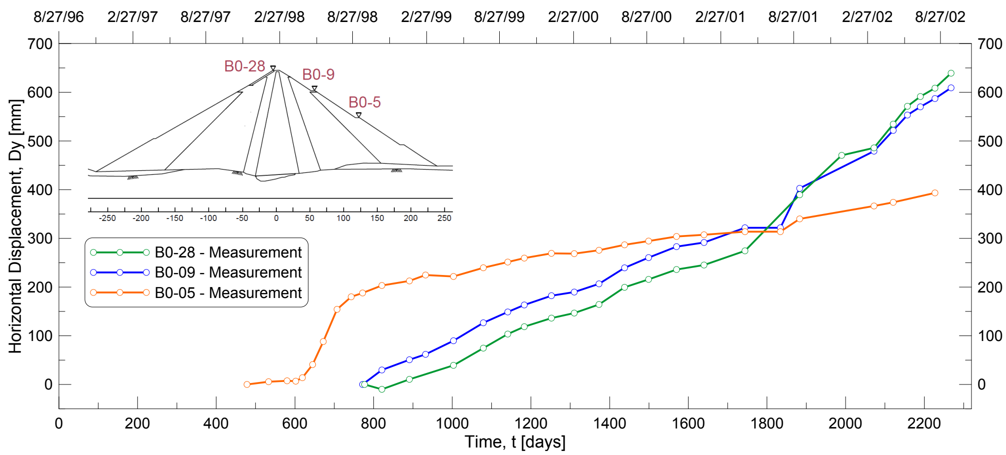

Figure 2.10: Downstream horitonztal displacement gauges measurements of B0-28, B0-9 and B0-5.

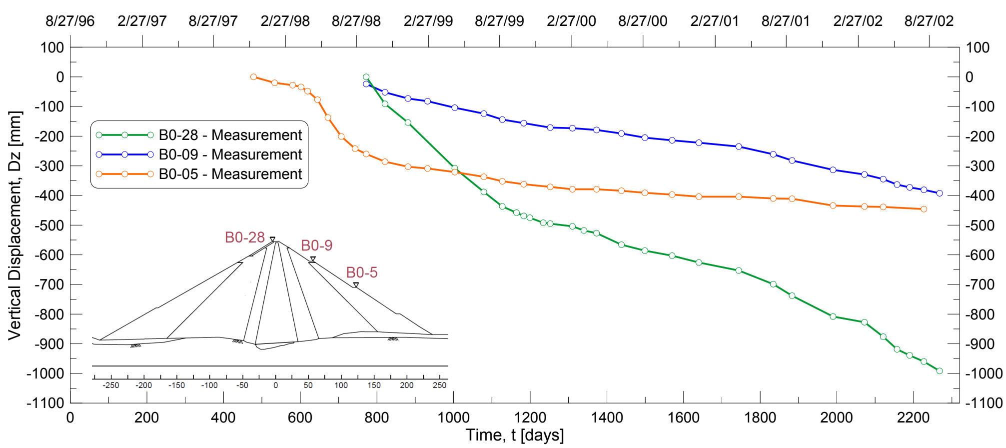

Figure 2.11: Downstream vertical displacement gauges measurements of B0-28, B0-9 and B0-5.

The cumulative horizontal displacements are plotted on Figure 2.10 and show the development of horizontal movement with time. Similarly, cumulative vertical displacements are presented on Figure 2.11.

It has to be noted the top of inclinometer INB1 matches the location of that observation terminal B0-28. The measurement for INB1 at end of construction and impoundment is around 500 mm and the measurement for B0-28 for the same date is 1000 mm, which introduces a big discrepancy in the results. It was discussed that INB1 had some unknown issues regarding its post-construction measurements (stages [D] to [F]), therefore its results could be considered unreliable. Results are compared to the post-construction measurements of INB1 for consistency purposes.

2.2.4 Piezometers

Five pneumatic piezometers have been installed in the till core, the locations of which are shown in Figure 2.12. The apparatus consists of a metallic body housing a porous ceramic filter, a cell filled with distilled water and a diaphragm. A rate of gas (nitrogen) under pressure is supplied to the diaphragm via tubing input. The gas pressure is applied gradually to avoid sudden detachment of the diaphragm. The pressure causes separation and is equivalent to the piezometric pressure exerted on the diaphragm.

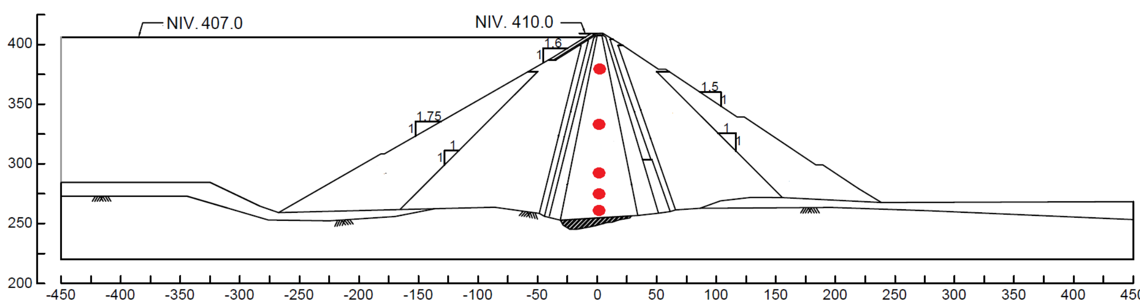

Figure 2.12: Location of piezometer cells PPB 272, 302, 342 and 381.

Frequently observed variations in readings are often explained by the sensitivity of the diaphragm and the difficulty to control the gas pressure applied on the diaphragm. An effective use of the device involves a prolonged and sufficient reading time in order to allow the diaphragm to return to its initial position. An insufficient length of reading stabilization could cause erroneous readings. Excessive length of the inlet pipe also causes loss of pressure applied to the end of the tubing in contact with the diaphragm. That said, the pneumatic piezometers are considered less accurate than electric piezometers. However, they are simple to build, reliable and not prone to electrical disturbances. Readings of pressures were performed using PR-20 indicator. The position allows rapid filling of tubes and direct reading of the pressure measured by the sensor according to Hammamjil (2003).

Data was provided in the form of piezometer levels and was transformed into readings of pore pressures using

$$\text{NP} = \text{Cote} + 0.10197 \times \text{Reading} \tag{2.1}$$

where "NP" is the piezometric level (m), "Cote" is the installation level of the piezometer (m), the factor "0.10197" is a conversion factor for the specific device, transforming from kPa to meters (m/kPa), and the "Reading" is the field measurement of pore pressures (kPa). The measurements are plotted on Figure 2.13 and are later used to compare simulation pore pressures. The measurement at point PPB 251 has strange variations and is reported to be broken. Instruments PPB 272, 302, 342 and 381 are sufficient for comparison purposes.

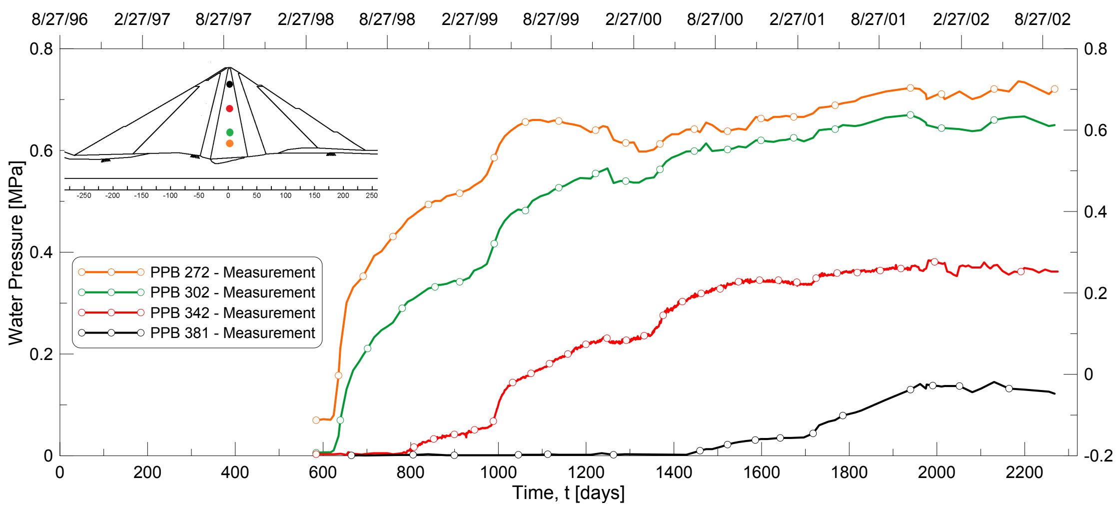

Figure 2.13: Piezometer cells measurements for PPB 272, 302, 342 and 381.

2.3 Laboratory data

2.3.1 Central till core

A major component of the dam that needs appropriate attention during analysis is the core. Laboratory tests have been performed to determine key characteristics of the behaviour of the glacial till core. The angle of internal friction is reported to vary between 38° and 40°. Triaxial-permeability tests have been performed on the core to establish the major hydraulic properties. Based on the triaxial test results the hydraulic conductivity is reported to vary between 1×10^{-5} and 1×10^{-8} cm/s (Péloquin, 2015). Grain size distribution and dry density measurements are available as well. The grain size distribution of the till material can be seen on Figure 2.14. The red line represents the grain size distribution of a similar sample from Northern Québec. The sample has very similar characteristics as the one used for the till core of Denis-Perron and has undergone more testing, which will aid the calibration of the mechanical parameters in the analysis.

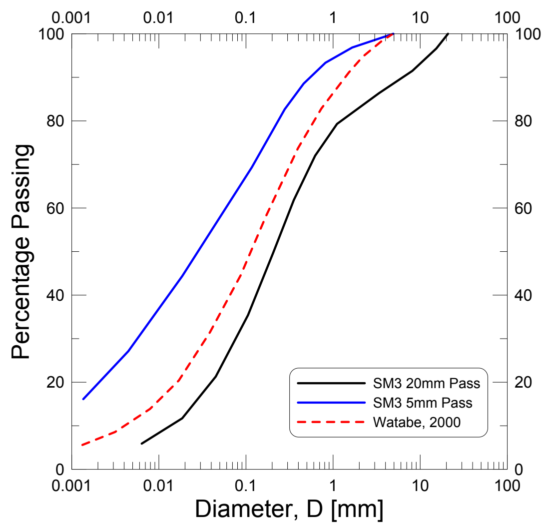

Figure 2.14: Grain size distribtuion of the Denis-Perron till core material (Hammamjil (2003)) and the grain size distribution of a till sample from Northern Québec (dashed red line) (Watabe et al., 2000).

Table 2.2 shows all the Dry density measurements of the till core material using Standard proctor or Nuclear device.

Table 2.3 shows the characteristics of three samples from the core 2660-D, 2741-O and 3708-O. Triaxial tests have been performed and a coefficient of permeability has been determined for each of the samples. Unknown properties of the material, due to limited laboratory data is taken from literature. Laboratory tests on a similar material from Northern Québec are available in Watabe et al. (2000), but this is discussed in detail in Chapter 4.

Table 2.2: Till core dry density measurements (Péloquin, 2015).

	In place Dry Density (nuclear device)	Maximum Dry Density (Standard Proctor)
Number of Tests	256	250
Average	2113 kg/m^3	2137 kg/m^3
Standard Deviation	53 kg/m^3	53 kg/m^3
Minimum	1960 kg/m^3	2002 kg/m^3
Maximum	2232 kg/m^3	2284 kg/m^3

Table 2.3: Results of triaxial permeability tests (Lafleur, 1998).

Preconsolidation Pressure σ'_3	Compaction				Final water content $w_f[\%]$	Hydraulic conductivity k [cm/s]
	Water content $w_0[\%]$	Void ratio e_0	Dry density ρ_{dry}	Saturation S_r		
Sample 2660-D						
500	7.9	0.29	2130	75	9.8	9.8E-6
1000	7.8	0.30	2116	72	10	1.3E-5
1500	7.7	0.32	2099	66	10	1.2E-5
Sample 2741-O						
500	8.8	0.24	2215	99	7.3	1.1E-8
1000	8.6	0.25	2193	93	7.0	8.3E-9
1500	9.0	0.24	2209	99	6.7	1.1E-8
Sample 3708-O						
500	8.0	0.31	2100	71	9.7	4.4E-5
1000	8.0	0.3	2111	73	10.1	4.0E-5
1500	7.9	0.29	2132	75	9.7	2.0E-5

2.3.2 Rockfill shells

Oedometer tests have been performed on dry and saturated material with a reported scaled grain size distribution, where the coefficient of uniformity, C_u, of the oedometer and the field material has been preserved. The results can be seen on Figure 2.15.

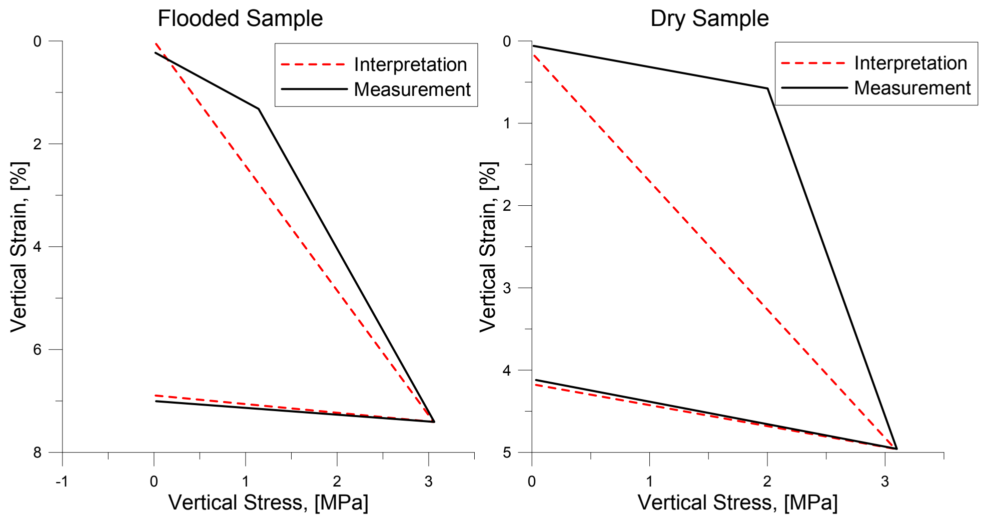

Figure 2.15: Oedometer rockfill data for dry and saturated samples (Errecalde, 2012).

The black line is the idealized measurement because the data is adopted from figures in Errecalde (2012). It is reported that at the beginning of the loading stage, the testing head got stuck. This resulted in measuring unrealistically low vertical strain. At higher stresses, the head got released and caused high collapse. Therefore, determining of the mechanical properties of the material is done in accordance with the dashed red line (Interpretation) according to Errecalde (2012).

The grain size distributions of inner and outer shells of the dam are shown on Figures 2.16(a) and 2.16(b) respectively. The particle size specification curves were provided from the design team of SM3. These plots are the only laboratory data available for the rockfill material.Therefore, missing parameters are obtained from literature and a sensitivity analysis on a few of them is described out in Chapter 6.

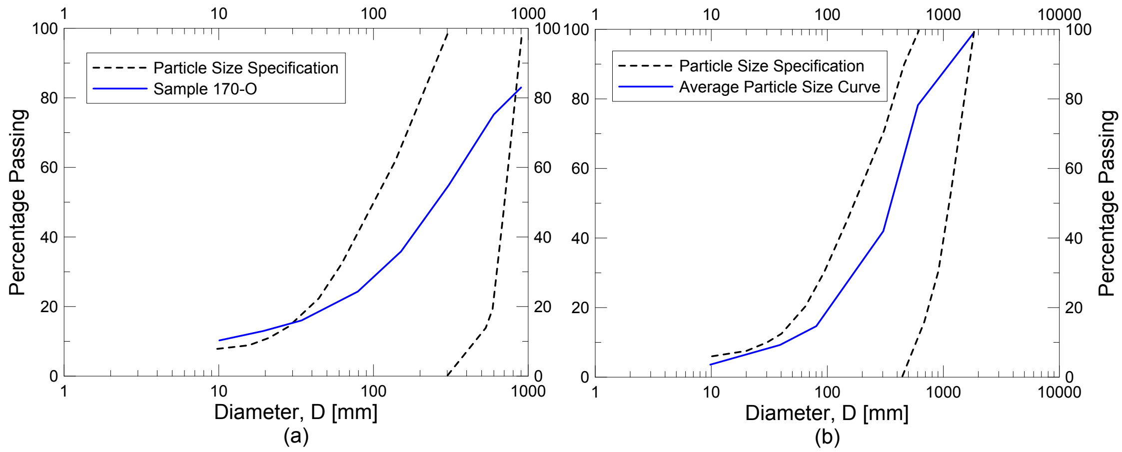

Figure 2.16: (a) Grain size distribution of inner shell (b) Grain size distribution of outer shell (Hammamjil, 2003).

2.4 Previous Denis-Perron dam analyses

Two analyses of Denis-Perron were previously performed. The first one was conducted in 1990 prior to construction of the dam. The purpose of this analysis was to aid the design and construction stages of the dam. The analysis used a hyperbolic model. The second analysis, was administered in 2012, at the Polytechnic University of Catalonia in Barcelona. The aim of this analysis was to capture the behaviour of rockfill based on current understanding of its unsaturated behaviour.

2.4.1 Pre-construction FE analysis using a hyperbolic model (1990)

Prior to construction of the Denis-Perron dam, a finite element analysis has been performed in order to determine the expected overall behaviour of the structure and guide the design. The information has been used to adjust the widths of different zones, geometry of the dam, specification controlling the establishment and compaction of the materials. The dam has been simulated only during construction. Impoundment has not been included, which is proven to cause the highest amount of settlement in rockfill. Therefore, the simulation results are expected to have more qualitative, rather than quantitative meaning. The figures and information are extracted from a technical report provided for Hydro Québec by Hydro-Québec (1990).

The dam is modelled in 2D at a cross section at the maximum height of the dam. The analysis has been performed in a finite element code called FEADAM Duncan et al. (1980), developed at the

University of California, Berkeley. FEADAM has an implemented hyperbolic model, developed by Duncan and Chang (1970). The model utilises 8 parameters that are used to establish the tangent modulus, unloading and re-loading modulus and the bulk modulus through equations 2.2, 2.3 and 2.4 respectively.

$$E_t = \left(\frac{R_f(1-\sin(\phi)(\sigma_1-\sigma_3)^2)}{2c\cos(\phi)+2\sigma_3\sin(\phi)} \right)^2 KP_a \left(\frac{\sigma_3}{P_a} \right)^n \tag{2.2}$$

$$E_{ur} = K_{ur}P_a(\sigma_3/P_a)^n \tag{2.3}$$

$$B = K_bP_a(\sigma_3/P_a)^m \tag{2.4}$$

Since no laboratory tests had been conducted at that point, the parameters for the materials of the foundation and embankment have been identified in literature for similar materials. Therefore, the parameters used for the simulation have been derived based on the LG4 dam (1979) Duncan et al. (1979). The parameters are summarized in Table 2.4 for one of the cases examined in the report.

Table 2.4: Hyperbolic model material parameters for all dam zones.

Material Description	γ (g/cm^3)	c (kPa)	ϕ (°)	K (kPa)	n	K_{ur} (kPa)	K_b (kPa)	m	R_f
Alluvion	1.88	0	34	1250	0.4	1500	600	0.2	0.7
Transition	2.2	0	38	600	0.4	800	240	0.2	0.7
Core	2.1	0	37	600	0.6	800	200	0.2	0.7
Filter	2	0	35	300	0.4	400	120	0.2	0.7
Rockfill	2.2	0	45	600	0.4	1000	240	0.2	0.7
Concrete	2.3	2000	5	60000	0.5	70000	3000	0.1	0.7

γ – density
c – cohesion
ϕ – angle of friction
K – compressibility modulus
n – exponent of the compressibility modulus
K_{ur} – unloading deformation modulus
K_b – volumetric deformation modulus
R_f – failure ratio

Six cases were used to examine different material properties. Table 2.4 shows the parameters for the first case. Contour plots are provided only for this case and are shown on Figure 2.17. Figures 2.17 (a) and (b) exhibit the vertical and horizontal deformations.

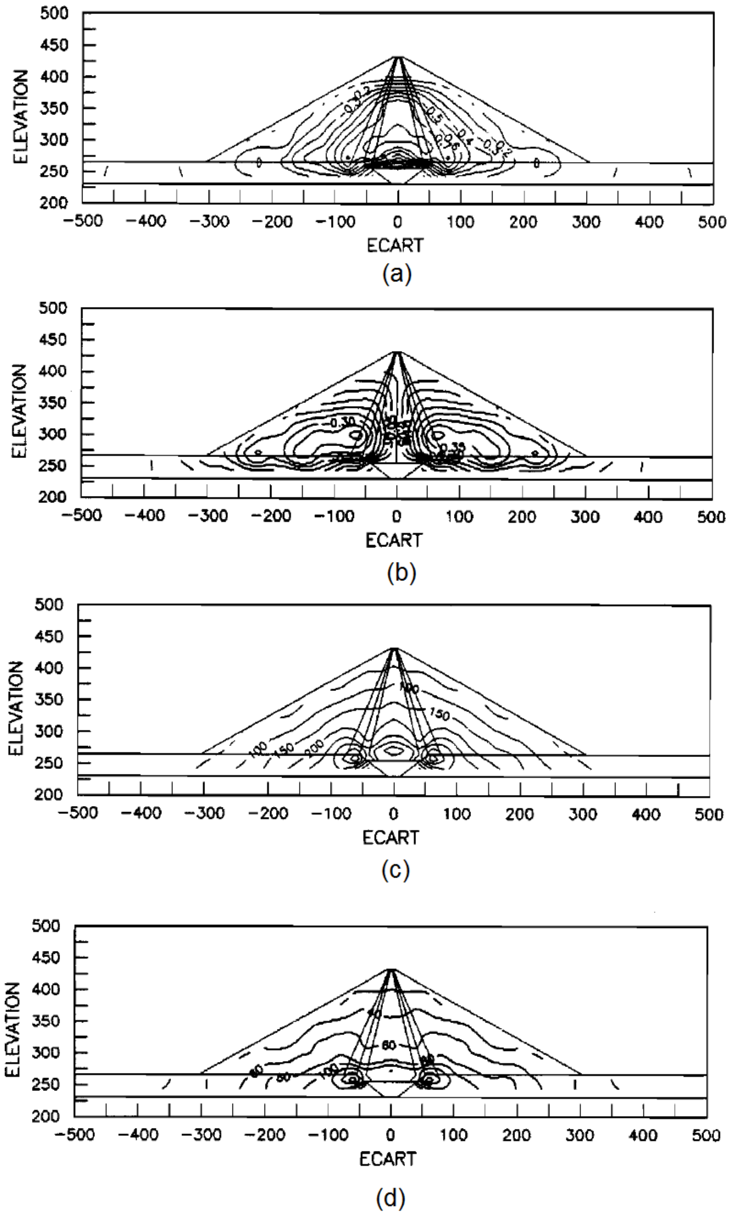

Figure 2.17: Contour plots of the simulation results for (a) Vertical displacements [m] (b) Horizontal displacements [m] (c) Vertical total stress [tonne/m^2] (d) Horizontal total stress [tonne/m^2].

Larger settlements are present in the rockfill and reach up to 0.8 m. Horizontal deformations are symmetrical. As mentioned in the previous chapter, more deformations are expected to occur during the reservoir impoundment. Figures 2.17 (c) and (d) convey the vertical and horizontal stresses in the dam. The expected stress transition between the rockfill, transitions and core are also observed.

2.4.2 FE analysis using the Rockfill Model (2012)

Errecalde (2012) conducted a more recent study on the Denis-Perron Dam with an attempt to capture the unsaturated behaviour of rockfill. The simulation has been completed using a 2D three phase finite element platform called Code_Bright, which has an implemented advanced constitutive model with the capability of capturing the rockfill behaviour. Current research uses a more recent version of the same software and the same constitutive models. Therefore, a detailed description of the constitutive models, modelling procedures and material parameters are provided in the next chapters of the thesis to avoid redundancy. For details, refer to Errecalde (2012)

Due to technical issues and non–convergence of the code, the simulation of Errecalde (2012) manages to successfully represent only construction of the dam up to the elevation of 360 m and partial reservoir impoundment. Comparison of the partial simulation results with field measurements of two inclinometers in the upstream (INB1) and downstream (INB5) are presented in Figure 2.18.

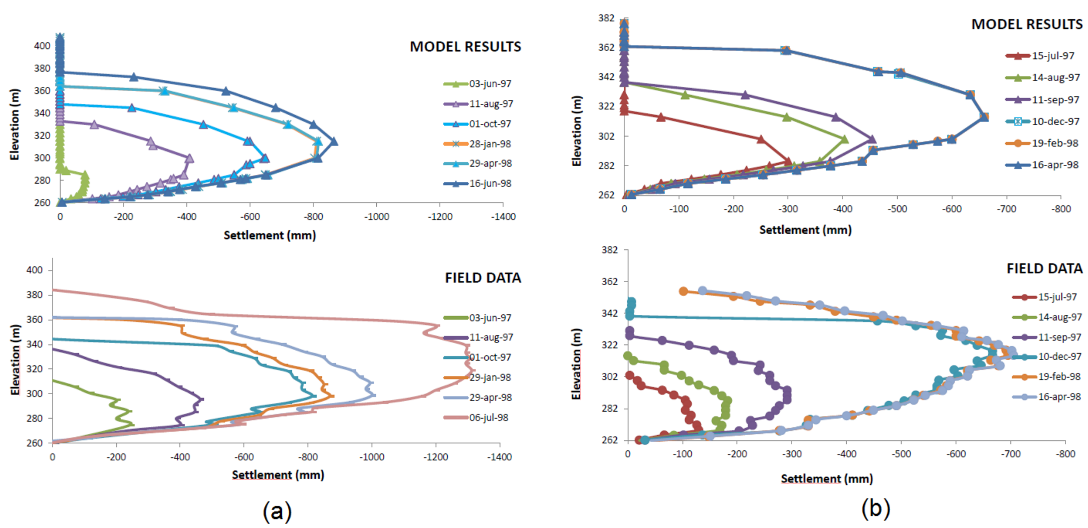

Figure 2.18: Vertical displacements at (a) Upstream inclinometer INB1 (b) Downstream inclinometer INB5 for different dates. Adapted from Errecalde (2012).

Chapter 3

Mechanical and hydraulic models used in the analysis of Denis-Perron

3.1 Introduction

This chapter introduces the advanced mechanical constitutive models and hydraulic models used to simulate the materials within the body of the dam. The linear elastic model used to simulate the rest of the materials, such as bedrock, is not presented due to its simplicity.

A constitutive model is a mathematical formulation of the stress and strain response of a material. Generally, constitutive models are a simplification of the real material behaviour, but can vary in the level to which they simplify the response. In order to accomplish an adequate simulation of a boundary value problem, it is important to have a necessary level of sophistication in the constitutive models.

In the recent decades, a number of models of different complexity have been developed. The hyperbolic model of Duncan and Chang (1970) was used to simulate Denis-Perron. The model requires two separate analysis for dry and saturated conditions, missing the transition of the partially saturated state of the dam. Another more recent elasto-plastic critical state model was used by Naylor et al. (1997) to back analyse Beliche Dam. This model requires two different set of parameters for dry and saturated conditions and it manages to capture the collapse mechanism of rockfill, but does not incorporate the important time dependent deformation of rockfill.

The first section in this chapter examines an advanced elasto-plastic three phase constitutive model used for modelling of unsaturated soils called the Barcelona Basic Model. The second section studies the mechanical behaviour of rockfill. Following is a description of the Rockfill Model (RM) constitutive model based on the principles of BBM and incorporating the observed mechanisms discussed prior to that. Finally, the last two sections discuss the hydraulic constitutive models used in the simulations.

3.2 Mechanical models

3.2.1 Barcelona basic model (BBM)

The Barcelona basic model has been developed at the Polytechnic University of Catalonia in Barcelona, Spain in the works of Alonso et al. (1990). BBM is intended for modelling of slightly to moderately expansive partially saturated soils such as silts, clayey sands, sandy clays and low plasticity clays.

The model is formulated in the framework of hardening plasticity and becomes a conventional critical state model (Modified Cam Clay) upon reaching full saturation. BBM is defined by two sets of stress variables. The first one is the mean net stress defined as $p = (\sigma_1 + 2\sigma_3)/3 - u_a$, where p is net mean stress, σ_1 is vertical total stress, σ_3 is horizontal total stress and u_a is air pressure. The second variable is the suction, defined as $s = u_a - u_w$, where s is suction and u_w is water pressure. The deviatoric stress is defined in a conventional way as $q = \sigma_1 - \sigma_3$.

The strains associated with the model are split into the conventional volumetric and deviatoric strains, notated with v and q as a subscript respectively. Each of them is obtained due to change of stress (loading/unloading) or change of suction, notated with with l and s as a superscript respectively. The strains induced based on changes of stress or suction are either elastic or plastic and are notated with e and p as a superscript respectively. A visual break down of the strains is presented in Figure 3.1. The changes of stress and suction form two yield surfaces in (p,q,s) space and are shown on Figure 3.2 in (p,q,s) space

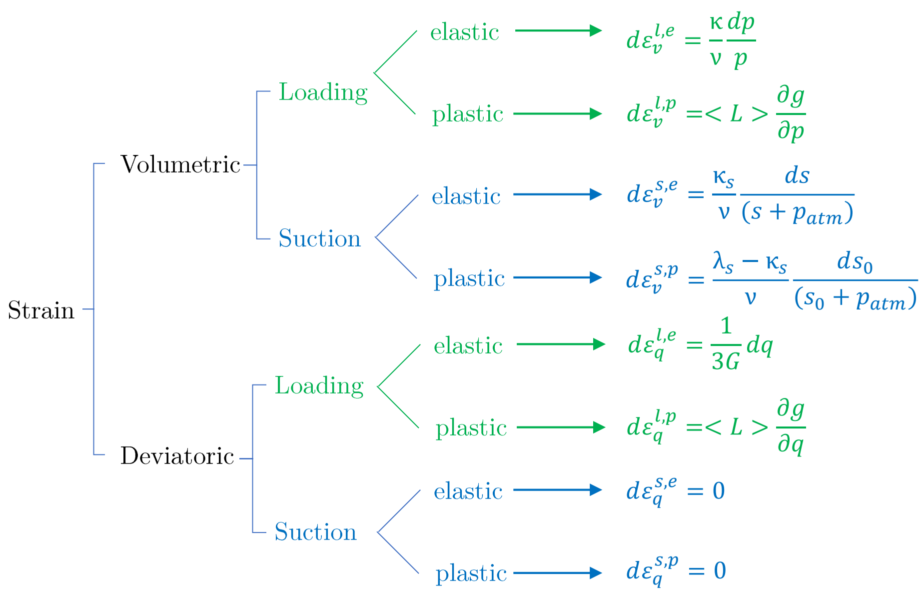

Figure 3.1: Strains assosiated with loading and suction changes in BBM.

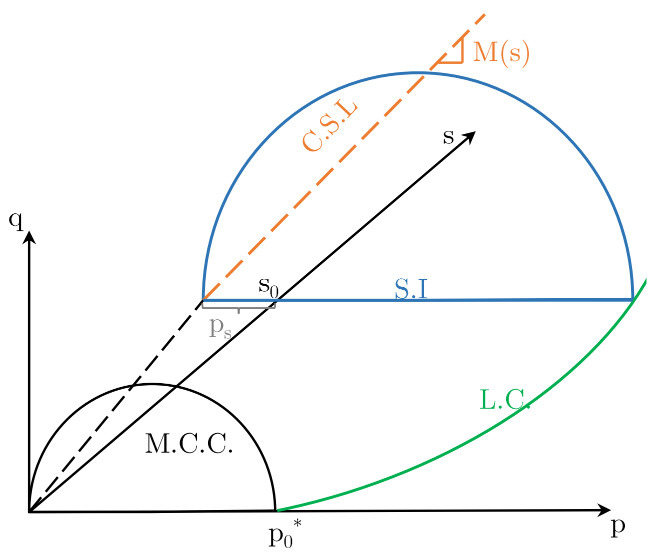

Figure 3.2: The dimensional view of the BBM yield surfaces in (p,q,s) space. Adapted from Alonso et al. (1990).

Yield surfaces

The first yield surface, f_1, is called the *L.C.* (loading-collapse) yield surface, which defines the increase in pre-consolidation pressure with increasing suction and also the collapse phenomena observed during wetting. At full saturation ($s = 0$), the yield surface is defined as the Modified Cam Clay (M.C.C). The surface in (p,q,s) space is defined as

$$f_1(p,q,s,p_0^*) = q^2 - M^2[p + p_s(s)]\,[p_0(s) - p] = 0 \tag{3.1}$$

where $p_s(s) = k_s s$ is a shear strength parameter, linearly increasing with suction and M is the critical state line slope defined in a conventional way as $M = 6\sin\phi/(3-\sin\phi)$. The loading-collapse curve (LC) defines the set of $p_0(s)$ values for each associate suction. It can be considered as a set of yield curves in (p,s) space. The LC curve is as follows:

$$p_0(s) = p^c \left(\frac{p_0^*}{p^c}\right)^{\dfrac{\lambda(0)-\kappa}{\lambda(s)-\kappa}} \tag{3.2}$$

where p_c is a reference stress, p_0^* is pre-consolidation stress for saturated conditions, $\lambda(0)$ is a compressibility parameter for saturated conditions, κ is an elastic stiffness parameter and $\lambda(s)$ is the change of the compressibility parameter with suction defined by

$$\lambda(s) = \lambda(0)\,[(1-r)\exp(-\beta s) + r] \tag{3.3}$$

where β controls the rate of increase of stiffness with suction and r is a parameter that defines the maximum soil stiffness.

The second yield surface, f_2, is associated with the suction increase locus (SI). The s_0 variable is the maximum past suction experienced. When suction is increased, s_0 bounds the transition from the elastic state to the virgin range. The yield surface is represented by Equation 3.4 and can be visualized on Figure 3.3 (a).

$$f_2(s,s_0) = s - s_0 = 0 \tag{3.4}$$

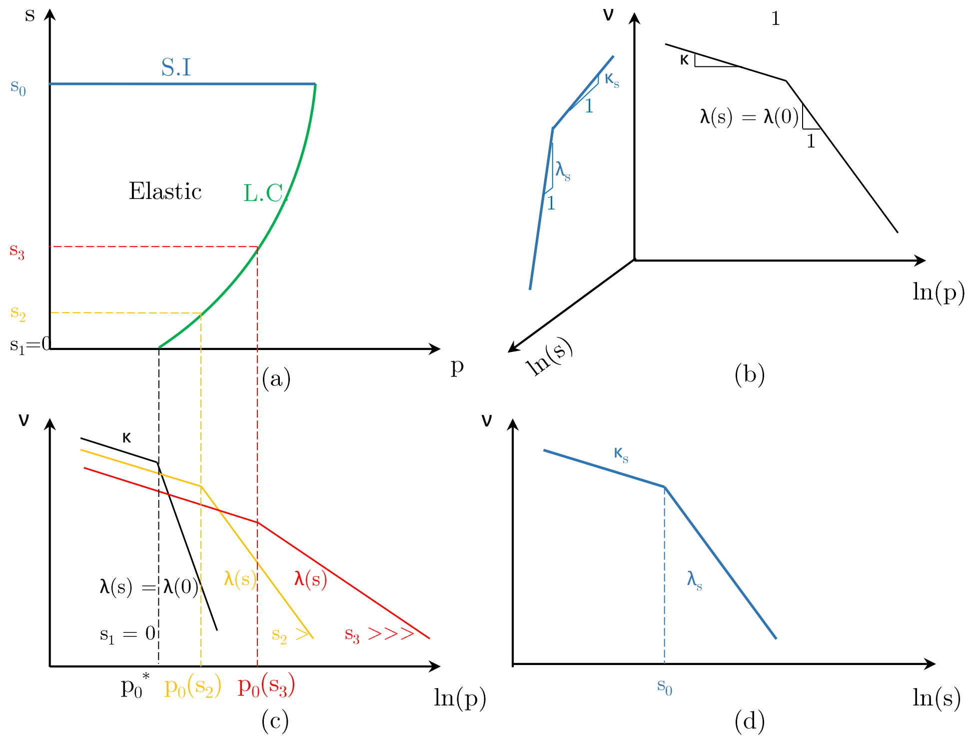

Figure 3.3: (a) Representation of the S.I. and L.C. curve in (s,p) space (b) Compression curves in v, s, p space (c) Compression curves for saturated and unsaturated soils in v, p space (d) Compression curves in v, s space for BBM (Alonso et al., 1990).

The effect of suction change on the compressibility and size of $p_0(s)$ are illustrated on Figure 3.3 (c). The three curves shown, from black to red, represent values for $\lambda(s)$ at different suctions. With the increase of suction, the compressibility of the soil decreases and the yield surface $p_0(s)$ increases in size as seen on Figure 3.3 (a). The parameters λ_s and κ_s are fixed as a constant for the sake of simplicity and therefore experience no change in value due to suction changes. This is reflected in Figures 3.3 (b) and (d).

Flow rules

The plastic strain increments (flow rule) associated with yield surface f_1 are $d\varepsilon_{vp}^p$ (volumetric plastic increment associated with the LC curve) and $d\varepsilon_q^p$ (deviatoric plastic increment associated with the LC curve) are defined as

$$\frac{d\varepsilon_{vp}^p}{d\varepsilon_q^p} = \frac{2q\alpha}{M^2(2p + p_s - p_0)} \tag{3.5}$$

where α is a non-associativity parameter defined. Assuming zero elastic deviatoric strain increment and K_0 stress conditions, α is defined by

$$\alpha = \frac{M(M-9)(M-3)}{9(6-M)} \frac{1}{1-\dfrac{\kappa}{\lambda(0)}} \tag{3.6}$$

The flow rule associated with f_2 is $(d\varepsilon_{vs}^{p}, 0)$, defined as

$$\frac{d\varepsilon_q^p}{d\varepsilon_{vs}^p} = 0 \tag{3.7}$$

where $d\varepsilon_{vs}^{p}$ is the volumetric plastic strain increment for the S.I. locus.

Hardening laws

The hardening law for the loading yield surface, f_1, is controlled by the hardening parameter p_0^*, which evolves as Equation 3.8 suggests

$$dp_0^* = \frac{(1+e)p_0^*}{\lambda(0)-\kappa} d\varepsilon_v^p \tag{3.8}$$

The hardening law governing yield surface f_2 is controlled by the evolution of the hardening parameter s_0. Its evolution depends on $d\varepsilon_v^p$ (total plastic volumetric strain) and is defined as

$$ds_0 = \frac{(1+e)(s_0+p_{\text{atm}})}{\lambda_s-\kappa_s} d\varepsilon_v^p \tag{3.9}$$

Elasticity

The volumetric and deviatoric elastic strains associated with changes in loading and suction are as follows:

$$d\varepsilon_v^e = \frac{\kappa}{v}\frac{dp}{p} + \frac{\kappa_s}{v}\frac{ds}{(s+p_{\text{atm}})} \tag{3.10}$$

$$d\varepsilon_q^e = \frac{1}{3G}dq = \frac{2(1+\nu)}{3E}dq \tag{3.11}$$

where κ is the elastic stiffness parameter associated with changes of stress and κ_s is the elastic stiffness parameter associated with changes of suction. A summary of the parameters required for the BBM and the way of calibrating them, are presented in Table 3.1.

Table 3.1: Summary of BBM parameters and calibration methods.

Parameter definition	Symbol	Units	Calibration method
Elastic parameters			
Elastic stiffness parameter during loading/unloading	κ	MPa^{-1}	Suction controlled oedometer test
Poisson's ratio	ν	–	Suction controlled oedometer test
Elastic stiffness parameter for changes in suction	κ_s	MPa^{-1}	Drying-wetting test cycle at a given net mean stress
Yield surface			
Critical state slope	M	–	Direct shear test
Pre-consolidation pressure	p_0^*	MPa	ICD triaxial or oedometer test
Reference stress	p_c	MPa	Suction controlled ICU triaxial or oedometer
Parameter in the LC curve	β	MPa^{-1}	Suction controlled ICU triaxial or oedometer
Parameter in the LC curve	r	–	Suction controlled ICU triaxial or oedometer
Stiffness parameter during suction changes	λ_s	MPa^{-1}	Drying-wetting test cycle at a given net mean stress
Plastic potential			
Non-associativity parameter	α	–	From M, κ, ν and $\lambda(0)$
Hardening law			
Virgin compressibility for saturated conditions	$\lambda(0)$	MPa^{-1}	Oedometer test

3.2.2 Rockfill compressibility model (RM)

The model used to simulate the rockfill response is an viscoplastic constitutive model based on the main principles of the Barcelona Basic Model (BBM) (Alonso et al., 1990). The stress variables for the RM are defined in the same manner as in BBM. The model captures the volumetric deformation behaviour of the rockfill that is based on a fracture propagation mechanism. This deformation mechanism is able to give a qualitative physical explanation of time-dependent strains and collapse strains of rockfill, and of their simultaneous dependence on stress and water action. Prior to description of the constitutive model, the main factors affecting the behaviour of rockfill are examined.

The Rockfill Model (Oldecop and Alonso, 2001) considers a linear relationship for the stress-strain response for both instantaneous and time dependent deformation of the material based on experimental data. The model is based on isotropic compressibility, elastic behaviour, yield stress function with a volumetric hardening law, critical state and has an extension for triaxial stress conditions with a yield and plastic potential functions.

Isotropic compressibility

The volumetric compressibility is assumed to be governed by two components. Under a threshold stress value, p_y, only the first mechanism occurs. It is called particle re-arrangement and involves slip and rotation of the particles in relation to their neighbours. The second mechanism is active beyond that threshold stress value and controls particle breakage. Isotropic compressibility is described as follows:

$$d\varepsilon_v = \lambda^i dp \qquad\qquad p \leq p_y \tag{3.12}$$

$$d\varepsilon_v = \lambda^i dp + \lambda^d(s) dp \qquad\qquad p > p_y \tag{3.13}$$

where $d\varepsilon_v$ is the incremental volumetric strain, p is the total mean net stress and λ^i is a compressibility parameter that governs the particle re-arrangement mechanism, where the superscript i stands for instantaneous deformation. The compressibility parameter $\lambda^d(s)$ represents the particle breakage mechanism, which is dependent on the total suction and captures some of the macroscopic phenomena observed in laboratory testing. The compressibility $\lambda^d(s)$ increases when the rockfill is wetted (decrease of suction). The superscript d shows the delayed nature of the particle breakage mechanism. Equation 3.14 appropriately captures this behaviour

$$\lambda^d(s) = \lambda_0^d - \alpha_s \ln\left(\frac{s + p_{atm}}{p_{atm}}\right) \tag{3.14}$$

where λ_0^d is rockfill compressibility at full saturation and α_s controls the rate of increase of rockfill stiffness due to suction increase. A visual representation of Equations 3.12 and 3.13 for different stress paths can be seen on Figure 3.4 (a).

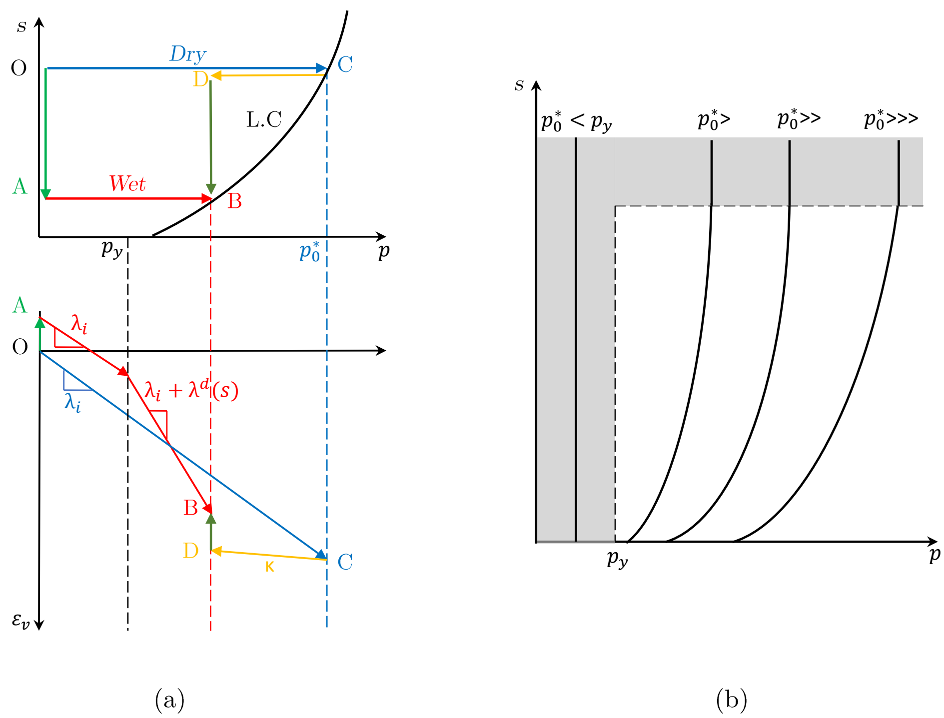

Figure 3.4: (a) Idealized model response for different stress paths (b) Yield surface (L.C. curve) for different values of p_0^* for RM.

Yield surface

Rockfill behaves in an non-associated manner and the yield function based on BBM is modified to obtain the potential function G. Both functions are shown below

$$\begin{aligned} F(p,q,s) &= q^2 - M^2(s)\,[p + p_s(s)]\,[p_0(s) - p] = 0 \\ G(p,q,s) &= q^2 - \alpha M^2(s)\,[p + p_s(s)]\,[p_0(s) - p] = 0 \end{aligned} \tag{3.15}$$

where α is a non-associativity parameter, $p_s(s) = k_s s$ is a shear strength parameter, linearly increasing with suction. $M(s)$ shows the effect of the suction on the critical state slope, varying between two extreme values: M_{dry} for very high values of suction and M_{sat} for $s = 0$, presented in Equation 3.16. The loading-collapse curve (LC) defines the set of $p_0(s)$ values for each associate suction. It can be considered as a set of yield curves in (p, s) space. The LC curve is defined in Equations 3.17 and 3.18.

$$M(s) = M_{\mathrm{dry}} - (M_{\mathrm{dry}} - M_{\mathrm{sat}}) \left(\frac{M_{\mathrm{sat}}}{M_{\mathrm{dry}}} \right)^{s/p_{\mathrm{atm}}} \tag{3.16}$$

$$p_0(s) = p_0^* \qquad\qquad p_0^* \leq p_y \tag{3.17}$$

$$p_0(s) = p_y + \frac{(\lambda^i - \kappa)(p_0^* - p_y)}{\lambda^i + \lambda^d(s) - \kappa} \qquad p_0^* > p_y \tag{3.18}$$

where p_0^* is the yield stress for the very dry rockfill material. Under the threshold value p_y, the behaviour does not depend on water content. This could be seen on Figure 3.4 (b), where the L.C. curve is shown in (s,p) space for different values of p_0^*. The yield surface is also represented in (p,q,s) space on Figure 3.5.

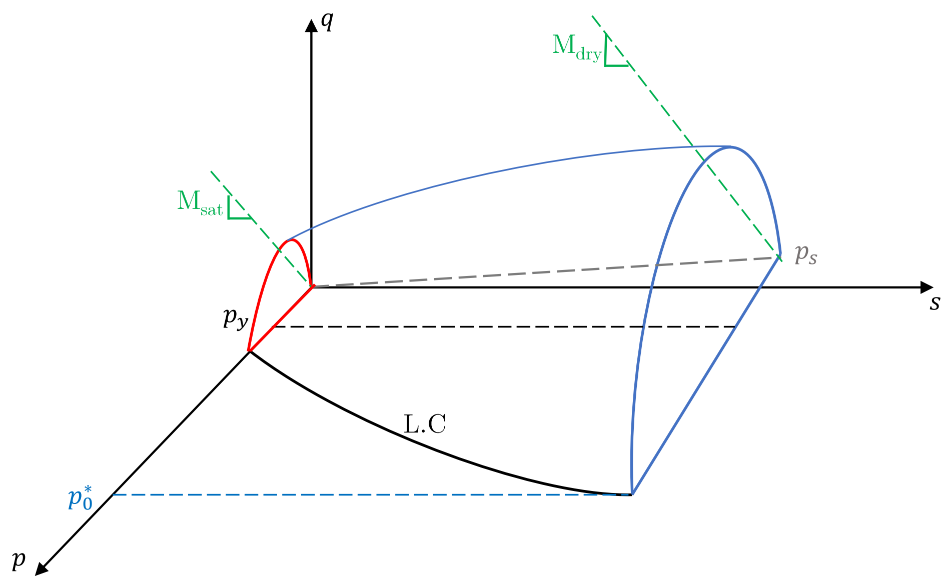

Figure 3.5: The dimensional view of the yield surfaces in (p,q,s) space for RM.

Flow rule

The constitutive model proposed in Oldecop and Alonso, 2001 is extended and a viscoplastic formulation is added in Alonso et al., 2005. Adding viscoplasticity to the model offers computational advantages because collapse behaviour can be viewed as a softening process and could result in numerical problems. Such instabilities happen because collapse concentrates in isolated elements while adjacent elements experience stress relaxation resulting in elastic behaviour. The viscoplastic approach homogenizes the spatial distribution of the collapse strains and prevents this numerical instability. The total strain is decomposed into elastic and viscoplastic in Equation 3.19. Equation 3.20 calculates the viscoplastic strain.

$$\dot{\varepsilon} = \dot{\varepsilon}^{e} + \dot{\varepsilon}^{vp} \tag{3.19}$$

$$\dot{\varepsilon}^{vp} = \Gamma \langle \phi(F) \rangle \frac{\partial G}{\partial \sigma} \tag{3.20}$$

where Γ is the fluidity parameter and $\langle \phi(F) \rangle$ is a flow function defined as

$$\langle \phi(F) \rangle = \phi(F) \qquad\qquad F > 0 \tag{3.21}$$

$$\langle \phi(F) \rangle = 0 \qquad\qquad F \leq 0 \tag{3.22}$$

$$\phi(F) = \left(\frac{F}{F_0} \right)^{N} \tag{3.23}$$

To achieve a solution close to the real elastoplastic solution, the fluidity parameter Γ must be increased sufficiently. Typical values are $\Gamma = 100$ and $N = 5$.

Hardening law

The model follows a volumetric hardening law that describes the evolution of p_0^*:

$$dp_0^* = \frac{d\varepsilon_v^p}{\lambda_i - \kappa} \tag{3.24}$$

where the volumetric plastic strain $d\varepsilon_v^p = d\varepsilon_v - d\varepsilon_v^e$.

Elasticity

The volumetric elastic strain of rockfill is dependent on the two compressibility coefficients κ and κ_s and the Poisson's ratio, ν. The swelling index κ_s is negligible in non-expansive materials and thus ignored here. The parameter κ_s is defined as follows:

$$d\varepsilon_v^e = \kappa dp = \frac{dp}{E}3(1-2\nu) \tag{3.25}$$

$$d\varepsilon_v^{es} = \kappa_s \frac{ds}{s+p_{atm}} \approx 0 \tag{3.26}$$

Creep

There is an extra feature in RM which simulates the long term behaviour of rockfill. The volumetric component of the "creep" behaviour is based on experimental data and is expressed as

$$\dot{\varepsilon}_v^c = \frac{d\varepsilon_v^c}{dt} = \frac{\lambda_t(p,s)}{t} = \frac{1}{\eta_v(s,t)}p \tag{3.27}$$

where $\eta_v(s,t)$ is a viscosity coefficient dependent on suction and time. It is expressed as

$$\frac{1}{\eta_v(s,t)} = \frac{\mu}{t}\left[1-\beta^c ln\left(\frac{s+p_{\text{atm}}}{p_{\text{atm}}}\right)\right] \tag{3.28}$$

where μ and β^c are constitutive parameters. To account for the deviatoric part of the "creep" strain, a tentative expression, which is not based on data, has been established as

$$\dot{\varepsilon}_d^c = \frac{d\varepsilon_d^c}{dt} = \frac{1}{3\eta_d(s,t)}q \tag{3.29}$$

where $\eta_d = a\eta_v$ and a is usually taken as 0.1. The total creep strain is calculated via the viscoelastic equation

$$\dot{\varepsilon}^c = \frac{1}{2\eta_d}(\sigma - pI) + \frac{1}{3\eta_v}pI \tag{3.30}$$

The formulation for the time dependent compressibility manages to capture its reliance on stress and suction observed in laboratory settings.

Differences with BBM

There are several differences between the BBM and the RM model. The first one is that compressibility relations for the rockfill are described by linear functions between stress and strain. The value of p_y (threshold stress) has no equivalent value for unsaturated soils. Another significant difference is the definition of the suction, s. In unsaturated soils s has a mechanical meaning and describes the capillary or matric component of suction. The role of suction in rockfill is to control the velocity of crack propagation within the particles. Therefore, s is used as a state variable that is externally controlled by boundary conditions and flow phenomena. The velocity of crack propagation depends on the relative humidity, or by the total suction. In the case of dams, the distinction between both definitions of suction is not significant because the chemical composition of water is not a relevant variable. The chemical composition of water governs the osmotic component of the total suction, but when it is not present this effect disappears and total and matric suction become identical.

For both BBM and RM constitutive models, the suction variable s is controlled by the flow phenomena and the assigned boundary conditions. This is done through using a unique water retention curve for each material, relating s with the current saturation, S_r, of the material. In the case of rockfill, however, the S_r refers to relative humidity that is inside the particle cracks and not, as in the standard definition of S_r, the amount of water in the pore space between the particles.

A summary of the constitutive model equations for BBM and RM are presented in Table 3.2 for comparison purposes. The parameters required by RM are summarized in Table 3.3 and a short description of the calibration methods is included.

Table 3.2: Basic relationships for BBM and RM*. Table adopted from Alonso et al. (2005).

	Barcelona Basic Model (BBM) (Alonso et al., 1990)	Rockfill Model (RM) (Compressibility part described in Oldecop & Alonso, 2001)
Isotropic elastoplastic volumetric deformation	$d\varepsilon_v = \frac{\lambda(s)}{(1+e)}\frac{dp}{p}$	$d\varepsilon_v = \lambda^i dp \quad p \le p_y$ $d\varepsilon_v = \lambda^i dp + \lambda^d(s)dp \quad p > p_y$
Volumetric compressibility index	$\lambda(s) = \lambda(0)\left[(1-r)\exp(-\beta s) + r\right]$	$\lambda_i + \lambda^d(s)$ $\lambda^d(s) = \lambda_0^d - \alpha_s ln\left(\frac{s+p_{atm}}{p_{atm}}\right)$
Hardening law	$dp_0^* = \frac{(1+e)p_0^*}{\lambda(0)-\kappa}d\varepsilon_v^p$	$dp_0^* = \frac{d\varepsilon_v^p}{\lambda_i-\kappa}$
Loadingcollapse curve (LC)	$p_0(s) = p^c\left(\frac{p_0^*}{p^c}\right)^{\frac{\lambda(0)-\kappa}{\lambda(s)-\kappa}}$	$p_0(s) = p_0^* \quad p_0^* \le p_y$ $p_0(s) = p_y + \frac{(\lambda^i-\kappa)(p_0^*-p_y)}{\lambda^i+\lambda^d(s)-\kappa} \quad p_0^* > p_y$
Shear strength critical-state parameter	$M(s) = M$	$M(s) = M_{\mathrm{dry}} - (M_{\mathrm{dry}} - M_{\mathrm{sat}})\left(\frac{M_{\mathrm{sat}}}{M_{\mathrm{dry}}}\right)^{s/p_{\mathrm{atm}}}$
Tensile strength parameter	$p_s = k_s s$	
Yield surface (triaxial)	$F = 3J_{2D} - \frac{M^2(s)}{9}(J_1 + 3k_s s)\left[3p_0(s) - J_1\right] = 0$	
Plastic potential (triaxial)	$G = 3J_{2D} - \frac{\alpha M^2(s)}{9}(J_1 + 3k_s s)\left[3p_0(s) - J_1\right] = 0$	
Creep strain		$\frac{d\varepsilon_v^c}{dt} = \frac{1}{\eta_v(s,t)}p \qquad \frac{d\varepsilon_d^c}{dt} = \frac{1}{3\eta_d(s,t)}q$ $\frac{1}{\eta_v(s,t)} = \frac{\mu}{t}\left[1 - \beta^c ln\left(\frac{s+p_{\mathrm{atm}}}{p_{\mathrm{atm}}}\right)\right]$ $\eta_d = a\eta_v$

* A common notation was used for equivalent parameters. Material parameter values are different for the rockfill and soil

Table 3.3: Summary of RM parameters and calibration methods.

Parameter definition	Symbol	Units	Calibration method
Elastic parameters			
Young's modulus	E	MPa	Unloading stage – oedometer test
Poisson's ratio	ν	–	Material property
Plastic behaviour			
Plastic virgin instantaneous compressibility	$\lambda^i - \kappa$	MPa^{-1}	Loading stage under dry conditions at low stress – oedometer test
Virgin clastic compressibility for saturated conditions	λ_0^d	MPa^{-1}	Loading stage under saturated conditions – oedometer test
Parameter describing the rate of change of compressibility with suction	α_s	–	Flooding of dry sample under constant stress
Slope of critical-state strength envelope for dry conditions	M_{dry}	–	Friction angle of dry material, ϕ_{dry} – DSS
Slope of critical-state strength envelope for saturated conditions	M_{sat}	–	Friction angle of saturated material, ϕ_{sat} – DSS
Parameter that controls the increase in cohesion with suction	k_s	–	From the cohesive intercept – ICU triaxial/oedometer test
Threshold yield mean stress for the onset of clastic phenomena	p_y	MPa	Flooding of dry sample under constant stress (collapse strain); Flooding of dry sample under low stress (expansion strain); ICU triaxial/oedometer test
Parameter that defines the non-associativeness of plastic potential	α	–	Material parameter
Creep			
Creep coefficient for saturated conditions	μ	MPa^{-1}	Suction controlled oedometer test under constant stress
Parameter that controls the influence of suction on creep rate	β^c	–	Suction controlled oedometer test under constant stress

3.3 Hydraulic models

3.3.1 Van Genuchten hydraulic model

The water retention curve shows the relation between capillary pressure (suction) and degree of saturation (S_r) of various materials. Typically, it is used in unsaturated soils with high plasticity and the suction variable refers to the suction within the pores between the particles. In the case of rockfill, however, the suction is found within the cracks of the particle, instead of in between the pores of the particles. Also, the saturation in rockfill refers to the relative humidity located, again, inside the particle cracks. One model in particular seems to capture well the shape of those curves and it is the model described in van Genuchten (1980). The Van-Genuchten equation implemented in Code_Bright (2015) is

$$S_r = \frac{S_l - S_{lr}}{S_{ls} - S_{lr}} = \left[1 + \left(\frac{u_a - u_w}{P}\right)^{1/(1-\lambda_{\text{van}})}\right]^{-\lambda_{\text{van}}} \tag{3.31}$$

where S_r is the degree of saturation (cm^3/cm^3), which varies between 0 and 1, S_l is equivalent saturation ratio, $P = \sigma P_0/\sigma_0$, σ_0 is surface tension at temperature at which P_0 was measured (usually 0.072N/m), P_0 is the air entry value of the material, λ_{van} is an exponent parameter, S_{ls} is maximum saturation and S_{lr} is residual saturation. By definition, the suction $s = u_a - u_w$. An example of four water retention curves is presented in Figure 3.6 to show the effect of the most dominant parameters in this equations, which are P_0 and λ_{van}.

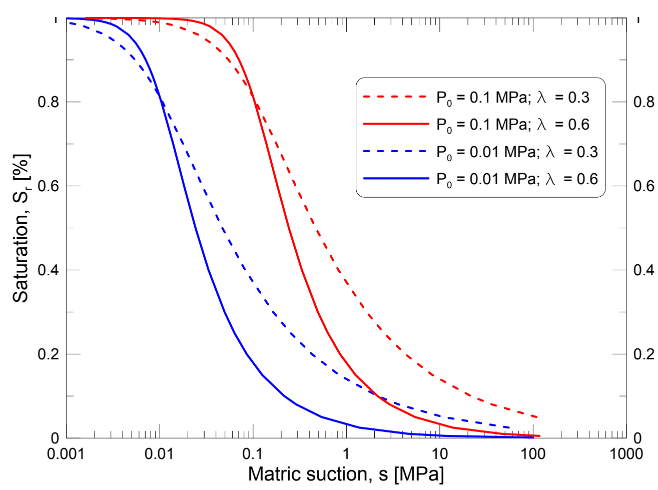

Figure 3.6: Water retetion curves with varying P_0 and λ_{van} parameters.

Typically, for rockfill, the value for P_0 is lower than 0.01 MPa and for clay/till materials, P_0 could go as high as 0.5 MPa. Values for λ_{van} are typically 0.6 for rockfill and 0.3 for clay.

3.3.2 Liquid phase relative permeability

The relative permeability introduces the effect of partial saturation on intrinsic permeability. The function is notated with $K_r(S_r)$ and varies between 0, for dry soil, and 1 for fully saturated soil. The function acts as a multiplier to the intrinsic permeability as

$$K = k\frac{\rho_w g}{\mu_w}K_r(S_r) \tag{3.32}$$

where K is the hydraulic conductivity (m/s), k is the intrinsic permeability (m^2), g is the gravitational constant (m/s^2) and μ_w is the dynamic viscosity of the water (kg/m.s) and ρ_w is the density of water (kg/m^3). There are different simple laws that express the reduction of permeability with decrease of saturation. In the present work, a power law is selected as

$$K_r(S_r) = AS_r^m \tag{3.33}$$

where A is a constant, usually taken as 1, m is the exponent, usually taken as 10 for rockfill and 3 for clay core. In the case of rockfill, having a higher exponent results in $K_r(S_r)$ becoming 0 for degree of saturation more than 0.3. This equates to water freely percolating within the saturated rockfill pores. Visual representation of the power law can be seen on Figure 3.7, adopted from Alonso et al. (2005).

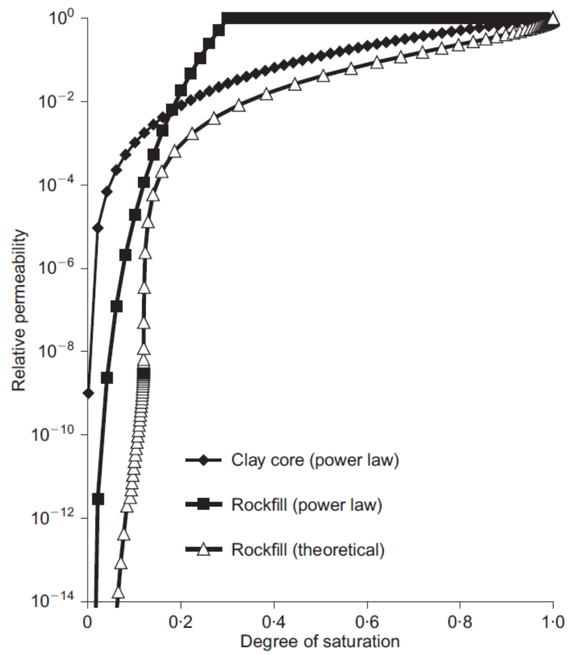

Figure 3.7: Varying relative permeability for clay and rockfill materials (Alonso et al., 2005).

Chapter 4

Description of the numerical model

4.1 Finite element software

The numerical simulation is set up in a finite element platform called Code_Bright, developed at the Polytechnic University of Catalonia (Code_Bright, 2015). This is a two dimensional FEM software for coupled Thermo-Hydro-Mechanical analysis in geological media. The theory consists of a set of governing equations and a set of constitutive laws. The code is developed in FORTRAN and consists of multiple subroutines. Code_Bright uses GiD as pre and post-processing tool (Coll et al., 2016). GiD is an interactive graphical user interface that is used to prepare the numerical model of the dam for analysis. The data defined in GiD includes setting up the geometry, material parameters used by Code_Bright, initial and boundary conditions, solution information, time intervals and time step definition. Meshing of the model is done after introducing all of the described data. Constitutive laws in GiD are defined by entering a combination of material parameters. For example, to use the Rockfill compressibility model, material parameters have to be filled for Linear Elasticity, Viscoplastic General Parameters 1,2 and 3 in the "Mechanical Parameters 1" section of the software. In the next sections, the constitutive models that are used for modelling the dam, are explored in depth, including an explanation of the parameters involved.

4.2 Geometry and zoning

The model of the dam has been built layer by layer in accordance with real life construction and impoundment stages. The whole simulation captures the construction and full impoundment of the dam reservoir, lasting for 5 years. The geometry has been exported from Hydro Quebec's DXF file in GiD 12.0.7. The height of the dam is 171 m and it reaches to an elevation of 410 m. A local coordinate system is placed with its X origin to be along the centre of the till core. The next two subsections show the numerical model layer discretization and the constitutive models assigned for the different materials.

4.2.1 Geometry and model layers

The geometry of the dam is divided into multiple layers with depth of around 20 m as shown in Figure 4.1.

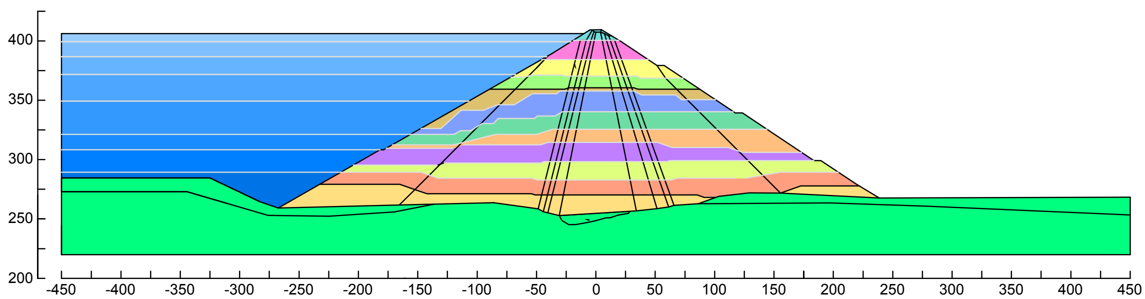

Figure 4.1: Construction sequence of dam for model calculations.

The layer discretization has been obtained from the provided DXF file, assuring that the layers are constructed exactly as in the field. This process guarantees a more accurate representation of the construction sequence than simulating idealized horizontal layers. Construction has been simulated by adding layers to an initial geometry of the alluvial foundation and bedrock. The weight of each layer has been applied in a ramp manner in order for the layer to reach full weight at the end of the construction time interval. Detailed information regarding the time intervals, construction and impoundment are provided in Section 4.5.

4.2.2 Constitutive models assigned to material zones

Figure 4.2 describes all the material zones.

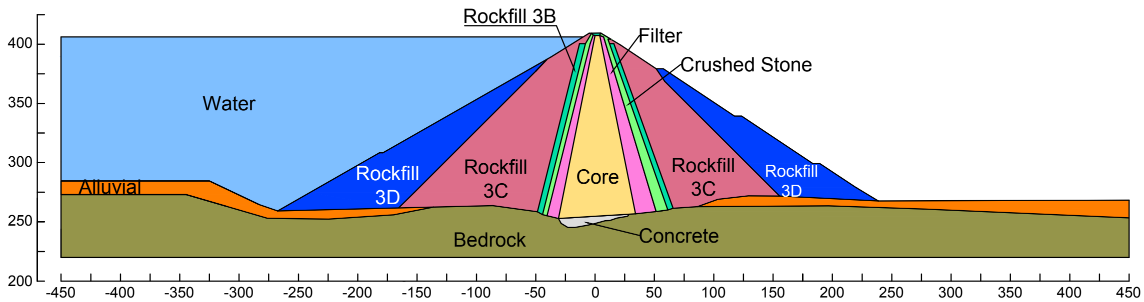

Figure 4.2: Denis-Perron dam material zones.

Table 4.1 exhibits the respective constitutive model assigned to the material zones.

Table 4.1: Assigned constitutive models to dam zones.

Dam Zones	Constitutive Model
Rockfill Shells (3C, 3D)	RM
Transition (Rockfill 3B)	RM
Drain and Filter	BBM
Till Core	BBM
Alluvial Foundation	BBM
Bedrock	LE
Concrete	LE
Water	LE

4.3 Material parameters

Each of the material zones requires a set of parameters in order to solve the stress equilibrium and flow equations. Generally, a set of mechanical parameters to describe the LE, BBM or RM models are needed. Each of these three constitutive models require different parameters as shown in Chapter 3.

Another set of parameters needed are the hydraulic parameters. They include the definition of a water retention curve and intrinsic permeability. The final set of parameters for each material is the initial values for porosity and suction. Subsections 4.3.1 to 4.3.4 investigate the calibration of the parameters for the materials in Table 4.1.

4.3.1 Till core

The core is constructed out of a glacial till material. A suitable constitutive model for this type of material is the BBM. To use the BBM in Code_Bright, a combination of linear elasticity and viscoplasticity for unsaturated soils is used. The laboratory and field data provided are not sufficient to derive all necessary material parameters for the numerical simulation. A similar glacial till material from Northern Quebec has been thoroughly examined in the work of Watabe et al. (2000). Twelve samples, H-01 to H-12, under different compaction and saturation conditions have been tested. Figures 4.3a and 4.3b show the compaction curves and the hydraulic conductivities for the twelve samples respectively.

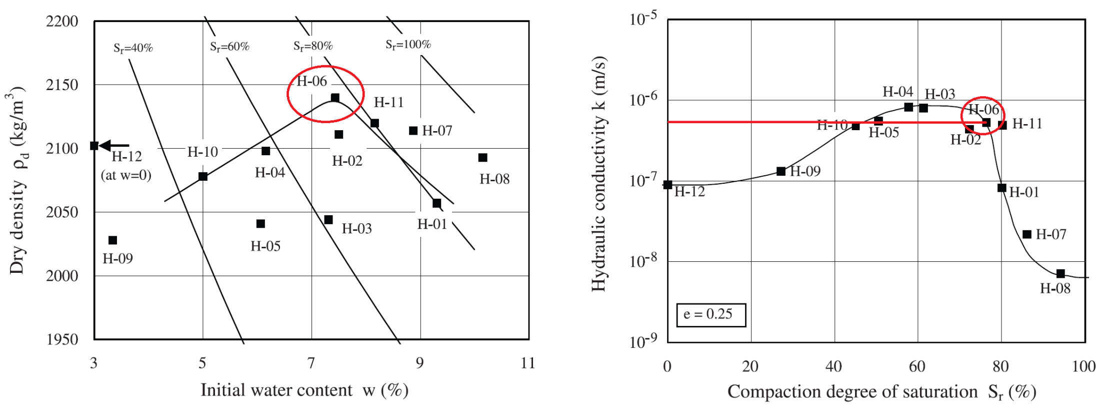

(a) **(b)**

Figure 4.3: (a) Standard Proctor compaction curve for all samples tested (b) Hydraulic conductivity as a function of the compaction degree of saturation. Figures modified from Watabe et al. (2000).

Sample H-06 has suitable physical characteristics and is chosen based on a few criteria described in Table 4.2, exhibiting similarities with the SM3 glacial till material. Hydraulic parameters are derived based on hydraulic conductivity and water retention curve of that sample. Mechanical parameters are derived based on an oedometer test performed on sample H-06. Derivation of those parameters is explored in the next subsections.

Table 4.2: Comparison of H-06 glacial till material physical characteristics with SM3 glacial till material.

Physical parameter/definition	Value and/or Reference	
	H-06 Sample	SM3 Sample
Soil classification	Glacial Till	Glacial Till
Grain size distribution	Figure 2.14	Figure 2.14
Maximum average dry density, $\rho_{\mathrm{d,max,average}}$	2135 kg/m^3	2137 kg/m^3; Table 2.2
Void ratio	0.25	0.24; Table 2.3
Hydraulic conductivity, K	7×10^{-7} m/s; Figure 4.3b	$1 \times 10^{-7} - 1 \times 10^{-10}$ m/s
Water content after compaction, w_f	7.5 %	7.3 %; Table 2.3

Hydraulic parameters

The intrinsic permeability is calculated using Equation 4.1

$$k = K \frac{\mu_w}{\rho_w g} \tag{4.1}$$

From the permeability tests it is established that $K = 7 \times 10^{-7}$ m/s. Using Equation 4.1, $k = 7.2 \times 10^{-14}$ m^2. Permeability is assumed to be isotropic as no anisotropy has been reported.

The water retention curve has been estimated from Watabe et al. (2000) for the till core material. The curve varies based on compaction conditions, thus an average was taken (thick red line) shown on Figure 4.4a. To capture the shape of the retention curve, the van Genuchten (1980) law is used. A plot of the water retention curve with the estimated parameters for Equation 3.31 is shown on Figure 4.4b with the thick blue line.

Sample H-06's saturation is reported as $S_r = 0.76$. Using the retention curve from Figure 4.4b, a value for the initial suction is calculated as $s = 0.01$ MPa. The hydraulic parameters are summarized in Table 4.3.

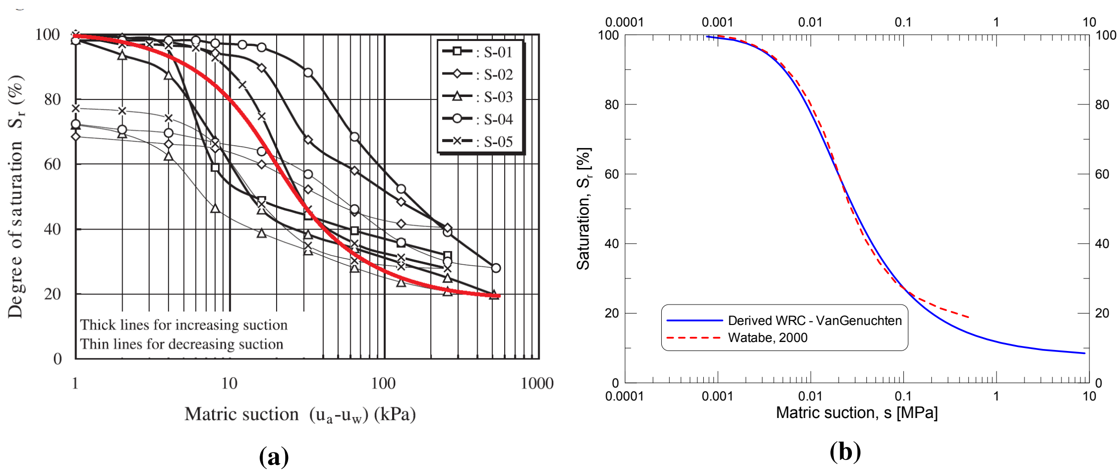

Figure 4.4: (a) Soil characteristic curves for till samples in Watabe et al. (2000). Red line shows an average curve. (b) Fitted curve (blue) to averaged soil characteristic curve using van Genuchten (1980).

Table 4.3: Hydraulic parameters for the till core.

Definition of parameter	Symbol	Value	Units
Intrinsic Permeability	k	7.2×10^{-14}	m^2
Water Retention Curve (van Genuchten, 1980)			
Pressure at $T = 20°$	P_0	0.01	MPa
Maximum Saturation	S_{ls}	1	–
Residual Saturation	S_{lr}	0.075	-
Curve Shape Defining Exponent	λ	0.4	–
Liquid phase relative permeability			
Model constant	A	1	–
Model exponent	m	3	–
Initial Suction (applied as an initial condition to model)	s_0	0.01	MPa

Mechanical parameters

The parameters for the BBM are calibrated based on oedometer data for sample H-06. The oedometer test is simulated in Code_Bright with a 10×10 mesh. The initial suction for the test is $s_0 = 0$ MPa ($S_r = 100\%$). The initial porosity is $n = e/(1+e) = 0.195$. The initial suction and porosity are both applied as initial surface boundary conditions. The saturation level of the sample is kept constant during the test by applying a constant liquid pressure equal to the suction level corresponding to the given saturation. Ramp loading is applied as a boundary condition on the top surface of the oedometer. The results of the tests can be seen on Figure 4.5.

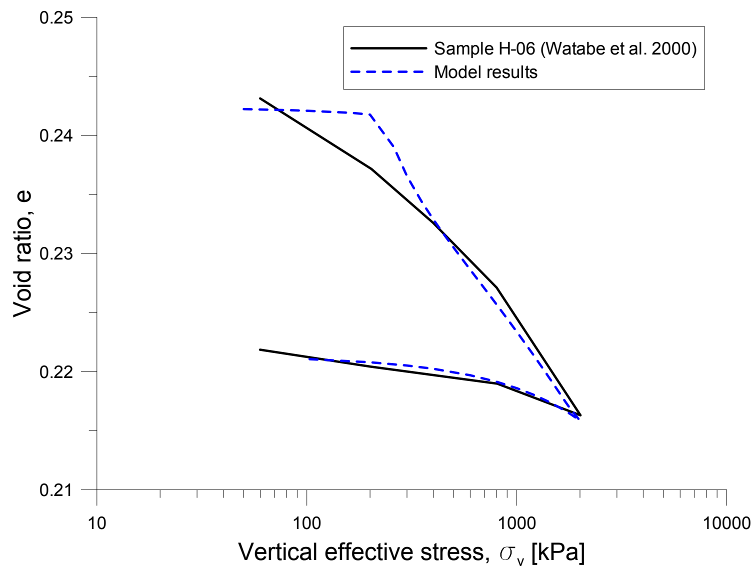

Figure 4.5: Oedometer test on compacted till from Northern Quebec, sample H-06 (Watabe et al., 2000).

The parameters calibrated with the test are:

- Elastic parameters - E and ν using the unloading stage of the test
- Virgin compressibility parameter using the data from the loading stage - $\lambda(0)$
- Viscoplasticity parameters for the general shape of the loading stage - Γ and N

The model does not seem to capture the behaviour of the till at lower stresses in the range of 100 to 300 kPa, experiencing less volume change than what the laboratory data is suggesting.

The slope of the critical state line is estimated based on the reported angle of friction, $\phi = 39$ (SNC-Shawinigan, 1996), using Equation 4.2.

$$M = \frac{6\sin(\phi)}{3-\sin(\phi)} \tag{4.2}$$

The non-associated parameter α is calculated based on Equation 4.3 (Vaunat, 2015).

$$\alpha = \frac{M(M-9)(M-3)}{9(6-M)} \frac{1}{1-\dfrac{\kappa}{\lambda(0)}} \tag{4.3}$$

The parameters governing the LC curve could not be calibrated due to a lack of suction controlled experiments. The effect of suction on the compressibility is considered low for this material due to the high density. Suction values of the till material are in the low range (less than 0.05 MPa) due to the high initial saturation. Thus, the compressibility value is very close to the maximum value (when $S_r = 100\%$). A summary of the mechanical parameters is shown in Table 4.4.

4.3.2 Rockfill material

Three different rockfill material zones are considered in the analysis. The inner (Rockfill 3C) and outer shells (Rockfill 3D) of the dam have the most significant impact on the dam behaviour. Therefore, they will be the focus of this study. The transition zone (Rockfill 3B) is composed of the same material, but with smaller maximum particle diameter of 450 mm. All of the three zones are modelled with the RM model. For the base case, the constitutive model parameters will be the same for all three rockfill materials.

According to Errecalde (2012) the rockfill particles are composed of biotite and anorthosite. Biotite is characterized by a foliated structure, which favours development of many microcracks. The higher the amount of microcracks in the particles, the more settlement is expected. During the compaction process, the material has been placed without sluicing. The omission of sluicing causes more collapse during the first impoundment due to the nature of rockfill response.

Hydraulic parameters

Due to a lack of provided data for rockfill, the hydraulic properties are established based on literature. Previous research has shown that rockfill intrinsic permeability varies between $k = 1 \times 10^{-8}$ m^2 and $k = 1 \times 10^{-12}$ m^2. In the case of Beliche dam (Alonso et al., 2005), the intrinsic permeability of the rockfill is $k_{\text{Beliche}} = 2 \times 10^{-11}$ m^2 for a rockfill with porosity of $n = 0.35$. In the case of

Table 4.4: Mechanical parameters for the till core.

Definition of parameter	Symbol	Units	Value
Elastic behaviour			
Elastic modulus	E	MPa	300
Poissons ratio	ν	–	0.33
Plastic behaviour			
Virgin compressibility for saturated conditions	$\lambda(0)-\kappa$	MPa^{-1}	0.011
Parameter that establishes the minimum value of the compressibility for high suction	r	–	0.7
Parameter that controls the rate of increase in stiffness with suction	β	MPa^{-1}	0.6
Reference stress	p_c	MPa	0.001
Slope of critical-state strength line	M	–	1.6
Parameter that controls the increase in cohesion with suction	k_s	–	0
Parameter that defines the non-associativeness of plastic potential	α	–	0.46
Viscoplasticity			
Fluidity parameter	Γ	s^{-1}	1000
Flow function exponent	N	-	6

Lechago dam (Alonso et al., 2012), the intrinsic permeability of the rockfill is $k_{\text{Lechago}} = 1 \times 10^{-12}$ m^2 for a rockfill with porosity of $n = 0.30$. Examining the work of Konrad et al., 2011, rockfill intrinsic permeability could go as high as $k = 1 \times 10^{-8}$ m^2. It is safe to assume that the intrinsic permeability for Denis-Perron is somewhere in the middle, $k_{\text{SM3}} = 1 \times 10^{-10}$ m^2. A more detailed study regarding the sensitivity of the intrinsic permeability is carried out in Chapter 6.

Data for the water retention characteristics of the rockfill is missing, therefore, a water retention curve is estimated from literature. The model used to describe the curve is van Genuchten (1980). A suitable water retention curve is adopted from Errecalde (2012). Figure 4.6 conveys the water retention curve used in the analysis of SM3 dam in blue. The Figure also exhibits the water retention curves used for Beliche and Lechago dams for comparison purposes.

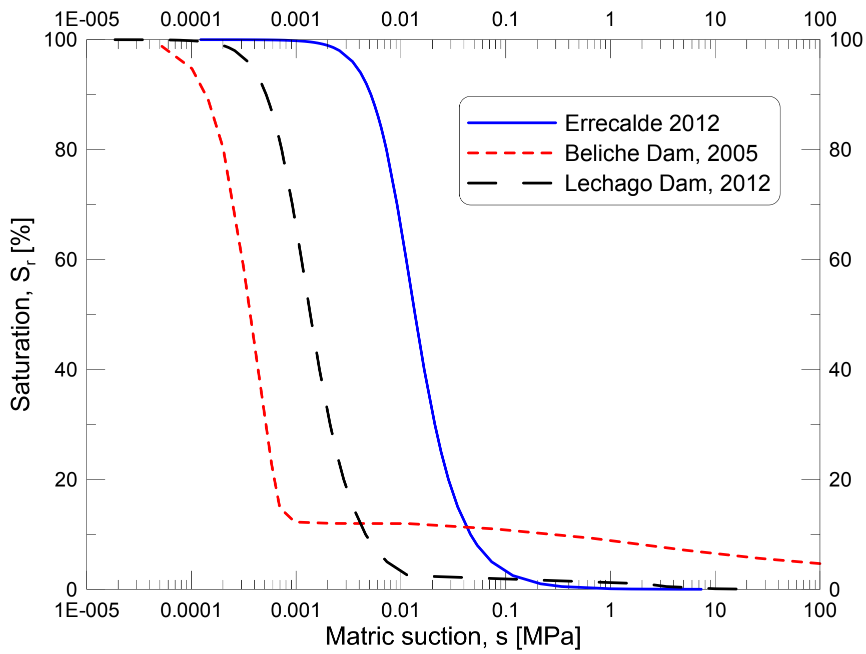

Figure 4.6: Water retention curves for rockfill material: Beliche Dam (Alonso et al. (2005)), Lechago Dam (Alonso et al. (2012)) and Denis-Perron Dam (Errecalde (2012)).

It is very difficult to estimate initial saturation of the rockfill in the field and no information for this is available. This value depends in the way the rockfill has been placed in the field. If there has been sluicing involved, the initial saturation should be considered higher and therefore initial suction is lower. If the rockfill has not been placed with sluicing, the initial saturation should be considered lower, which causes higher long term settlements. The oedometer test on the rockfill material is carried out at a relative humidity of 30% ($S_r = 30\%$). The initial saturation for the numerical simulation is assumed to be the same due to no other information available. Using the water retention curve from Figure 4.6, the initial suction is calculated to be $s_0 = 0.007$ MPa. The hydraulic parameters for the inner and outer shells are summarized in Table 4.5.

Table 4.5: Hydraulic parameters for the rockfill shells.

Definition of parameter	Symbol	Units	Rockfill	
			Inner Shell	Outer Shell
Intrinsic Permeability	k	m/s	1×10^{-10}	1×10^{-10}
Water Retention Curve (Van Genuchten, 1980)		–		
Pressure at $T = 20°$	P_0	MPa	0.01	0.01
Maximum Saturation	S_{ls}	–	1	1
Residual Saturation	S_{lr}	–	0	0
Exponent Defining Curve Shape	λ	–	0.6	0.6
Liquid phase relative permeability				
Model constant	A	–	1	1
Model exponent	m	–	10	10
Initial Suction (applied as an initial condition to model)	s_0	MPa	0.007	0.007

Mechanical parameters

Oedometer tests have been performed on dry and saturated material with a reported scaled grain size distribution, where the coefficient of uniformity, C_u, of the oedometer and the field material is preserved. The oedometer device has a diameter of 300 mm; the maximum particle size for the tested material is estimated to be 1/5th of that, i.e. about 60 mm. The mechanical parameters of the rockfill compressibility model are calibrated using oedometer data. Similar to the element test for the till material, the oedometer test is simulated in Code_Bright with a 10×10 mesh at two different saturations: $S_r = 30\%$ for the dry sample and $S_r = 100\%$ for the flooded sample. The saturation levels of the sample is established by applying a constant liquid pressure equal to the suction level corresponding to the given saturation: $s = 0.007$ MPa for $S_r = 30\%$ and $s = 0$ MPa for $S_r = 100\%$. In the case of rockfill S_r corresponds to the relative humidity of the material, meaning the saturation within the cracks of the particles, instead of the saturation in the pores between the particles. The boundary condition is applied to the top and bottom boundaries of the sample. Results of the simulation are illustrated on Figure 4.7.

The porosity of the sample is calculated from Equation 4.4 on a reported saturated unit weight of $\gamma_{sat} = 22$ kN/m^3 and an assumed $G_s = 2.7$ (SNC-Shawinigan, 1996). The porosity is then calculated as 0.27 and is applied as an initial surface boundary condition to the element test.

$$\gamma_{sat} = (G_s(1-n)+n)\gamma_w \tag{4.4}$$

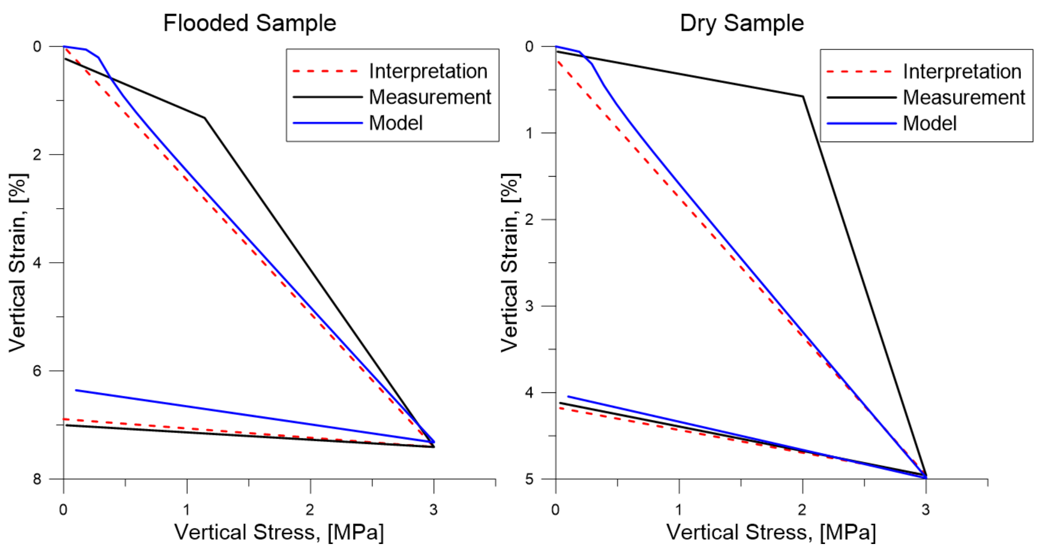

Figure 4.7: Oedometer test data and model results for wet ($S_r = 100\%$) and dry ($S_r = 30\%$) rockfill samples.

Elasticity parameters, E and ν, are estimated based on the unloading. It seems like the unloading slope of the two samples is influenced by the level of saturation. The compressibility parameters λ_i and λ_0^d are calibrated based on the loading slopes of the two tests. The rate of change of compressibility parameter α_s is also calibrated according to the oedometer test. M_{dry} and M_{sat} are assumed to correspond to $\phi_{max} = 45^\circ$ and $\phi_{min} = 42^\circ$ respectively (SNC-Shawinigan, 1996). No increase in cohesion is reported and thus $k_s = 0$. A low value for the threshold stress p_y is assumed because deformations are seen to occur nearly instantaneously. The mechanical parameters are summarized in Table 4.6, showing a comparison between the parameters used in Beliche Dam's inner rockfill shell. The rockfill material in SM3 has lower compressibility than the rockfill from Beliche due to the higher quality of the material used. The analysed experimental data are not sufficient to discriminate with accuracy between different model parameters. Oedometer tests under suction control are required for a precise determination of the parameters $(\lambda_i - \kappa)$, λ_0^d and α_s.

Calibration of the constitutive model parameters μ and β_c could be obtained from a suction controlled oedometer test, providing values for λ^t at different suction. Such calibration has been completed for the quartzitic shale used in the analysis of Beliche dam (Alonso et al. (2005)) and a visual representation of the calibration procedure is shown on Figure 4.8.

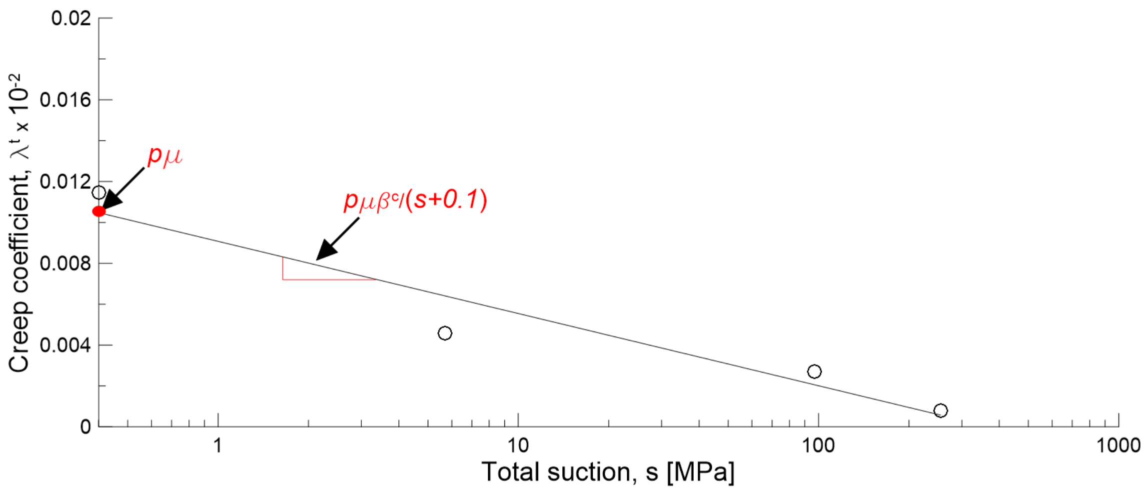

Figure 4.8: Calibration of parameters μ and β^c based on data from Figure B.8 (a).

The relation to "real time" is shown in the constitutive description of RM in equation 3.29.

4.3.3 Drain, filter and alluvial foundation

The drain and filter are relatively small in size and do not affect the dam settlements significantly. For simplicity purposes and the lack of laboratory data, the two materials are modelled as one.

The focus of this study is on the rockfill settlements during construction and impoundment, therefore a detailed examination of the foundation is not conducted. The rockill shoulders lay predominately on bedrock and thus the effect of this thin layer of alluvial material is considered negligible.

Table 4.6: Mechanical parameters for the rockfill shells.

Definition of Parameter	Symbol	Units	Rockfill Shoulders SM-3	Rockfill Shoulders Beliche Inner Shell
Elastic behaviour				
Elastic Modulus	E	MPa	400	150
Poisson's ratio	ν	–	0.3	0.3
Plastic behavioor				
Plastic virgin instantaneous compressibility	$\lambda^i - \kappa$	MPa^{-1}	0.010	0.025
Virgin clastic compressibility for saturated conditions	λ_0^d	MPa^{-1}	0.009	0.028
Parameter describing the rate of change of clastic compressibility with total suction	α_s	–	0.02	0.01
Slope of critical-state strength envelope for dry conditions	M_{dry}	–	1.85	1.75
Slope of critical-state strength envelope for saturated conditions	M_{sat}	–	1.7	1.3
Parameter that controls the increase in cohesion with suction	k_s	–	0	0
Threshold yield mean stress for the onset of clastic phenomena	p_y	MPa	0.005	0.01
Parameter that defines the non-associativeness of plastic potential	α	–	0.3	0.3
Creep				
Creep coefficient for saturated conditions	μ	MPa^{-1}	0.0012	0.0012
Parameter that controls the influence of suction on creep rate	β^c	–	0.083	0.083
Viscoplasticity				
Fluidity parameter	Γ	s^{-1}	100	N/A
Flow function exponent	N	–	5	N/A

Hydraulic parameters

The permeability of the drain and filter materials is assumed to be the same as the one for the transition zone. The water retention curve of the material is considered the same as the one for the till material. For more detailed and accurate representation of those zones, more experimental data is required.

The hydraulic parameters for the alluvial foundation are taken from the work of Alonso et al. (2005). The hydraulic properties are summarized in Table 4.7

Table 4.7: Hydraulic parameters for the drain, filter and the alluvial foundation.

Definition of parameter	Symbol	Units	Value	
			Drain and Filter	Foundation
Intrinsic Permeability	k	m^2	1×10^{-10}	1×10^{-11}
Water Retention Curve (Van Genuchten, 1980)				
Pressure at $T = 20°$	P_0	MPa	0.01	0.1
Maximum Saturation	S_{ls}	–	1	1
Residual Saturation	S_{lr}	–	0	0
Exponent Defining Curve Shape	λ	–	0.5	0.27
Liquid phase relative permeability				
Model constant	A	–	10	10
Model exponent	m	–	10	10
Initial Suction (applied as an initial condition to model)	s_0	MPa	0.01	0.002

Mechanical parameters

The drain and filter are considered to exhibit similar behaviour as the till core, but with decreased stiffness and decreased compressibility. They are modelled with BBM and values for material parameters are adopted from the work of Errecalde (2012). Data for the dry densities is available and is used to calculate the porosity of the materials. The maximum average dry density of the two materials is $\rho_{dry,average} = 2146$ kg/m^3. Assuming $G_s = 2.7$ and using Equation 4.5, the average porosity of the material becomes $n = 0.21$.

$$\rho_d = (1-n)G_s\rho_w \tag{4.5}$$

Table 4.8: Mechanical parameters for drain, filter and alluvial foundation.

Definition of parameter	Symbol	Units	Materials		
			Drain	Filter	Alluvial
Elastic behaviour					
Elastic modulus	E	MPa	100	100	400
Poissons ratio	ν	–	0.3	0.3	0.3
Plastic behaviour					
Virgin compressibility for saturated conditions	$\lambda(0)-\kappa$	MPa^{-1}	0.006	0.006	0.038
Parameter that establishes the minimum value of the compressibility, for high suction	r	–	0.8	0.8	0.75
Parameter that controls the rate of increase in stiffness with suction	β	MPa^{-1}	0.4	0.4	0.4
Reference stress	p_c	MPa	0.001	0.001	0.01
Slope of critical-state strength line	M	–	1.1	1.1	1.45
Parameter that controls the increase in cohesion with suction	k_s	–	0	0	0
Parameter that defines the non-associativeness of plastic potential	α	–	0.3	0.3	0.3
Viscoplasticity					
Fluidity parameter	Γ	s^{-1}	100	100	100
Flow function exponent	N	–	5	5	5

The alluvial foundation is modelled with the BBM and parameters are obtained from the work of Alonso et al. (2005). The summarized material properties are presented in Table 4.8

4.3.4 Bedrock, concrete and water

The bedrock, the concrete at the bottom of the core and the water material are modelled as linear elastic materials. The bedrock and concrete behave as very stiff materials and values taken for their parameters are standard.

The water is defined as a linear-elastic material in Code_Bright Code_Bright (2015). Instead of applying a hydrostatic pressure as most commercial codes handle hydro-mechanical problems, here the water is considered as a highly porous and soft material that gets "filled up" with liquid as the impoundment is happening. This method has been verified and validated as a good approximation of reality, both by the Code_Bright creators and the author of current work. For validation of the method, refer to Appendix A. This way of simulating the reservoir impoundment is a new feature in the software and brings a few advantages:

- The first one is from a practical point of view. It drastically reduces the manual labour. The standard way of impounding is by calculating the pore pressures and the corresponding mechanical pressures (weight of water) for each of the depths and assigning it manually to the upstream surfaces of the dam for each time interval. By using the new method, only one value has to be calculated per interval and only one boundary condition has to be applied per time interval. Also, no mechanical pressures have to be calculated to simulate the weight of the water.

- In addition, computation time is reduced. Applying only one boundary condition, compared to multiple ones, reduces the computation time.

- Lastly, rainfall impact with the reservoir surface can be simulated due to the presence of an available water surface. In standard numerical modelling, the water is artificially introduced and no actual water surface is present.

Hydraulic parameters

The hydraulic properties for the bedrock, concrete and water are presented in Table 4.9. The zero suction for the bedrock and concrete translates to a saturation of 100 %. The assigned suction of 0.1 MPa for the water simulates the atmospheric pressure. The water retention curves for the bedrock and concrete are not of importance, because those materials are under the water table level and are fully saturated during the whole simulation. The water retention curve for the water is obtained from the tutorial examples in Code_Bright (2015), showing how to use this new method of simulating the reservoir rising.

Table 4.9: Hydraulic parameters for bedrock, concrete and water.

Definition of parameter	Symbol	Units	Value		
			Bedrock	Concrete	Water
Intrinsic Permeability	k	m^2	1×10^{-12}	1×10^{-12}	1×10^{-10}
Water Retention Curve (Van Genuchten, 1980)					
Pressure at $T = 20^{\circ}$	P_0	MPa	0.1	0.1	0.001
Maximum Saturation	S_{ls}	–	1	1	1
Residual Saturation	S_{lr}	–	0	0	0
Exponent Defining Curve Shape	λ	–	0.3	0.3	0.33
Initial Suction (applied as an initial condition to model)	s_0	MPa	0	0	0.1

Mechanical parameters

The values for E and ν for the bedrock and concrete are standard - very high values for E and smaller ν. The used $E = 5$ MPa and $\nu = 0.49$ for the water guarantees very high bulk modulus and low shear modulus. The high porosity and intrinsic permeability guarantees fast percolation of water within the material. The mechanical parameters for the three materials are summarized in Table 4.10.

4.4 Initial and boundary conditions

For the code to solve the hydro-mechanical equations, it needs initial and boundary conditions. Every boundary condition is assigned during the appropriate time interval. The time intervals are explored in detail in Section 4.5.

Table 4.10: Mechanical properties for bedrock, concrete and water.

Definition of parameter	Symbol	Units	Value		
			Bedrock	Concrete	Water
Young's Modulus	E	MPa	1800	5000	5
Poisson's ratio	ν	–	0.15	0.15	0.49
Porosity (applied as an initial condition to model)	n	–	0.18	0.18	0.9

4.4.1 Boundary conditions

The necessary boundary conditions for the Denis-Perron dam are:

- Mechanical boundary conditions - applied as line conditions
  - X and Y displacement constraints at the bottom boundary of the foundation (applied as 0 displacement rate in the X and Y directions)
  - X displacement constraints at the side boundaries of the model (applied as 0 displacement rate in the X direction)
- Hydraulic (flux) boundary conditions - applied as line conditions
  - Impermeable boundary conditions are applied at the bottom and sides of the model
  - The seepage boundary condition is applied on the face of the dam, allowing for water to flow out
  - The atmospheric boundary condition is applied on the dam boundaries to simulate rainfall
  - The nodal flow with prescribed pressure is assigned at the bottom of the "Water" material to simulate impoundment of the dam

The assigned mechanical and hydraulic (flux) boundary conditions are shown on Figure 4.9. Details regarding the impoundment stages are discussed in subsection 4.5.2.

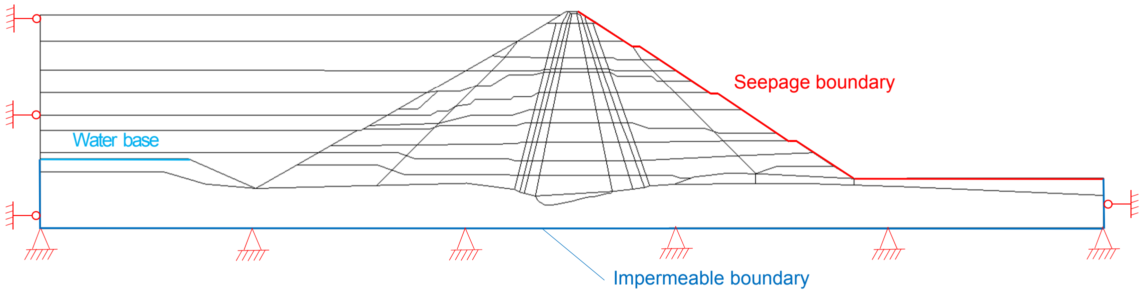

Figure 4.9: Mechanical and hydrauilic boundary conditions.

4.4.2 Initial conditions

The necessary initial conditions for the Denis-Perron dam are applied as surface conditions and are the following:

- Initial suction values assigned to the model internal surfaces to simulate the initial saturation of the materials
- Initial porosity values assigned to the model internal surfaces

Figure 4.10 illustrates the initial suction values that the software uses as a state variable in the constitutive models. The values are assigned to dam surfaces as an "Initial unknown". Suction is defined as $s = P_g - P_l$, where P_g is gas pressure and P_l is liquid pressure. In the software P_g is assumed to be 0, therefore, $P_l = -s_0$, where s_0 is the initial value of suction calculated in Section 4.3. For the water this value is 0.1 MPa, which represents the atmospheric pressure (1 atm).

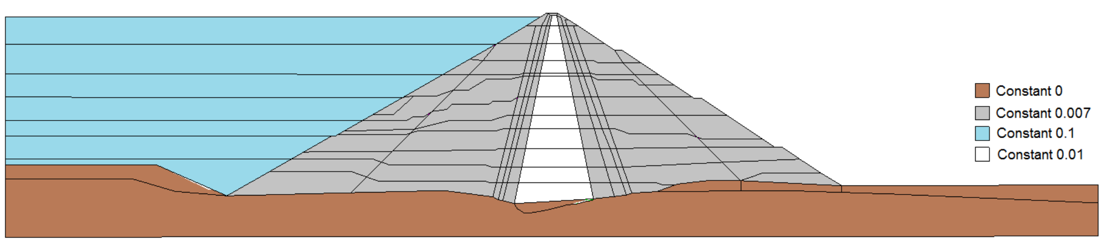

Figure 4.10: Initial suction values for the material zones.

In Code_Bright, porosity is assigned as an initial condition to the geometry's surfaces. The values for each material are calculated in Section 4.3 and the values assigned to the model are shown in Figure 4.11. It must be noted that the initial conditions apply only for the initial activation of the given layer. For example, if the foundation is placed during Interval 1 with an applied initial porosity of 0.18, the porosity condition for Interval 2 would be calculated based on the equilibrium equations solved by the code. Even if an initial porosity is assigned for the same material in Interval 2, this value is ignored.

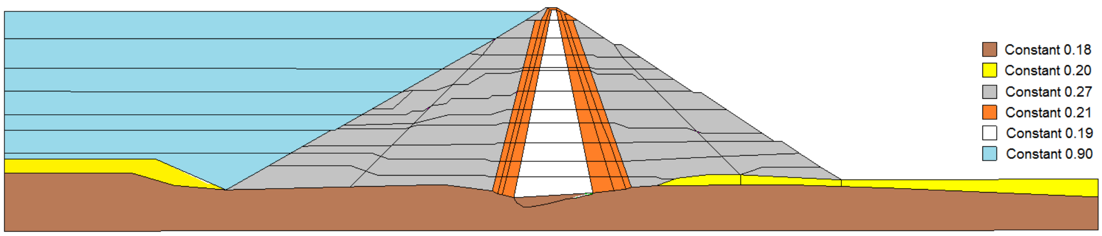

Figure 4.11: Initial porosity values for the material zones.

4.5 Time intervals

The intervals in Code_Bright control the application of loading (i.e. construction stages) and application of boundary and initial conditions (i.e. reservoir impoundment). Each time interval has a length in units of time. In the case of SM3, the time intervals are defined in days.

4.5.1 Construction stages

Each layer is constructed during a time interval with the length representing the time it took for construction of the layer in real life. Communicating the interval in which the given layer needs to be constructed (activated) is done through the “Construction Excavation” tab in the material parameters. This construction process usually involves reduction in material stiffness, but due to low initial pre-consolidation stress ($p_0^* = 0.02$ MPa) applied to the layers, there is no need for such reduction (Alonso et al., 2005). The construction stages of the dam are illustrated in Figure 4.12.

Visualization of the construction sequence from placement of foundation, to full construction and impoundment of the dam, is presented on Figure 4.14. The construction stages and impoundment are shown in Figure 4.13. The brown line represents the dam elevation with respect to time and is obtained based on the construction sequence shown in Figure 4.12.

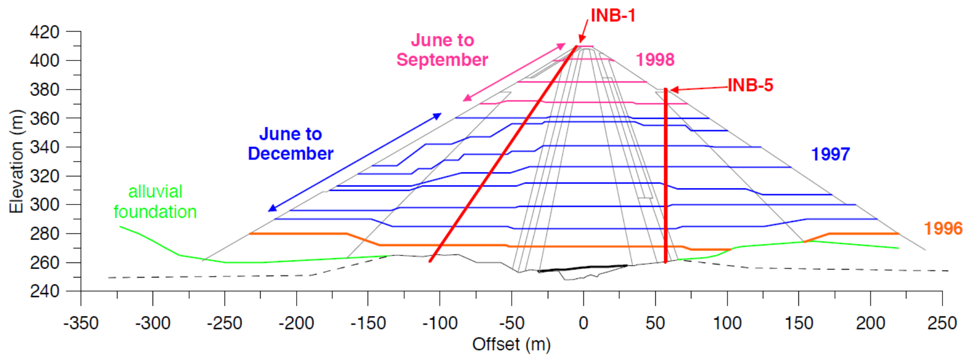

Figure 4.12: Construction sequence of the dam between 1996 and 1998 according to Péloquin (2015).

The top X axis on Figure 4.13 shows the construction sequence in terms of dates, with a beginning date 8/27/96 and is chosen as $t = 0$ days in the simulation. The end date is 01/01/2003 which is the end of the impoundment stage and is equivalent to $t = 2320$ days in the simulation, as shown on the bottom X axis. The solid blue line represents the reservoir level measured and the dashed red line is the equivalent simulation reservoir level. The impoundment is simulated as a hydraulic (flux) boundary condition in GiD and is described in the next subsection.

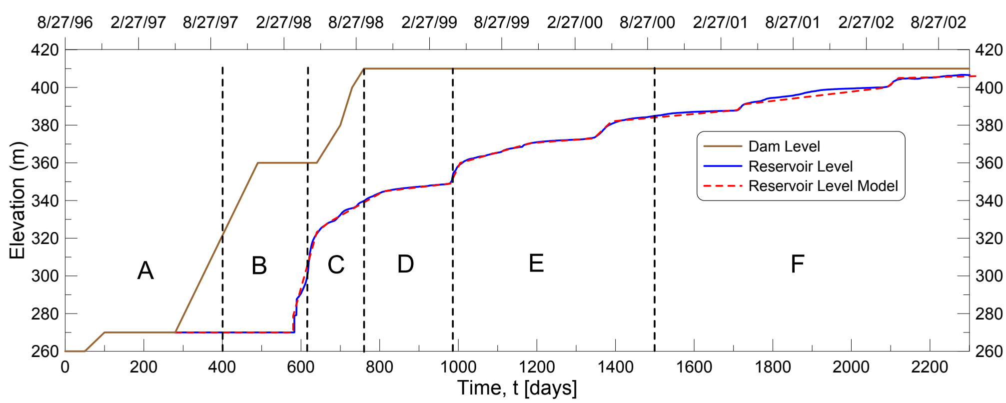

Figure 4.13: Dam construction and impoundment sequence in real life and the numerical model.

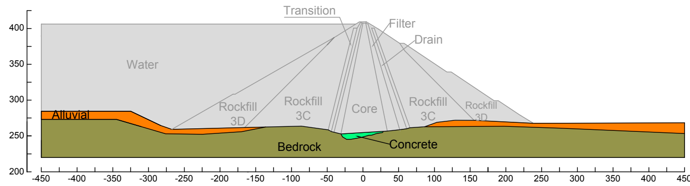

(a) Foundation construction.

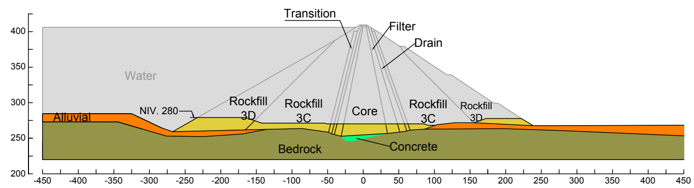

(b) 1996: Dam construction.

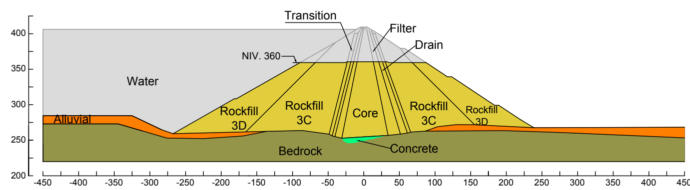

(c) Jun – Dec 1997: Dam construction.

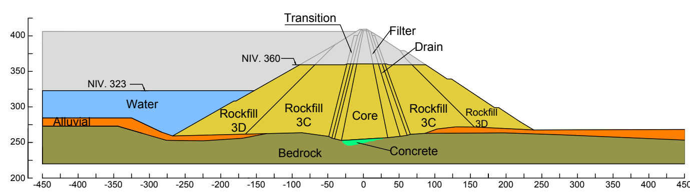

(d) Mar – May 1998: Impoundment

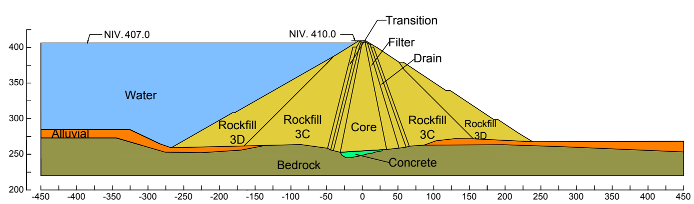

(e) Jun 1998 – Jan 2003: Impoundment

Figure 4.14: Visualization of construction sequence and impoundment simulated in Code_Bright.

4.5.2 Impoundment stages

The water is modelled as a highly porous material, with high bulk modulus and low stiffness as described earlier in the chapter. In order to simulate the impoundment, a hydraulic (flux) boundary condition is applied at the base of the "Water" material (light blue line on Figure 4.9). For each interval a "Prescribed Liquid Pressure", a "Prescribed Liquid Pressure Increment" and "Gamma for Liquid" are prescribed. The "Prescribed Liquid Pressure" (PLP for short) defines the starting water pressure in the reservoir, i.e. $u_{PLP} = h_{reservoir} \times \gamma_w = 0.1$ MPa for water height of 10 m. "Prescribed Liquid Pressure Increment" (PLPI for short) defines how much the liquid pressure during that interval will increase, i.e. $u_{PLPI} = h_{increase} \times \gamma_w = 0.1$ MPa for an additional impoundment of 10 m. "Gamma for Liquid" controls the speed of impoundment and direction of flow, i.e. if it is a negative value, seepage occurs (red line on Figure 4.9) and if it is 0, the boundary is impermeable (dark blue line on Figure 4.9).

The impoundment is the only boundary condition that varies with the time intervals. The prescribed liquid pressures for each interval are shown in columns 5 and 6 in Table 4.11. Columns 3 and 4 show the interval lengths in days and Column 2 shows the corresponding beginning date for that interval. Columns 7 and 8 show the time steps associated with the intervals in order to reach convergence.

4.5.3 Rainfall stages

In the past, rainfall has been shown to affect the behaviour of rockfill dams. In some cases, partial wetting can have the same effect as full flooding. Such examples are the Beliche dam (Naylor et al., 1997) and the Martin Gonzalo Dam. Most computational models have not been able to capture this behaviour, but Code_Bright in combination with the Rockfill Model have the capabilities to do that.

Figure 4.15 shows precipitation values recorded at the Denis-Perron dam site in mm. Standard precipitation data shows values in mm and is the measurement of water height in the span of 24 hour increments.

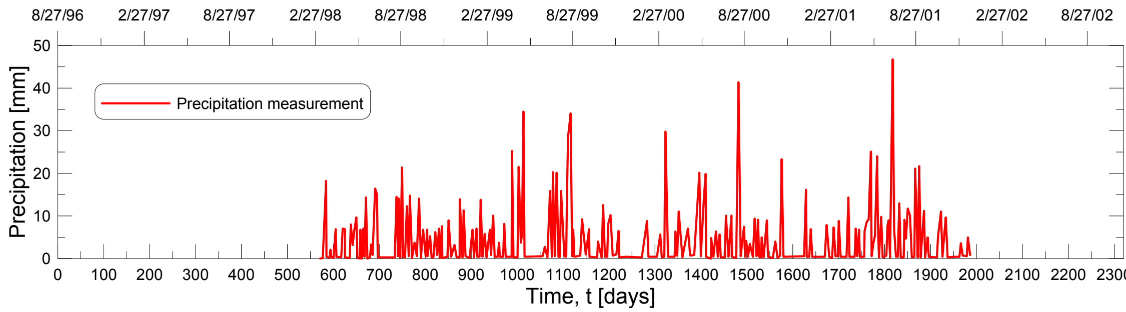

Figure 4.15: Precipitation data recorded in the field. Data digitized from Hammamjil (2003).

Therefore, to obtain the proper units, mm/s, each data point from 4.15 is divided by 24×3600 sec. The rainfall information is incorporated in the analysis through means of an "Name_atm.dat" file placed in the simulation folder. The file is linked through an atmospheric boundary condition. The boundary condition is introduced on the current exposed surface of the dam geometry. It is then removed from the surface of a given layer as soon as a new layer is constructed. The precipitation data is placed in the "Name_atm.dat" file in units of mm/s and the time is in units of seconds. The rainfall flow is imposed as a function of time rather than dependent on the time intervals, the way impoundment is simulated.

Table 4.11: Description of time intervals details and impoundment boundary condition associated with each interval.

Interval	Start Date	Start [Days]	End [Days]	Prescribed Liquid Pressure [MPa]	Prescribed Liquid Pressure Incr. [MPa]	Initial Time Step [Days]	Partial Time Step [Days]
1	1996-08-27	0	50			0.01	0.1
2	1996-10-16	50	100			0.01	0.01
3	1996-12-05	100	280			1	0.01
4	1997-06-03	280	310			1.00E-08	0.01
5	1997-07-03	310	340			1.00E-08	0.1
6	1997-08-02	340	370			0.01	0.1
7	1997-09-01	370	400			0.01	0.01
8	1997-10-01	400	430			0.1	0.01
9	1997-10-31	430	460			0.001	0.01
10	1997-11-30	460	490			0.01	0.01
11	1997-12-30	490	508			0.01	0.001
12	1998-01-17	508	526			0.001	0.01
13	1998-02-04	526	544			0.001	0.01
14	1998-02-22	544	562			0.001	0.01
15	1998-03-12	562	580			0.001	0.01
16	1998-03-30	580	640	0	0.374	0.001	0.01
17	1998-05-29	640	670	0.374	0.0510	0.01	0.01
18	1998-06-28	670	700	0.425	0.034	0.1	0.001
19	1998-07-28	700	730	0.460	0.035	0.0001	0.001
20	1998-08-27	730	760	0.495	0.034	0.01	0.001
21	1998-09-26	760	810	0.529	0.057	0.01	0.01
22	1998-11-15	810	980	0.587	0.040	0.01	0.01
23	1999-05-04	980	1005	0.627	0.107	0.01	0.01
24	1999-05-29	1005	1185	0.735	0.103	0.01	0.01
25	1999-11-25	1185	1345	0.838	0.024	0.01	0.01
26	2000-05-03	1345	1390	0.863	0.088	0.01	0.01
27	2000-06-17	1390	1710	0.951	0.058	0.01	0.01
28	2001-05-03	1710	1725	1.010	0.029	0.01	0.01
29	2001-05-18	1725	2090	1.039	0.088	0.01	0.01
30	2002-05-18	2090	2120	1.128	0.049	0.01	0.01
31	2002-06-17	2120	2320	1.177	0.009	0.001	0.01

4.6 FE mesh

4.6.1 Mesh description

For a 2D simulation, four element types are available for use:

- Linear triangle. It is primarily used in flow problems. Those elements are not recommended for incompressible media
- Linear quadrilateral with four integration points and a modified B matrix. This avoids locking when the medium is highly incompressible.
- Quadratic triangle with three integration points
- Zero thickness element

For the initial used of the code, linear triangular elements were used and provided satisfactory results. Using a higher degree of elements (quadrilateral) later on caused instability in the code and convergence could not be achieved past time = 730 days. Therefore, due to time limitations, the research was continued using linear triangular elements. The usage of those elements in nearly incompressible media could result in shear locking and some under-prediction of displacements takes place. Results are compared between the simulations with the two meshes at time = 730 days and the difference in the results is less than 5%, thus the results are considered reliable and the linear triangular elements are used for the rest of the research.

The finite element mesh is composed of 2968 3-node triangular elements as shown on Figure 4.16. The nodes can have up to six degrees of freedom (u_x, u_y, u_z, P_l, P_g, T). In the case of SM3, only three degrees of freedom are used. Horizontal (u_y) and vertical (u_z) displacements and water pressure (P_l). Even though the mesh is composed of linear triangle elements, the simulation time is around 7-8 hours.

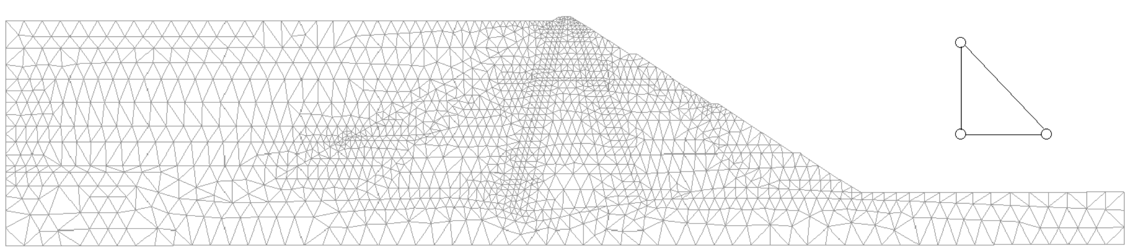

Figure 4.16: Finite element mesh of Denis-Perron dam.

4.6.2 Mesh quality

The quality of mesh is determined based on a few different criterion. Two criterion are examined. The first one is “Shape quality”. The quality criterion measures the likeness of the element to the reference one. In the case of a triangular element, the reference element is a equilateral triangle. The value is 1 for a perfect element (the reference element), and it decreases as the element becomes worse. The value is defined by Equation 4.6

$$q = \frac{4\sqrt{3}\text{Area}}{\sum_{i=1}^{3} l_i^2} \tag{4.6}$$

where Area is the triangle area and l_i (i=1,2,3) are the triangle edges. The value becomes negative if the element has a negative Jacobian matrix. Figure 4.17 (a) shows the cumulative plot for the Shape quality of the FE mesh elements. Less than 10 elements have quality under 0.5 and all of the elements have quality above 0.177.

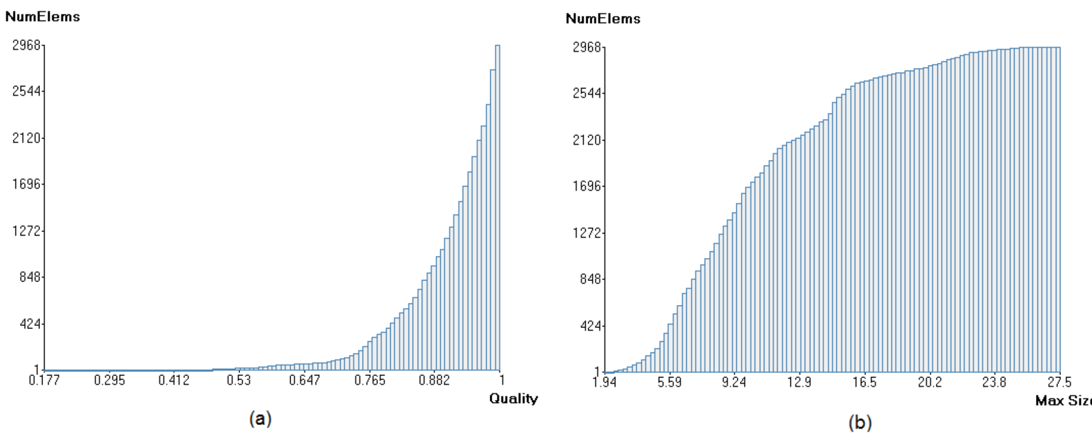

Figure 4.17: (a) Shape quality (b) Maximum edge cumulative distrobution.

The second criterion for mesh quality is based on element size. Figure 4.17 (b) shows the cumulative distribution of elements based on maximum edge size. All of the elements within the dam have maximum element edge less than 17 m. The elements with sizes between 17 and 27.5 m are in the foundation and/or water material. The element size is sufficiently small for the purposes of this research. In the case for the need of dynamic analysis, the mesh has to be refined in order to capture the wave propagation correctly.

4.7 Solution scheme

An important part of the description of the numerical model is showing the definition of the "Problem Data" and the "Interval Data". In the "Problem Data" menu, the first task is to assign the value for gravity which is -9.81 in the Z direction. The second step is to tell the software what equations are desired to be solved. In the current model, the equations solved are the "The stress equilibrium (unknown displacement u)" and the "Mass balance of water (unknown liquid pressure PL)". The air pressure is assigned to be a constant value of $P_g = 0$ and the temperature to be constant $T = 20°$. In this model, an Updated Lagrangian Method is not used due to the small magnitude of displacements expected.

The third step is to define the "Solution Strategy". The Solver is assigned as "direct LU+Back3"; the Elemental relative permeability is computed from the average nodal degree of saturation; the convergence criterion is "on nodal correction or residual". The rest of the Solution Strategy parameters are summarized in Table 4.12.

Table 4.12: Solution scheme data.

Parameter	Units	Value	Comments
Epsilon (Intermediate time for nonlinear functions)	–	1	Position of intermediate time $t^{k+\varepsilon}$ for matrix evaluation, i.e. the point where the non-linear functions are computed. (usual values: 0.5, 1)
Theta	–	1	Position of intermediate time $t^{k+\theta}$ for vector evaluation i.e. the point where the equation is accomplished
Time step control	–	7	Controls time stepping by means of a prediction based on the relative error deviation in the variables (relative error less than 0.001). Recommended value: 7
Max number of iterations per time step	–	10	Maximum number of Newton Raphson iterations per time step. If the prescribed value is reached, time step is reduced
Max Absolute Displacement	[m]	1E-4	Maximum (absolute) displacement error tolerance. When correction of displacements (displacement difference between two iterations) is lower than this value, convergence is achieved
Max Nodal Balance Forces	[MN]	1E-8	Maximum nodal force balance error tolerance. If the residual of forces in all nodes are lower than this value, convergence is achieved
Displacement Iteration Correction	[m]	1E-1	Maximum displacement correction per iteration (time increment is reduced if necessary)
Max Abs. PI	[MPa]	1E-3	Maximum (absolute) liquid pressure error tolerance
Max Nodal Water Mass Balance	[kg/s]	1E-8	Maximum nodal water mass balance error tolerance
PI Iteration Correction	[MPa]	1	Maximum liquid pressure correction per iteration (time increment is reduced if necessary)

Chapter 5

Base case simulation results

5.1 Introduction

The construction and impoundment of the Denis-Perron dam is simulated using the material parameters summarized in Tables 4.3 to 4.10. This case represents the base case. Different aspects of response like pore water pressure, degree of saturation, vertical stress, vertical and horizontal displacements are explored. The presented in this chapter are presented in this chapter in time series, contour plots or a spacial variation at a given snapshot in time.

For each of the selected response, if available, comparison with field measurements is made. The aim of this is to give a qualitative and quantitative measurement of the model performance and accuracy. The results are compared to the instruments investigated in Chapter 2. Other more general results are explored as well.

Figure 5.1 shows all the locations within the dam that are used for assessing the simulation results. Points labelled PPB 381, PPB 342, PPB 302 and PPB 272 are used to compare simulation results with field measurements of pore water pressures within the till core. Pressure cells measurements of vertical stress are compared at points CPB 251 and CPB 255. A horizontal cut through the dam is examined at chosen snapshots in time to explore the stress distribution. Inclinometer results during and post construction are compared at lines labelled INB1 and INB5. The points labelled with B0-28, B0-09 and B0-5 are used to compare simulation results with field measurements of vertical and horizontal displacements. Additionally, B0-28 and B0-9 are also used in parallel with Points 1 to 4 in order to investigate the progression of the degree of saturation and the pore water pressures in the rockfill.

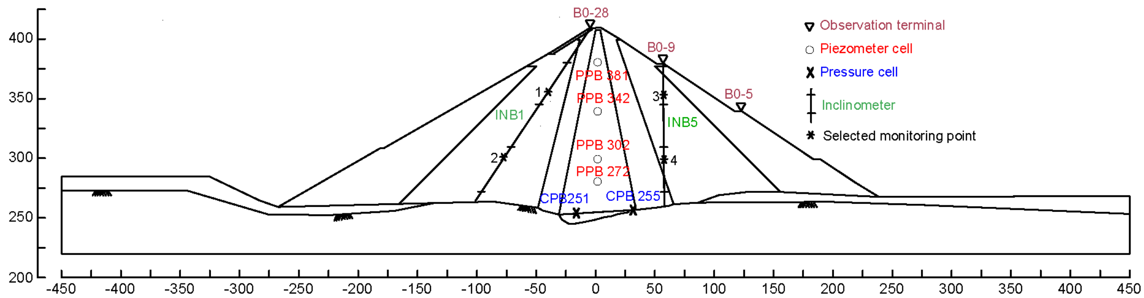

Figure 5.1: Summary of instruments and selected monitoring points used in analysis of simulation results.

The simulation time is divided into six intervals, as presented in Chapter 2, representing different stages of construction and impoundment. When referring to a "Time [A]" when presenting results, it refers to the end of time interval [A].

- A Construction to elevation 320m
  $t = 0 - 400$ days
- B Construction to elevation 360m; Impounding of the reservoir to elevation 292m
  $t = 400 - 610$ days
- C Completion of construction to elevation 410m; Impounding of the reservoir to elevation 343m
  $t = 610 - 760$ days
- D Impounding of the reservoir to elevation 350m
  $t = 760 - 980$ days
- E Impounding of the reservoir to elevation 382m
  $t = 980 - 1500$ days
- F Completion of reservoir impoundment to elevation 405m
  $t = 1500 - 2320$ days

5.2 Pore water pressure

5.2.1 General results

There are no available field measurements of the pore pressures within the rockfill zones. Therefore, simulation results are examined in order to understand the behaviour of the rockfill and the occurring displacements. Figure 5.2 shows the evolution of pore water pressure for points in the upstream and downstream rockfill shells.

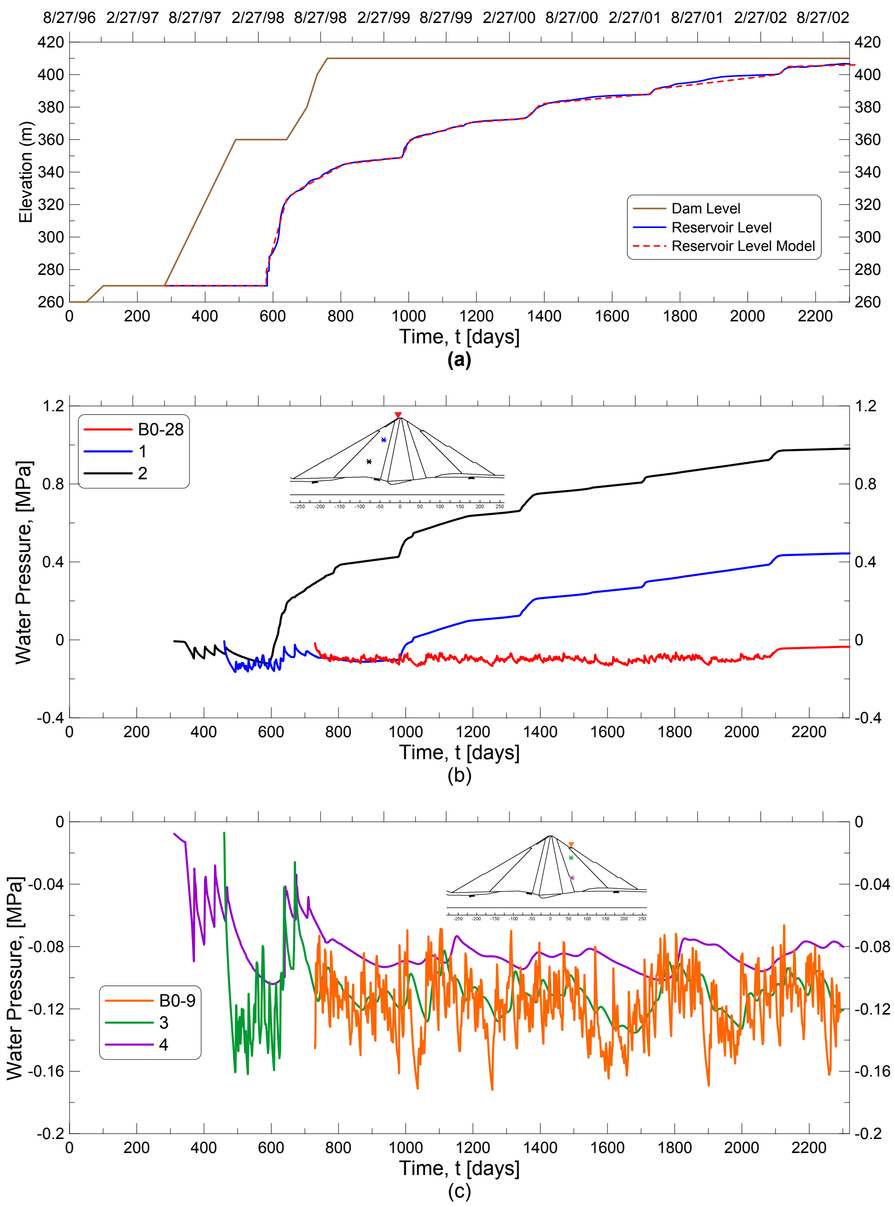

Figure 5.2: Evolution of: (a) Construction and impoundment sequence (b) Water pressure for upstream points B0-28, 1 and 2; (c) Water pressure for downstream points B0-9, 3 and 4: Base case.

Referring to Figure 5.2 (b), point 1 initially starts at a small water pressure and gradually decreases until day 650 due to drainage of the material. When a layer is constructed on top at day 650 it causes a reduction in suction (increase of water pressure) due to higher saturation levels in layer on top.

The initial water pressure at B0-28 begins to drop down at a slower rate compared to points 1 and 2 because of the less permeable materials underneath, restricting drainage. The pressure gradually increases when the reservoir begins impounding.

Points B0-9, 3 and 4 are on the downstream side and are entirely in the rockfill material. Figure 5.2 (c) shows that the rate of reduction of water pressure for points B0-9 and 3 is similar. Point 4 experiences lesser reduction in water pressure due to its proximity to the less permeable and more saturated transition zones.

It is evident that suctions in the downstream are higher because of the lower saturation levels. This points to lesser settlements prevailing in this zone based on the RM formulation and the observed mechanical behaviour of rockfill described in Appendix B.

The calculated changes in porosity for two comparable points in the upstream and downstream (Points 2 and 4) are presented on Figure 5.3 (a). The purpose of this figure is to present the differences between the changes of porosity for the upstream and downstream. Although the points are comparable, the loading and wetting history are rather different for the two points due to the dams complex layering. The decrease in porosity of the upstream shell due to raising of the reservoir level is reflected in the plot as well. Full flooding at the observed location occurs in Time [C], notated with a red line. This could be also seen on Figure 5.3 (b), where the suction at the upstream side decreases to 0 during Time [C]. The complex behaviour of the small increase of porosity during Time [C] is attributed to the simultaneous construction (increases in net stress) and impoundment (reduction in net stress). Construction finalizes at Time [C], but the impoundment continues all the way to end of Time [F]. This is reflected in the unloading on Figure 5.3 (a), notated with a dashed green line.

The upstream experiences a variation in suction and mean net stress due to the rainfall history. This could easily be seen on Figure 5.3 (b). This change of suction causes "miniature" collapses over time unlike the collapse seen for the upstream, where upon flooding porosity suddenly decreases.

After full saturation, mean net stresses become effective stresses and changes in the reservoir level are reflected in the changes of effective stress.

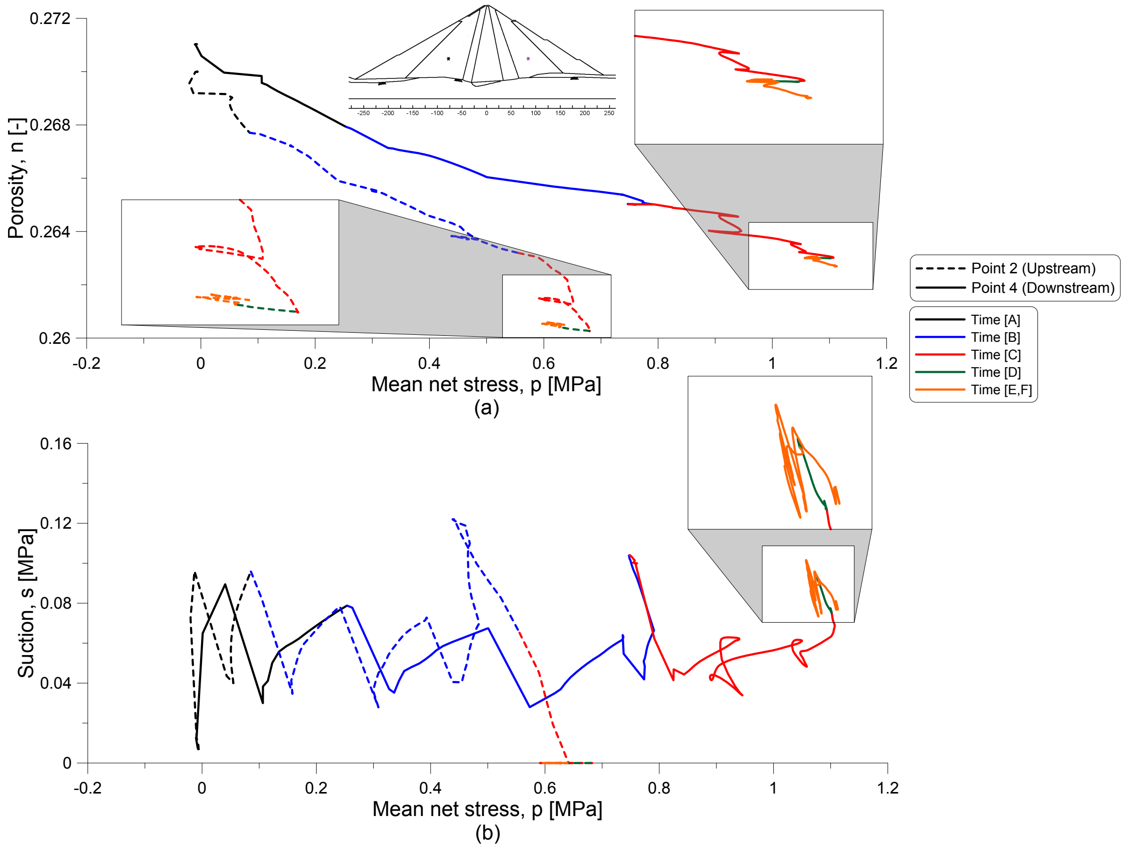

Figure 5.3: (a) Porosity-Mean net stress (b) Suction-Mean net stress for rockfill shells.

5.2.2 Comparison with instrument data

In addition to examining the pore water pressures in the rockfill zones, piezometer readings are available in the till core. Figure 5.4 exhibits the evolution of measured and calculated (model) water pressures compared at four different locations in the core. The till core is simulated with the Barcelona Basic Model, which incorporates the effects of suction. The pneumatic piezometer cells do not have the capability to measure the effect of suction. Therefore, before the reservoir level reaching the elevation of the cell, zero pore pressures are recorded.

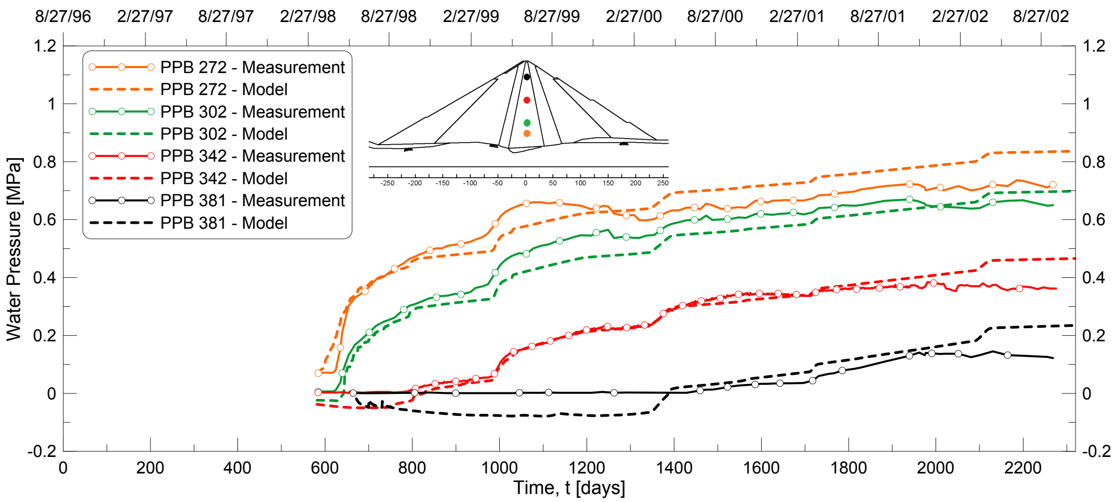

Figure 5.4: Pore water pressures in the till core of the dam: comparison of measured and calculated values for base case.

At the beginning of the simulation, when the reservoir has not reached the level of the instrument points, the simulated pore pressures become negative and keep decreasing due to the increase of suction in the material. This phenomenon is due to draining of water out of the material over time, causing the saturation level to drop and therefore increase the suction based on the water retention curve of the till core. Over time, when the water reaches the level the piezometer cells, it fully saturates the material and the prediction of the simulation matches the field measurements to a good extent. This provides confidence in the method of simulating reservoir impoundment and the selection of appropriate hydraulic parameters for the till core.

5.3 Degree of saturation

5.3.1 General results

Another interesting aspect of the dam behaviour is the degree of saturation in the zones. It is directly tied to the pore water pressures through individual water retention curves for each material zone. Examining the degree of saturation provides information of the proper (or wrong) simulation of impoundment stages of the dam.

Figure 5.5 conveys the evolution of the degree of saturation for points in the upstream and downstream rockfill shells. The "spikes" observed on the figures are attributed to the construction of a new layer with an initial degree of saturation of around 30%, as the prescribed initial condition dictates. At day 760, the construction of layers is completed and thus the water begins to drain from the rockfill. This is due to governing equations dictating flow equilibrium in the system and higher permeability of the material.

A better visualization of the impoundment stages can be seen with contour plots. The contour plots are shown at four different stages between time [A] to [F]. The dark red colour represents fully saturated material and dark blue, dry material. The levels of saturation for each of the stages displays that the impoundment is simulated according to the sequence shown on Figure 5.5 (a). As expected, the downstream rockfill material has a low level of saturation, in the range of $3-15\%$

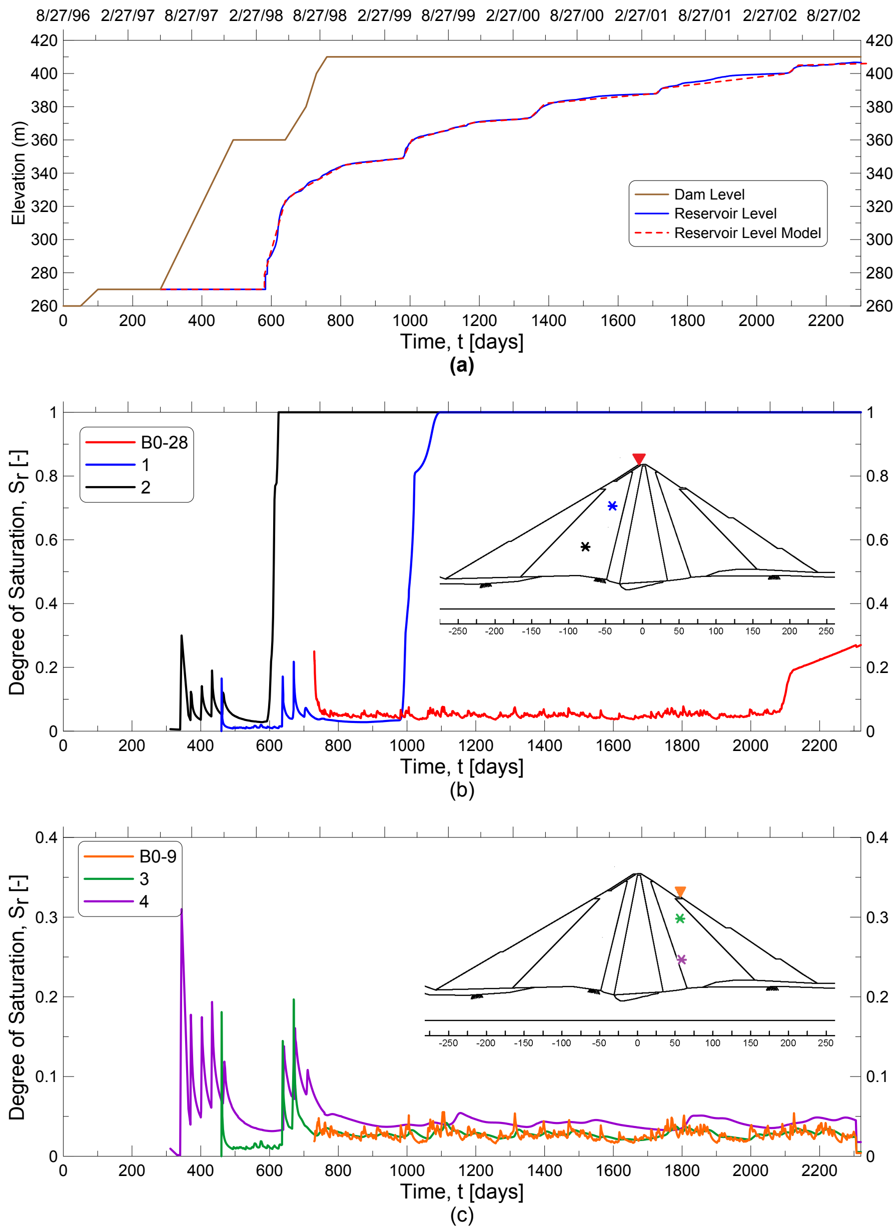

Figure 5.5: (a) Construction and impoundment sequence. Evolution of degree of saturation for (b) upstream points A, 1 and 2; (c) downstream points C, 3 and 4: Base case.

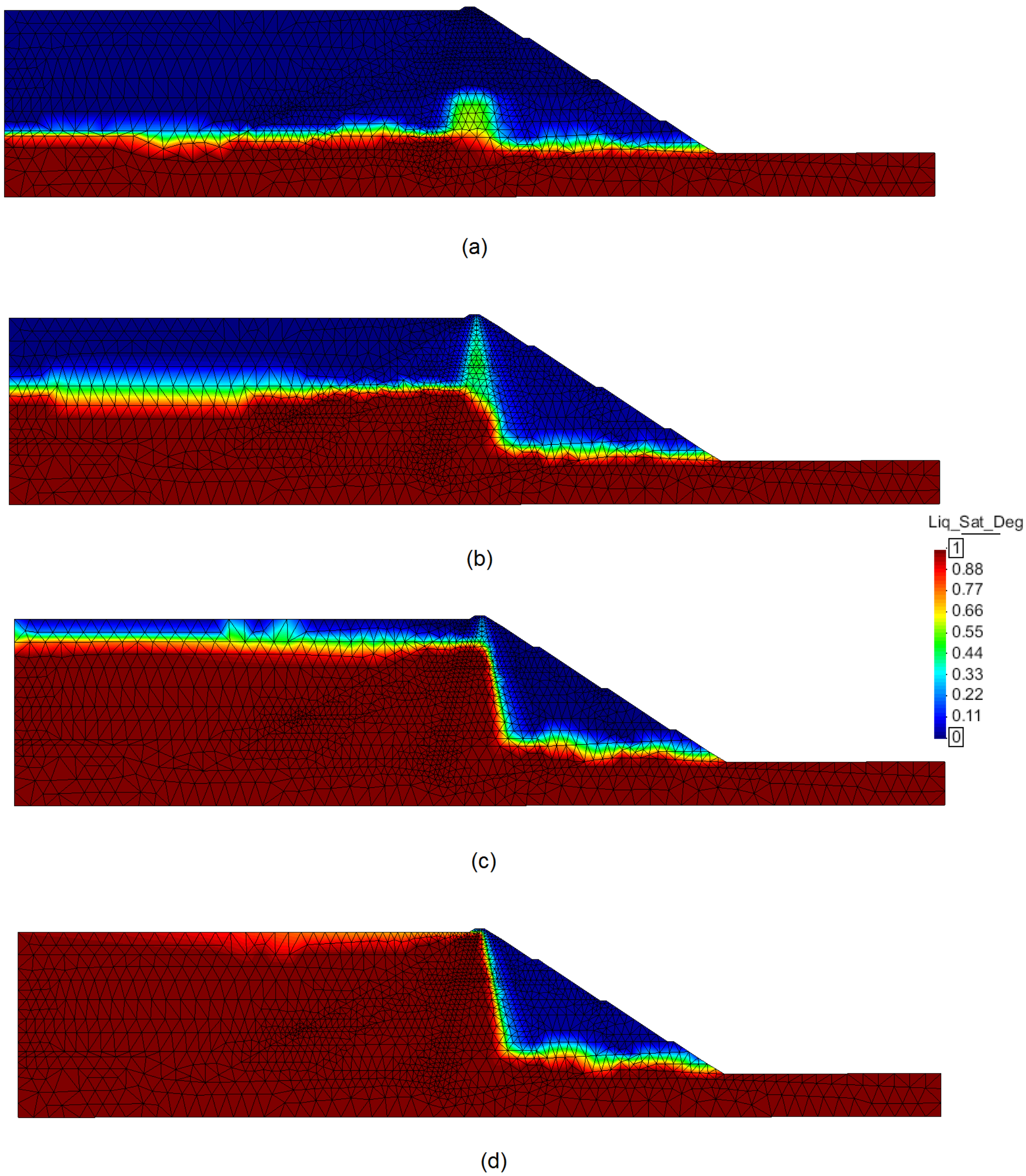

Figure 5.6: Contour plots for degree saturation at (a) end of time [A] (b) end of time [C] (c) end of time [E] (d) end of time [F].

5.4 Vertical total stress

5.4.1 General results

The calculated stress transfer phenomenon between the shells, transition and core is observed in Figure 5.7, where vertical stresses along a horizontal line, 60 m above the bottom of the till core (elevation 325 m), are represented. The stress distribution is explored at four stages between Time [A] and Time [F].

Vertical stresses between the inner shell, transition and the core reflect the collapse calculated for the rockfill. Moving from Time [B] to Time [E], the initial symmetrical distribution of stresses becomes non-symmetrical as a result of the impoundment, which induces rockfill collapse.

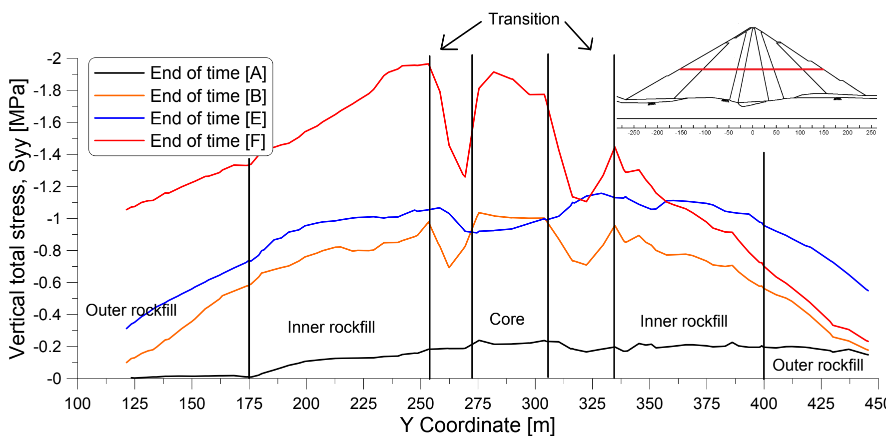

Figure 5.7: Vertical stresses during construction and impoundment on a horizontal plane at elevation 60 m above the bottom boundary of till core for Times [A] to [F].

Contour plots are produced for the vertical total stress S_{yy} for the same four dates as the contour plots for the degree of saturation. They can be seen on Figure 5.8, where dark blue colour represents stresses of 3.46 MPa and dark red stresses of 0 MPa The Figures show a gradual progression of the stresses as the dam is constructed and impounded. Figure 5.8 (b) represents end of construction and impoundment of half of the reservoir. As the reservoir is fully impounded, it can be seen that the stress in the upstream shell has increased due to the water weight and some stress redistribution has taken place towards the downstream. Shifting of stresses are better seen when comparing simulation results with measurements from pressure cells.

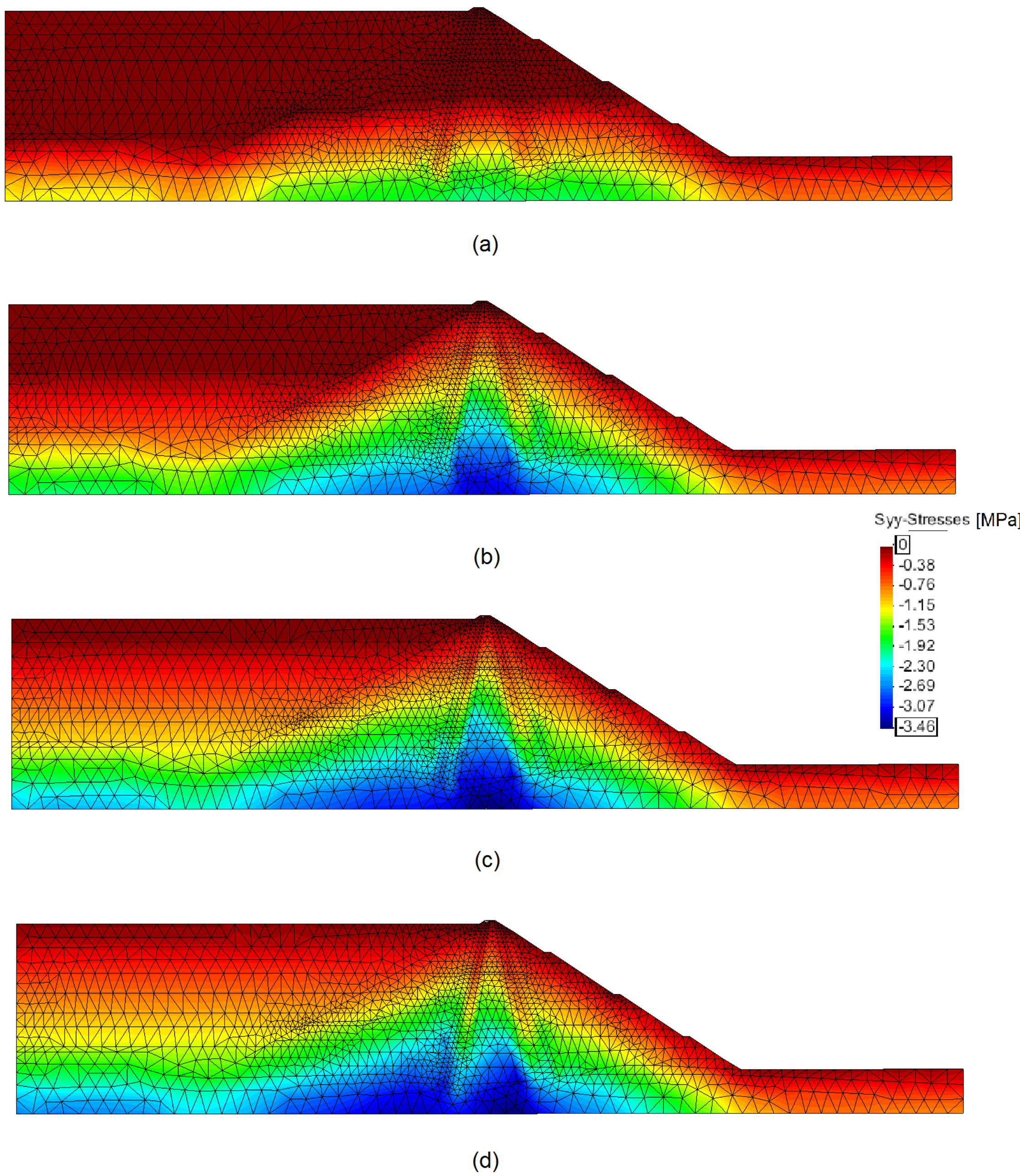

Figure 5.8: Contour plots for vertical total stress in MPa at (a) end of time [A] (b) end of time [C] (c) end of time [E] (d) end of time [F].

5.4.2 Comparison with instrument data

Vertical total pressures are compared to measured values in Figure 5.9. The simulation results are agreeable with the measured field value for point CPB 251. Field observations show a reduction of the total stress over time, due to horizontal displacement and shifting of the material towards the downstream. The observation from the pressure cell at point CPB 255 shows an increase in stress, which confirms shifting of the material towards the downstream. The model seems to capture this shifting behaviour and produces an agreeable qualitative result, but seems to under-predict the stress at point CPB 255. The soil column above point CPB 255 is predominantly transition material. The under-prediction of the stress could come from the choice of inaccurate material properties for the transition zones, such as porosity, G_s, intrinsic permeability or even the initial degree of saturation.

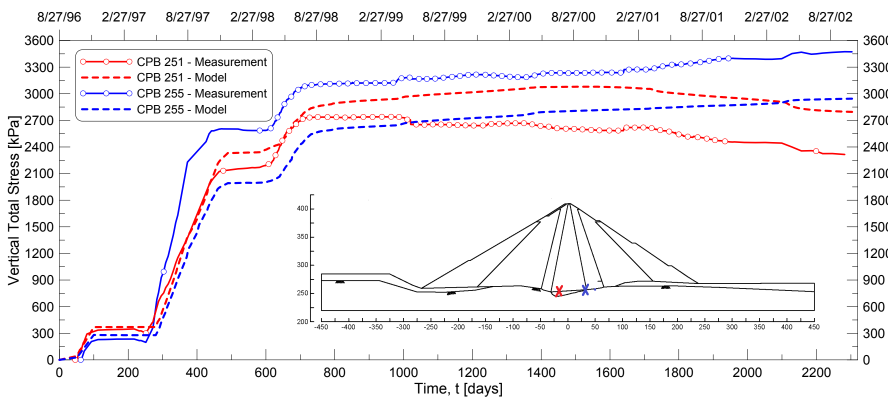

Figure 5.9: Vertical stress in MPa at the bottom of the till core for points CPB 251 and CPB 255: comparison of measured and calculated values for base case.

5.5 Vertical displacements

5.5.1 General results

The vertical displacements (settlements) are one of the key criterion for the safety operation of a dam. Figure 5.10 shows the contour plots of settlement for different stages of the dam construction and impoundment. In Figures 5.10 (a) and (b), settlements are generally uniform due to the symmetrical geometry of the dam.

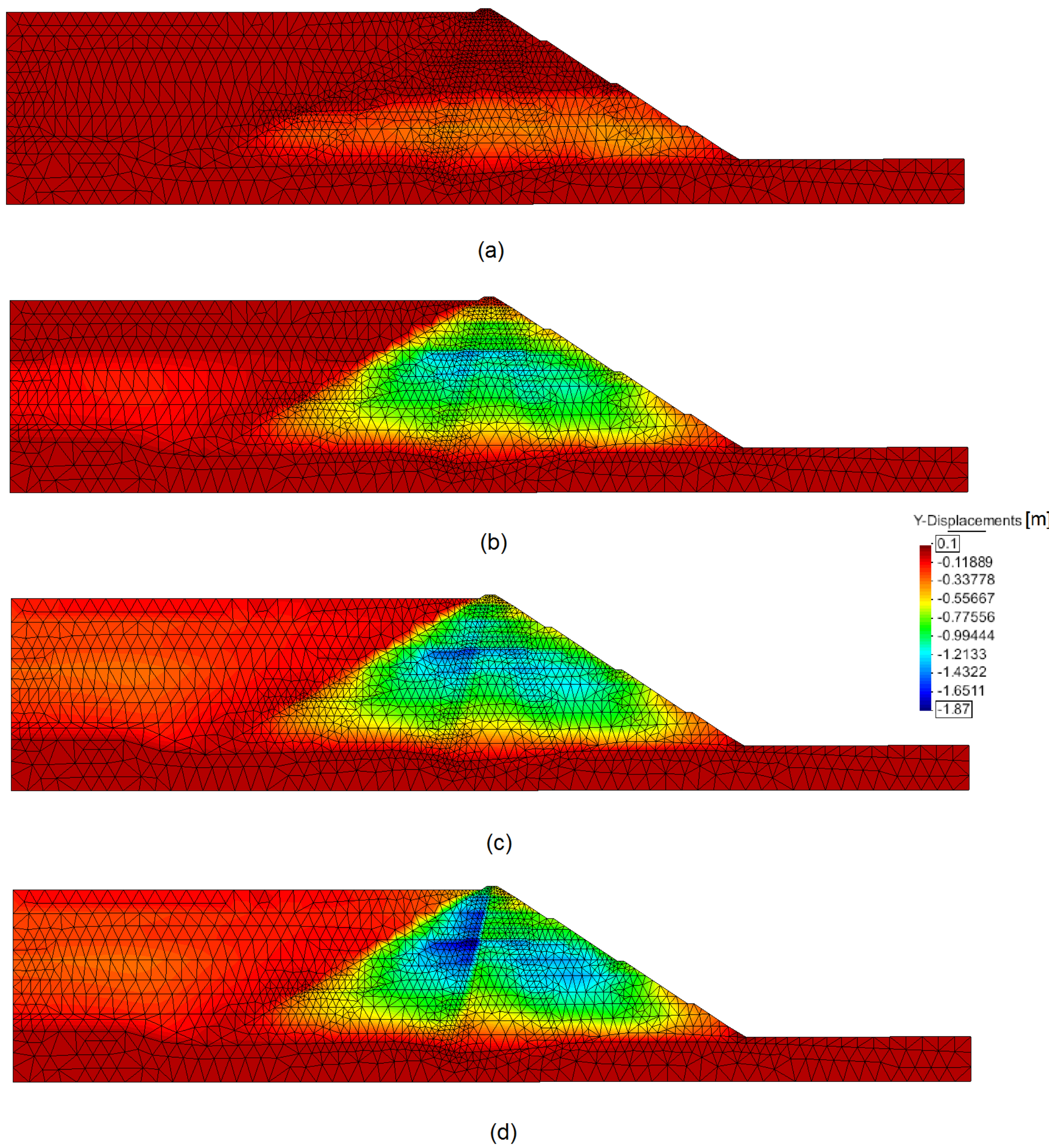

Figure 5.10: Contour plots for vertical displacements (settlement) at (a) end of time [A] (b) end of time [C] (c) end of time [E] (d) end of time [F].

Once impoundment commences, settlements begin to generate more in the upstream. In Figure 5.10 (c), the reservoir is halfway filled and displacements are generated more in the upstream shelf.

5.10 (d) represents full impoundment of the dam and exhibits higher amount of settlements in the upstream shelf compared to the downstream one. Due to the highly dense and compacted core, much less settlements take place.

5.5.2 Comparison with instrument data

Inclinometers

The evolution of calculated vertical displacements with depth at inclinometers INB1 and INB5 are shown during construction and initial impoundment on Figure 5.11 and after construction and final impoundment on Figure 5.12.

The agreement is good for the downstream inclinometer INB5 during the construction period. The reservoir impoundment does not affect the downstream, therefore, the particle breakage mechanism does not play a significant role due to the low level of saturation, making the particle re-arrangement mechanism more dominant.

The same inclinometer, INB5, after the construction of the dam, has a very good agreement with field measurements as observed on Figure 5.12. Calculated displacements are underestimated for inclinometer INB1 during the construction of the dam as seen on Figure 5.11. The cause is lower compressibility of the saturated material than in reality. The under-prediction of the compressibility stems from the attempt to simulate rockfill with particle sizes of up to 1.8 m using laboratory data of scaled down rockfill with particle sizes of up to 0.06 m. This discrepancy between laboratory and field compressibility values is due to the effect of particle size. In Chapter 6, the effect of particle size on the particle breakage mechanism is examined thoroughly.

Long term settlements in the upstream shell (INB1) are shown on Figure 5.12. The settlement trend is approximated to an extent. Settlements at elevations 260 to 320 m are low because collapse in those zones already occurred during initial construction and impoundment. Post-construction settlements are measured with reference date 09/10/1998, when reservoir level has reached 320 m. The settlements at elevations greater than 320 m, are prone to gradually increase due to the slow impoundment of the reservoir until finally reaching 400 m in the year 2003. It has to be noted that the post construction inclinometer measurements for INB1 could not be considered reliable, as mentioned in Chapter 2.

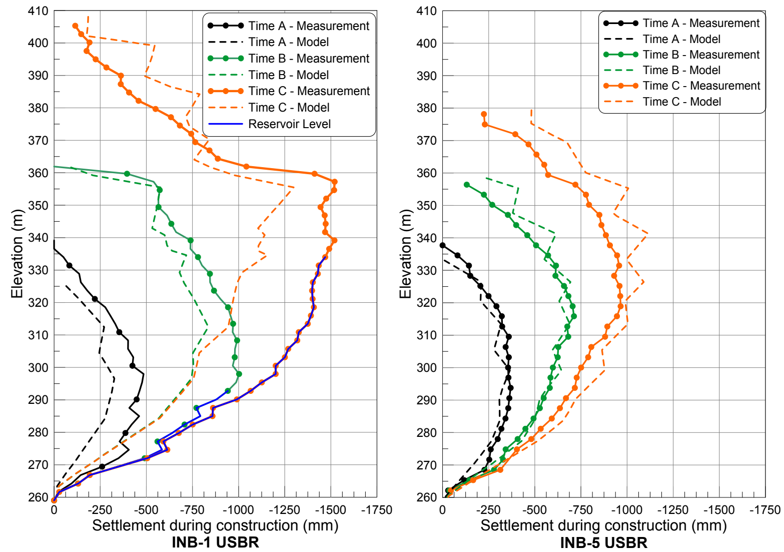

Figure 5.11: Calculated and measured vertical settlement for inclinometers INB1 and INB5 after construction for stages [A] to [D]: base case. Elevation 260 corresponds to bottom of the rockfill shell.

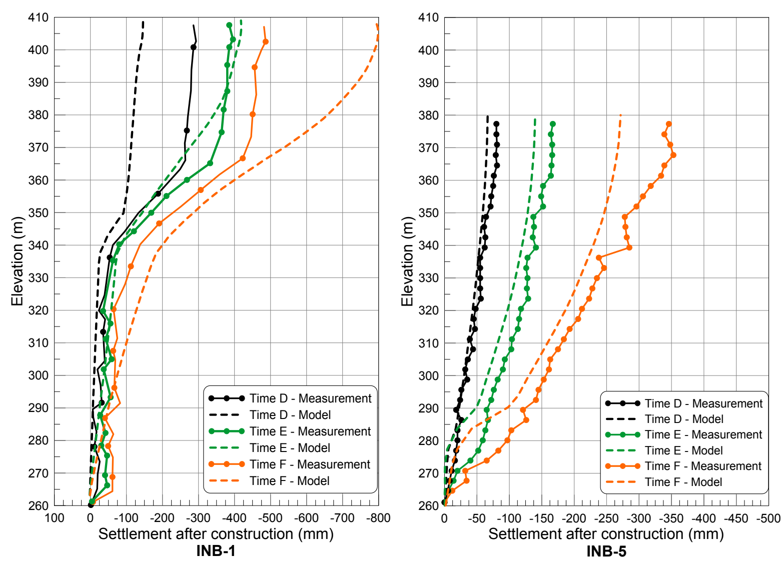

Figure 5.12: Calculated and measured vertical settlement for inclinometers INB1 and INB5 after construction for stages [E] to [G]: base case. Elevation 260 corresponds to bottom of the rockfill shell.

Observation terminal

Vertical displacements are measured at the surface crest and downstream face during the whole process of construction and impoundment at chosen locations. Simulation results are compared with the measurements as seen on Figure 5.13. Point B0-05 has very good approximation of the field measurement. Points B0-28 and B0-9 have a good qualitative approximation of the settlement trend, but are inaccurate by $20-40\%$. This under-prediction is the result of a few factors. The first one is, as discussed for inclinometer INB1, the particle size effect. This effect is thoroughly discussed in Chapter 6. There are other physical causes for the discrepancy between measurements and simulations such as possible unreliable field measurements. Generally, there could be very shallow surface displacements, which are not representative of the actual deformations in the area. This could cause the observation terminals to show higher displacements, when in reality they are smaller. Another factor could be a reported shear crack on the crest of the dam. The crack presence could lead to higher measured vertical and horizontal displacements.

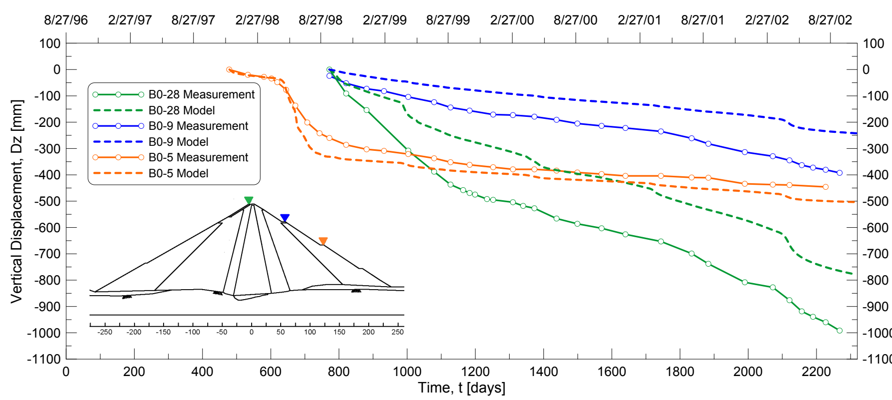

Figure 5.13: Vertical displacements for points B0-28, B0-9 and B0-5 along the dam crest: comparison of measured and calculated values for base case.

5.6 Horizontal displacements

5.6.1 General results

Contour plots of the horizontal displacements are shown on Figure 5.14. They help to visualize the forming shear planes within the dam and progression of material movement. The pre-impoundment spatial distribution of horizontal displacements is seen on Figures 5.14 (a) and (b).

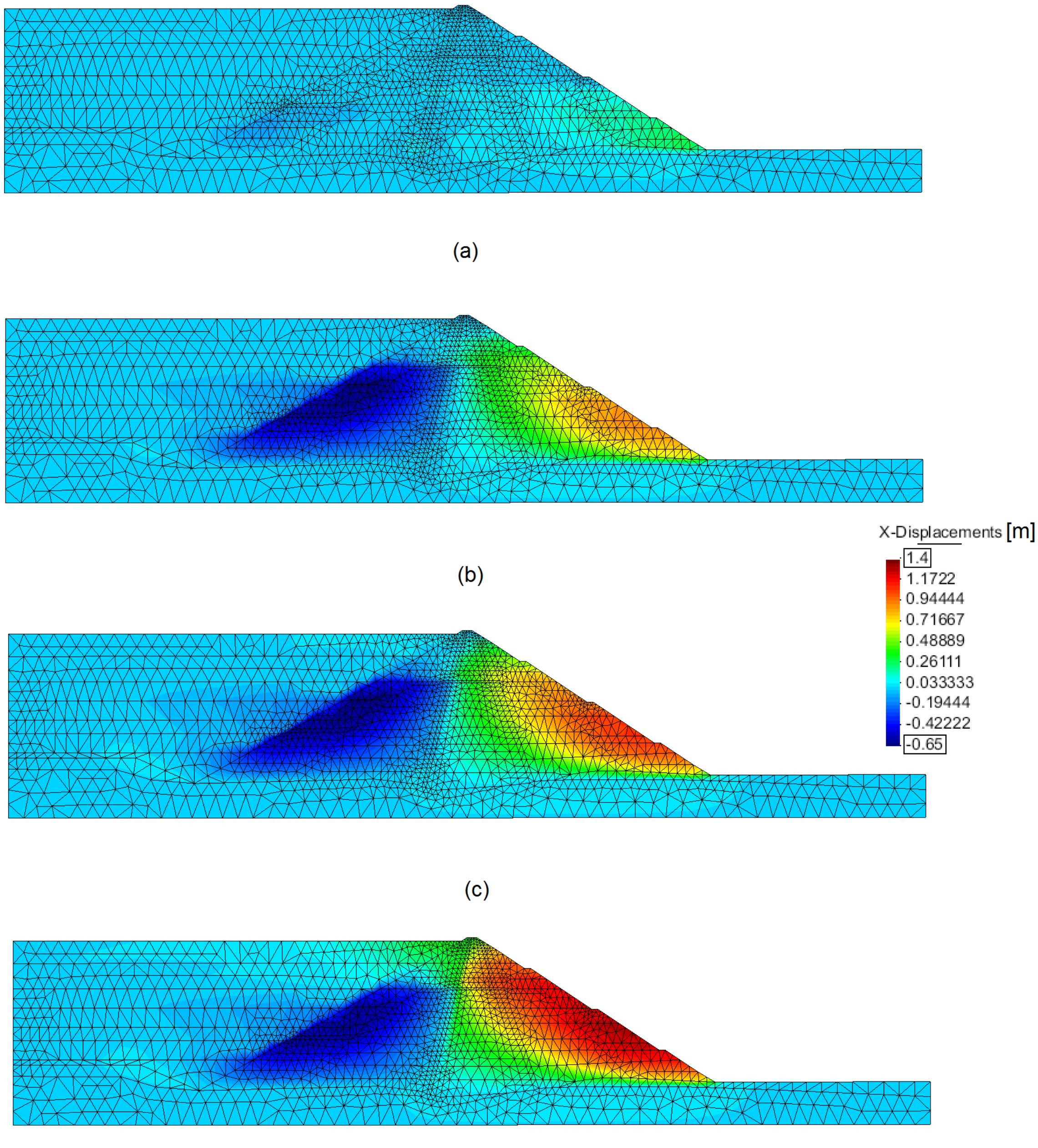

Figure 5.14: Contour plots for horizontal displacements in metres at (a) end of time [A] (b) end of time [C] (c) end of time [E] (d) end of time [F].

Once impoundment commences, downstream horizontal displacement rates increase towards the upstream side. Downstream horizontal displacements reach to 1.4 m and the upstream only to 0.65 m.

5.6.2 Comparison with instrument data

The complete evolution of horizontal displacements at observation points B0-28, B0-9 and B0-5 are shown on Figure 5.15. The horizontal displacements at point B0-28 are underestimated by a factor of two but follow the general trend. Point B0-9's calculated horizontal displacements agree with the observation. The horizontal displacements for point B0-5 are significantly overestimated, but follow the trend of the measured displacement curve to a good extent. The over-prediction of displacements occurs during the final stage of the construction process, ending at day 760. A similar phenomenon is observed in the analysis of Beliche dam by Alonso et al. (2005), where horizontal displacements from the mid section of the dam are over-predicted. This could probably be due to the model formulation and generation of excessive deviatoric stresses in that zone.

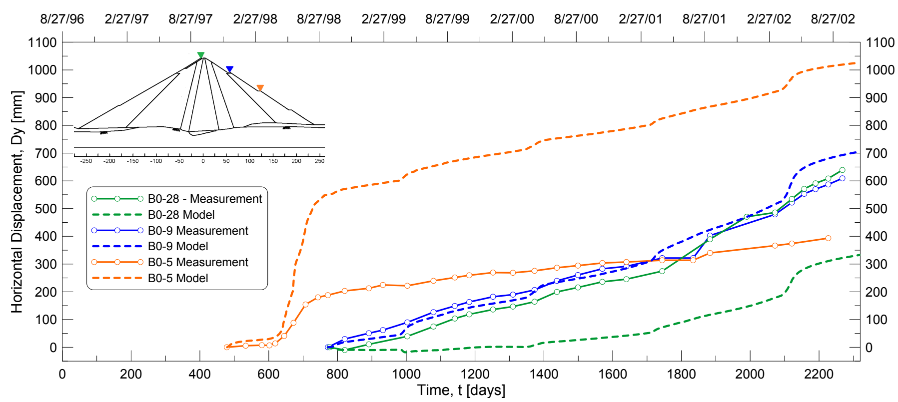

Figure 5.15: Horizontal displacements for points B0-28, B0-9 and B0-5 along the dam crest: comparison of measured and calculated values for base case.

Some additional cases such as modifying rockfill compressibility, to account for scale effects, and exploring rockfill permeability variation are examined in Chapter 6.

5.7 Summary

The base case is defined based on the basis of material parameters estimated from laboratory tests and literature. Due to the complexity of the constitutive models used, the provided laboratory data has limited capabilities of providing all of the necessary material parameters. The extensive literature available provided a solid basis for assuming some of those parameters. Generally, the simulation outcome is highly successful. The simulation results matched fairly well field measurements for few different responses.

The piezometer measurements in the core matched qualitatively and quantitatively the simulation results with an error of less than 10%. Therefore, it gives confidence in the impoundment stages simulated and the chosen hydraulic parameters for the zones.

Simulation results for total stress at the bottom of the core approximate the general trend of pressure cell measurements. Some interesting stress transfer phenomena is captured by the simulation due to movement of material towards the downstream and the impoundment. The same phenomena is observed by the pressure cells. The discrepancy with the final measurements could be attributed to poor approximation of the transition zone material parameters.

Simulations results for settlements during construction and initial impoundment for the upstream and downstream shells, approximate the behaviour to a good extent as well. The results match qualitatively the inclinometer measurements, which confirms the correct implementation of the construction stages. The results also approximate well the response in a qualitative manner with an error of less than 20%.

There are discrepancies between the long term displacement measurements and the simulation results. Generally, the trend is approximated well, but the final simulated settlements are less than the one observed in the field. For clarification purposes, it has to be noted that material parameters for the base were not adjusted to "match" instrument data.

On another subject, it has to be appreciated that, even though the constitutive models are fairly complex and capture the behaviour of rockfill, simulating a massive structure like a dam is a difficult task. Simplifying a large 3D structure and simulating it in 2D could lead to miss-representation of reality. Weather conditions, in particular rainfall, was simulated successfully but accounting for the hard winter conditions was not done. Other sources of error could include faulty instruments or miss-representation of the actual construction process.

Chapter 6

Complementary simulations

6.1 Introduction

The reference case, based on available laboratory results and literature, provides a satisfactory model response. However, discrepancies in measured upstream and downstream horizontal and vertical displacements remain.

Several reasons for those discrepancies are proposed in this chapter. The validity of scaled samples is a key issue. Compressibility is expected to increase with particle size, due to the size effects of crack propagation. Also, two laboratory samples are hardly representative of the whole in-situ material in such a large structure. This effect has proven to be quite significant and therefore a more substantial portion of this chapter focuses on exploring this phenomenon. An attempt is made to quantify the scaling effect.

Rockfill hydraulic properties are estimated based on literature, but the actual in-situ values are unknown. Properties like the water retention curve, initial saturation and permeability are unknown and are derived based on similar rockfill material from other dams. Exploring the effect of different water retention curves is not a part of this research due to the complexity of the problem. Instead, a parameter such as intrinsic permeability, is examined because it provides a more clearer perspective of its effect.

6.2 Sensitivity analysis on rockfill compressibility

The objective of this section is to address the effect of particle size on the compressibility parameters through a numerical simulation. First, based on previous research, the connection between particle size and the compressibility of rockfill and other potential factors needs to be established.

6.2.1 Effect of particle scale on rockfill compressibility

Tests show that the external stress capable of breaking particles, $(\sigma_{ext})_f$, depends on the particle size and can be defined as

$$(\sigma_{ext})_f \propto d^{-\alpha_{\text{scaling}}} \tag{6.1}$$

where d is the average particle size and α_{scaling} varies between 0.3 and 0.5 for the tested materials. For more information on the derivation, refer to Oldecop and Alonso (2013*a*). An explanation for the phenomenon is that more defects, cracks and micro-cracks in a bigger particle than a smaller one provides more stress concentration zones and thus weakens the particle. Therefore the bigger the particle, the more particle breakage occurs. Large oedometer tests are impractical and expensive and the maximum grain size that can be tested is 150-200 mm (Oldecop and Alonso, 2013*a*). Most dams have a maximum particle size of 0.5-1 m, which is impossible to test in a laboratory. Grain size distributions may be scaled down in an attempt to preserve the behaviour of the sample dimensions. However, the scale effects still have to be addressed in the numerical simulation.

Scaling up of λ_0^d is necessary because it governs the particle breakage mechanism, which, as discussed before, depends on the particle size. The parameter λ_i on the other hand, governs the particle re-arrangement mechanism, which is not reported to be dependent on the particle size.

6.2.2 Simulation results

To evaluate the effect of scaling regarding the rockfill material from Denis-Perron, simulation results with no scaling are examined and simulations results with scaling are explored as well.

Comparison of the simulation results to the settlement measurements at INB1 and INB5 has been done initially with using the $\lambda_0^d = 0.009$ directly calibrated based on the oedometer test data and no scaling applied. Three more simulations have been performed with $\lambda_0^d = 0.012;\ 0.015;\ 0.018$. The results of those simulation are presented for four different time intervals. The first two time intervals, [B] and [C], represent the response during construction and initial impoundment. The last two intervals, [E] and [F], represent the long term behaviour until the full impoundment of the dam.

For base case where $\lambda_0^d = 0.009$, results show under-prediction of the settlements recorded at INB1 in the zones where the rockfill has been exposed to the water action but good predictions are otherwise for evident both inclinometers. Judging by the results from Figures 6.1 and 6.2, the compressibility parameter λ_0^d, responsible for the wet behaviour of rockfill, has to be increased, or in other words scaled up from the one calibrated based on the oedometer test. This is supported also by the background discussed regarding the effect of particle breakage in the previous section.

Both inclinometers are predominantly within the inner shells of the dam. Therefore, the effect of the outer shell settlements cannot be captured by the inclinometers. Hence, the more representative value λ_0^d for the inner shell is estimated based on comparing the settlement from the numerical simulations and the data of INB1 and INB5.

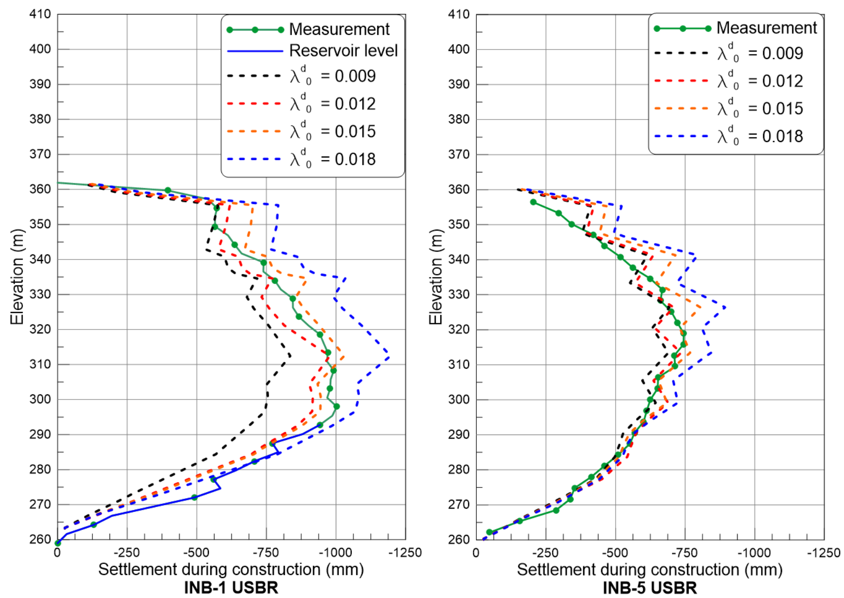

Figure 6.1: Calculated and measured vertical displacements for INB1 and INB5 at Time [B] for four differen values for λ_0^d.

Furthermore, the best match of the settlements is achieved with scaling the λ_0^d of the inner shell by a factor of 1.65 from the value of 0.009 obtained in the lab test, resulting in $\lambda_0^d = 0.015$. The higher value of $\lambda_0^d = 0.018$ over-predicts the settlements for end of time [B] for both INB1 and INB5 and also for end of time [C] for INB5. The scaling effect is less obvious in the post construction response of the dam. Figures 6.3 and 6.4 illustrate this and is evident that the difference in settlement between simulations with $\lambda_0^d = 0.012; 0.015$ and 0.018 is negligible. Generally, the results illustrate that the scaled λ_0^d provides an improved approximation of the field settlements with better agreement with the field data, hence a better capturing the compressibility of large wet particles.

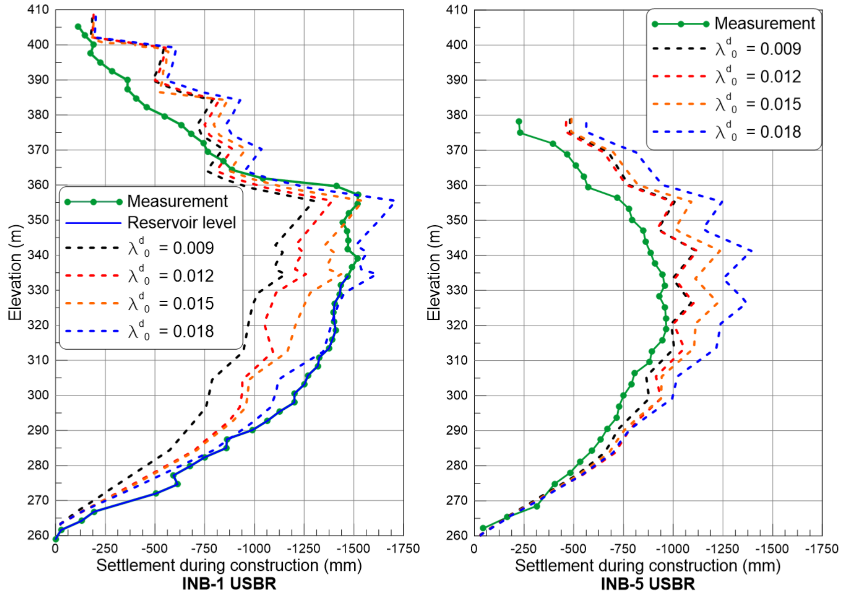

Figure 6.2: Calculated and measured vertical displacements for INB1 and INB5 at Time [C] for four differen values for λ_0^d.

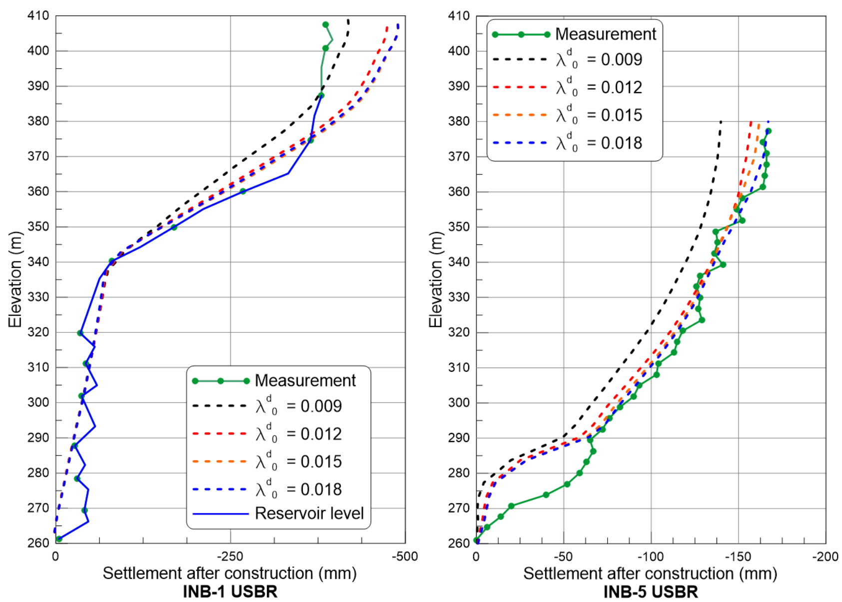

Figure 6.3: Calculated and measured vertical displacements for INB1 and INB5 at Time [E] for four differen values for λ_0^d.

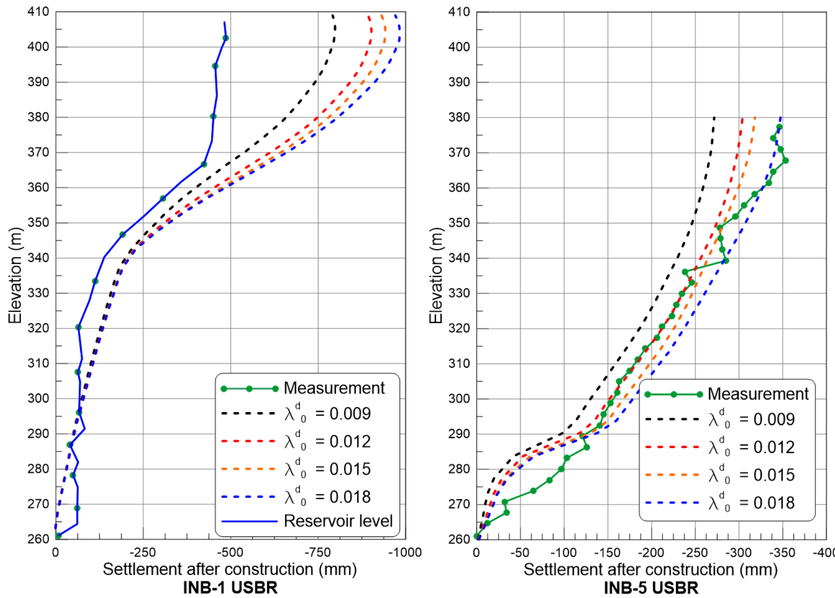

Figure 6.4: Calculated and measured vertical displacements for INB1 and INB5 at Time [F] for four differen values for λ_0^d.

6.2.3 Quantification of size effect

To asses and quantify the particle size effect, a scaling law has to be put in place. Assuming assemblies of uniform spherical particles and linear stress-strain relationship, a scaling law similar to Equation 6.1 is proposed by Oldecop and Alonso (2013*a*) for the delayed compressibility parameter

$$\lambda \propto d^{\alpha_{\text{scaling}}} \tag{6.2}$$

$$\lambda^d = \lambda_0^d \left(\frac{d}{d_0}\right)^{\alpha_{\text{scaling}}} \tag{6.3}$$

Equation 6.3 follows directly from Equation 6.2, where d is the maximum particle size of the prototype (field) material; d_0 is the maximum particle size of the model (laboratory) material; λ^d is the compressibility parameter of the prototype and λ_0^d is the compressibility parameter of the model. The exponent α_{scaling} is a function of the density of the aggregate and the type of rock and governs the severity of scaling. In the work of Oldecop and Alonso (2013*a*) a limestone material has been presented, which has α values varying between 0.33 and 0.5 for dense and loose aggregates respectively. Based on Equation 6.3, a plot on Figure 6.5 is presented to show the variation of λ^d with different α_{scaling} values, where $SF = d/d_0$ is a scaling factor, relating prototype dimensions to model dimensions.

Figure 6.6 shows the scaling law from Equation 6.3 applied to laboratory data. The laboratory data is related to the compressibility of two sets of samples, both with uniform particle sizes (40-30 mm, 30-20 mm; 25-20 mm; 20-10 mm) but different densities (one loose with $e = 0.947$ and one dense with $e = 0.5$). The scaling law of Equation 6.3 is used by (Oldecop and Alonso, 2013*a*) to scale down the λ^d of each sample to the corresponding λ_0^d of the sample with the smallest particle size.

In this process it has been founded that "taking d_0 as the minimum particle diameter tested, the size effect disappears, provided $\alpha_{\text{scaling}} = 0.5$ for the loose gravel and $\alpha_{\text{scaling}} = 0.33$ for the dense aggregate". The conclusion from this process is that "the α_{scaling} coefficient and, therefore, the intensity of scale effects depends on aggregate density".

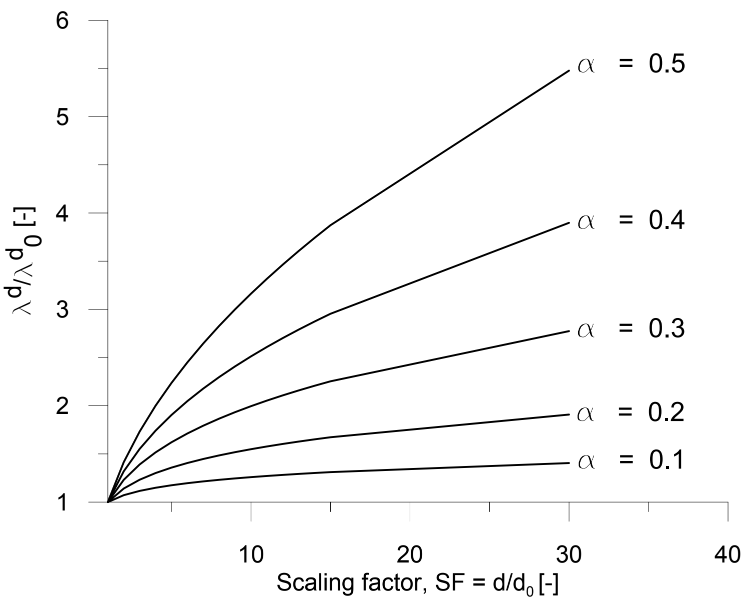

Figure 6.5: Variation of compressibility parameter λ^d for different α_{scaling} values.

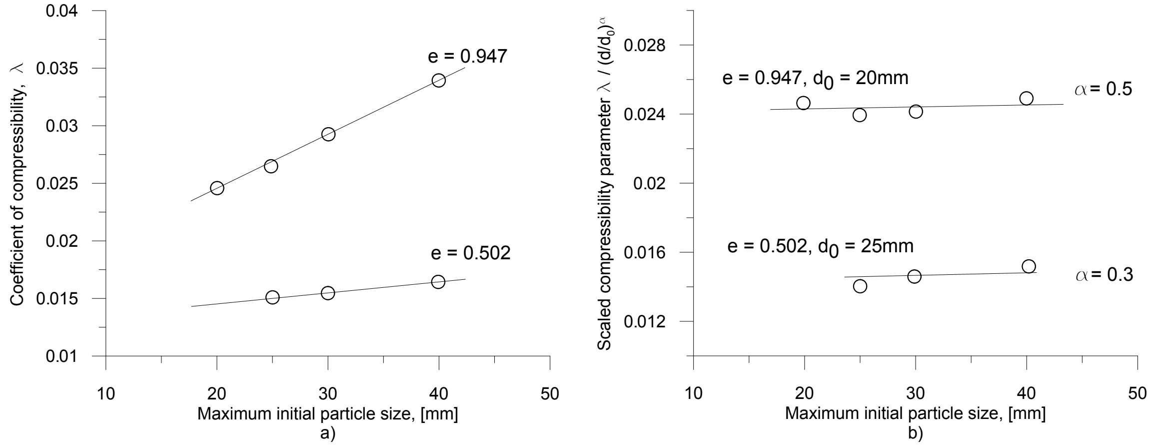

Figure 6.6: (a) Compressibility for samples with different maximum particle size at two different void ratios (b) Corrected compressibility of limestone material to account for scale effect. Modified from Oldecop and Alonso (2013*a*).

With reference to Figure 6.5, the parameter α for the rockfill material of the SM-3 dam can be calculated when the scaled λ_0^d (presented above) and field to laboratory SF are known for the material. For the inner and outer shells, the values of SF could be calculated based on their maximum particle sizes. Assuming the maximum particle size tested in the oedometer is about 60 mm the $SF = d/d_0$ can be calculated, where d_0 is the maximum particle size of the tested material and d is the $D_{\max}$ of the material in the field. For the inner shell, $SF = d/d_0 = 900/60 = 15$, and for the outer shell $SF = d/d_0 = 1800/60 = 30$. Based on this information and given the obtained factor of 1.65 for scaling of the compressibility parameter of the inner shell, parameter α_{scaling} is estimated as 0.19 for the inner shell.

Having no instrumentation within the upstream outer shell makes it impossible to explore this scaling effect for this material. Therefore, it is assumed the inner and outer shells behave similarly and share the same intensity of scaling parameter $\alpha_{\text{scaling}} = 0.19$. Earlier, it has been shown that the intensity of scaling parameter α depends on the density (void ratio) of the material. The present study suggests $\alpha_{\text{scaling}} = 0.19$ for the case of Denis-Perron dam with an approximate void ratio of 0.37 for the inner shell. This information in combination with the data from Figure 6.6 provides a relation between α_{scaling} and e_0 (initial void ratio).

To take it one step further, an α_{scaling} value can be determined for Beliche dam as well. In the paper of Alonso et al. (2005) the scaling factor $SF = D_{50,field}/D_{50,lab} = 100/18$ and the compressibility index has been increased with 50%. This translates to $1.5 = (100/18)^{\alpha_{\text{scaling}}}$ from Equation

6.3, which yields $\alpha_{\text{scaling,Beliche}} = 0.236$. The reported initial void ratio for the rockfill shells in Beliche dam is 0.538. A plot of the relation between α_{scaling} and void ratio can be seen on Figure 6.7

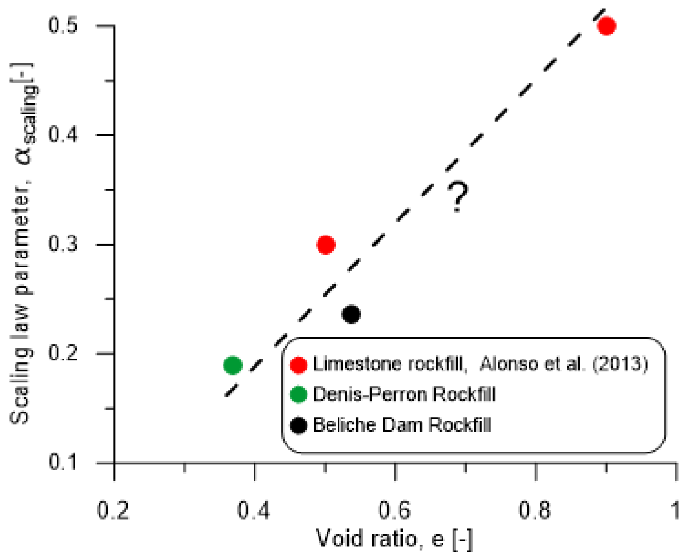

Figure 6.7: Variability of parameter α_{scaling} based on void ratio for laboratory data. Data from Oldecop and Alonso (2013*a*) and simulation results of Denis-Perron and Beliche Dam.

The data points provided on Figure 6.7 give an initial estimation of what the relation is between α_{scaling} and the void ratio. In order to establish a more reliable correlation, the plot has to be populated with more data points. This could be done by including more laboratory data, other large scale simulations or even results of a discrete element modelling of a large scale laboratory test.

The validity of determining the scaling effect needs to be addressed. Firstly, the compressibility parameter that is affected by scaling has to be established. As discussed, this parameter is the one responsible for the particle breakage phenomenon and dictates the maximum compressibility of the particle at full saturation. Secondly, in order for the scaling methodology to be valid, the effect of this parameter has to be isolated. The parameter is generally influenced by the level of saturation, the hydraulic properties of the material and the constitutive parameter of RM, α_s and β. At full saturation, the hydraulic properties of rockfill and the constitutive parameter become irrelevant, because λ_0^d reaches its maximum value. Therefore, comparison of the result between the simulations with applied parameter scaling and the field measurements is apparent for the fully saturated areas, which are in INB1. The results for INB5 are presented for consistency purposes and even though the effect of particle size is harder to isolate for the downstream zone, having accurate approximation of the settlements brings a level of confidence to the simulation approach.

6.3 Sensitivity analysis on rockfill permeability

Another reason for discrepancies that could be omitted on first sight, is the effect of the hydraulic parameters in rockfill. In this section, the permeability is discussed in particular. The value of the permeability for the rockfill is estimated based on available literature and deserves attention. Other hydraulic properties, like the water retention curve and the change of permeability with saturation, affect the response in a unclear manner that would be difficult to quantify.

A change in the rockfill permeability implies a change in the suction field. Lower water potential gradients are caused by increasing the rockfill permeability. This results in a more limited reduction of initial suction. Therefore, less collapse in the rockfill should be expected.

6.3.1 Simulation results

Two simulations are performed to examine the permeability effect of rockfill by increasing and decreasing the value from the original one of $k_{\text{rockfill}} = 1 \times 10^{-10}$ m^2. The first one has a tenfold reduction of rockfill permeability, $k_{\text{rockfill}} = 1 \times 10^{-11}$ m^2. The second, has a tenfold increase of permeability - $k_{\text{rockfill}} = 1 \times 10^{-9}$ m^2.

Comparison of the water pressure field and the displacements to the Base Case simulation and field measurements (if available), are discussed in this section.

6.3.2 Discussion

The water pressure within the rockfill is affected by the permeability of the material. Figures 6.8 (a) and (b) exhibit this behaviour - lower permeability increases water pressure and higher permeability reduces it. This results in lower suction for the lower permeability and higher suction values for the higher permeability cases.

Displacements are generally consistent with the expectation. Figures 6.9 suggest that lower permeability case yields higher settlements and the higher permeability one yields lower settlements. However, the effect on the horizontal displacements are less clear as can be seen on Figure 6.10. In locations B0-28 and B0-9, the higher permeability case yields more accumulated horizontal displacements than the lower permeability case.

Chapter 7 presents a summary of the thesis findings and a direction for future research in the field of rockfill mechanics.

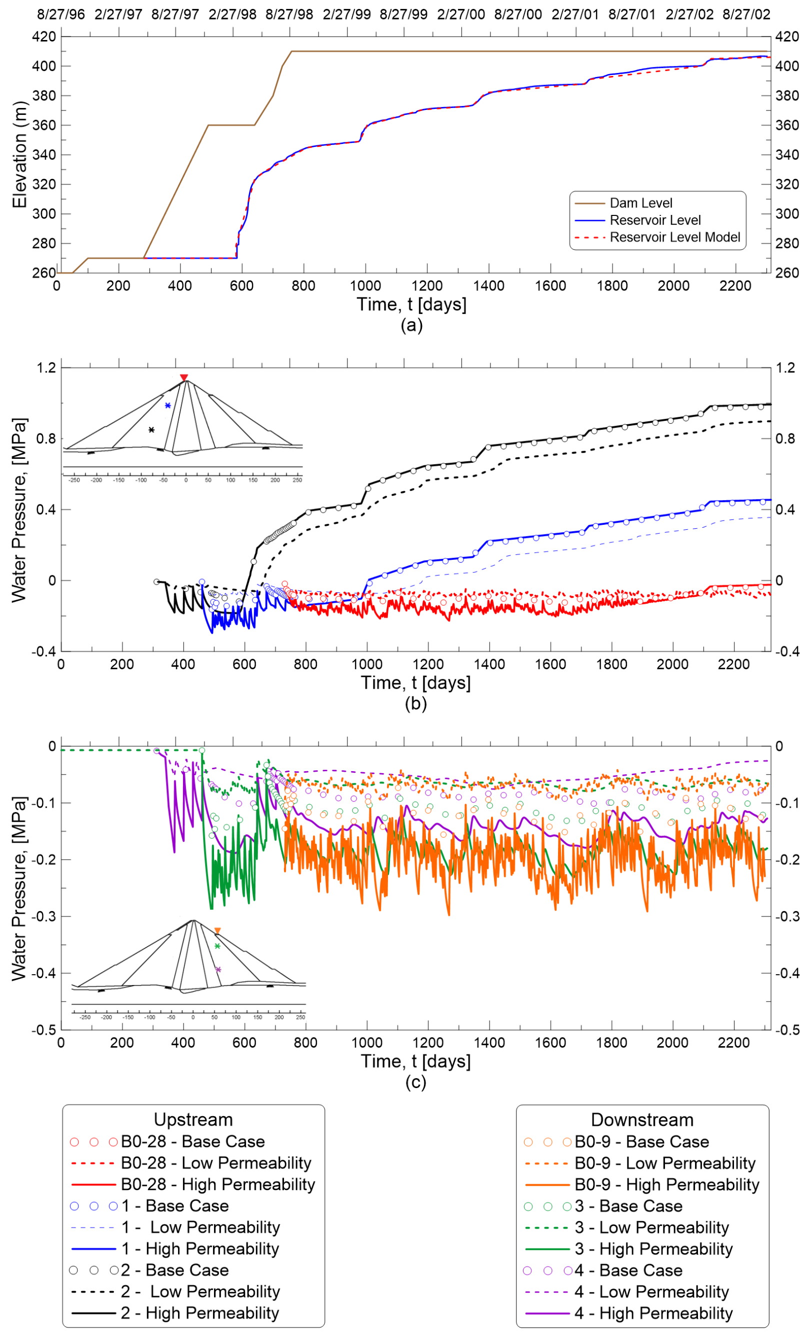

Figure 6.8: (a) Construction sequence (b) Water pressure for upstream points (c) Water pressure for downstream points.

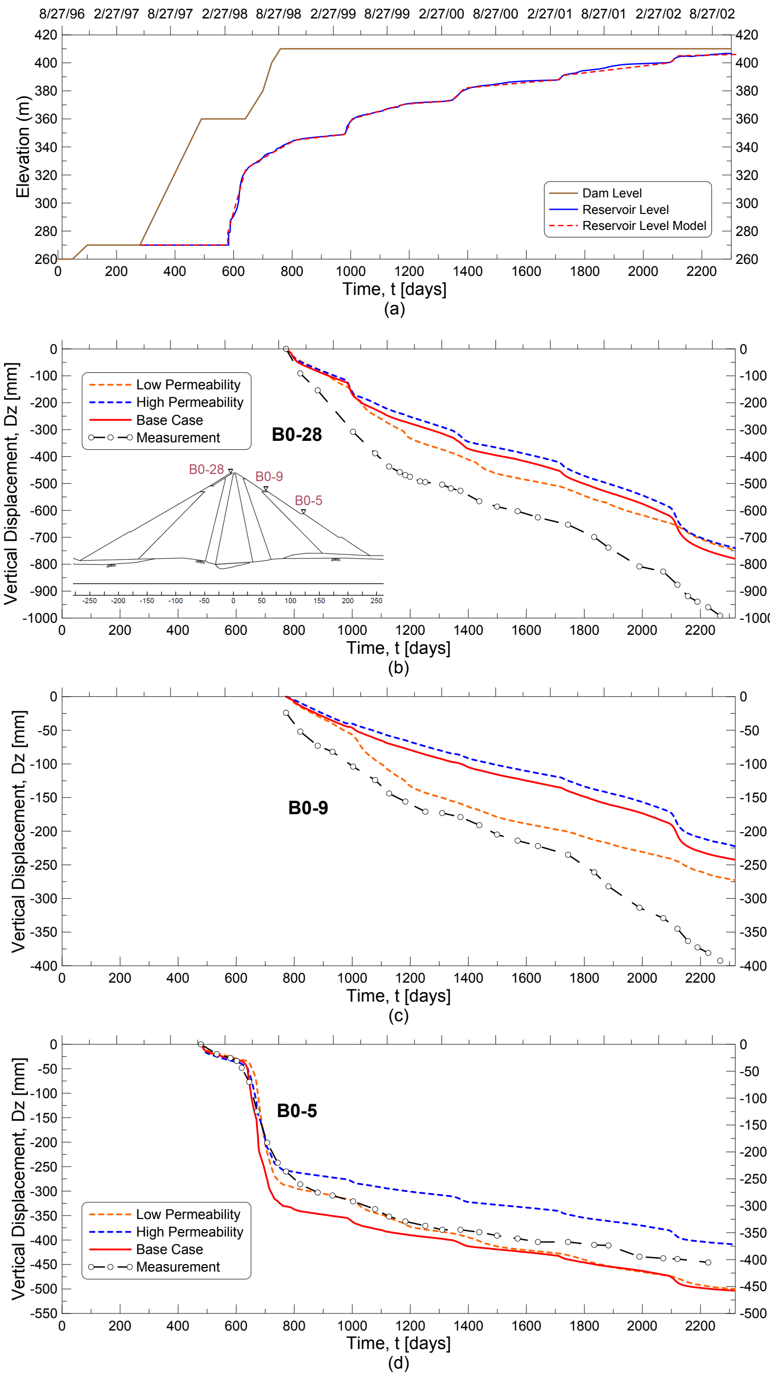

Figure 6.9: Vertical displacements for markers B0-28, B0-9 and B0-5 for the Base case, Low Permeability and High permeability cases.

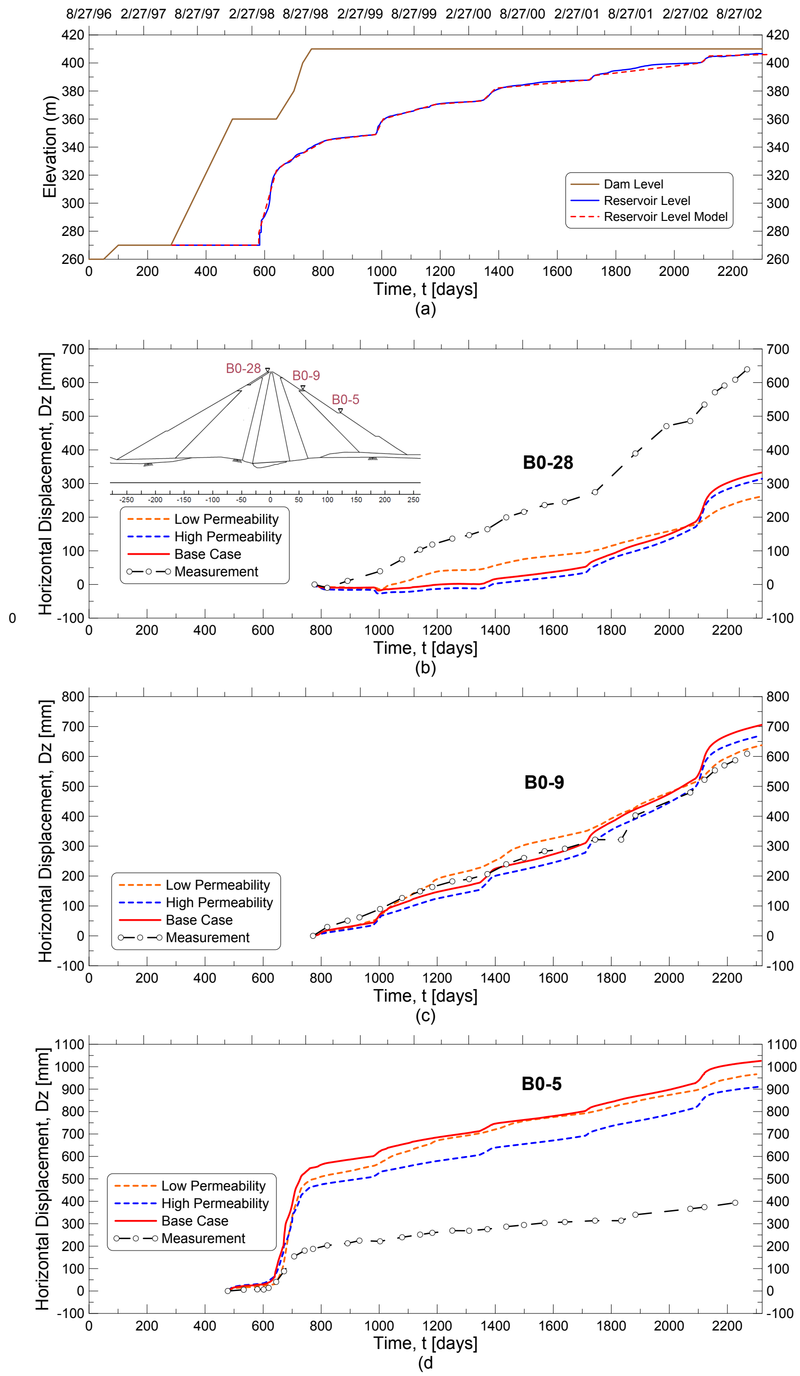

Figure 6.10: Horizontal displacements for markers B0-28, B0-9 and B0-5 for the Base case, Low Permeability and High permeability cases.

Chapter 7

Summary and future research

7.1 Summary of research

The response of rockfill dams presents a lot of challenges due to the uncertainties associated with rockfill behaviour. A fundamental variable governing rockfill behaviour is the effect of suction caused by the water action within the rockfill cracks. Some methodologies are already available that incorporate the role of suction, but are not based on physical phenomena and cannot take into account environmental factors, such as precipitation and/or evaporation. The thesis explored a modelling technique that is based on fundamentals of fracture mechanics, which is achieved through an implemented set of constitutive models in a fully coupled three phase finite element platform called Code_Bright (2015). The constitutive models used are the Barcelona Basic Model and the Rockfill Model, which captures the unsaturated behaviour of soils and rockfill respectively.

The research focuses on verification and validation of this particular modelling technique through an application of the RM in a numerical simulation of the well instrumented Denis-Perron rockfill dam. Denis-Perron dam is a zoned earth dam with compacted glacial till core and rockfill shoulders. Instrumentation data for a period of 6 years during construction, impoundment and operation was provided by Hydro-Québec.

Prior to modelling of Denis-Perron, a validation stage was carried out through simulating Beliche dam, which has been previously analysed by Alonso et al. (2005). The numerical model of Denis-Perron captures the construction stages, impoundment and the rainfall history recorded on site. Limited laboratory data was used to characterize the materials and calibrate constitutive model parameters. Ideally, the constitutive models require suction controlled tests to determine material parameters. In the case of Denis-Perron, the glacial till core's parameter calibration is carried out based on a suction controlled oedometer tests from a very similar material described in Watabe et al. (2000). For the rockfill shoulders, two oedometer tests under flooded and dry conditions are used for calibration. The oedometer test data was not sufficient to determine all necessary parameters, including the hydraulic ones. Therefore, some of them were estimated based on available literature.

Despite the limitations posed by the methodology of determining model parameters and lack of laboratory data, the general dam response has proven to be quite satisfactory. The accuracy of the results for settlements, horizontal displacements, stresses and pore pressures is within an acceptable range, considering all the uncertainties surrounding an analysis of such a large structure.

One of the contributions of the author is the successful simulation of the construction, impoundment and rainfall stages of the Denis-Perron dam. The current work can be used as a comprehensive guide to modelling future rockfill structures. This includes the creation of the numerical model, calibration of material parameters using laboratory data and an in depth analysis of the results. Another contribution of the author is the attempt to quantify the effect of particle size. It has been shown in the past that the compressibility of coarse grained material in laboratory experiments is reduced due to the smaller particle sizes tested. To account for this effect, the compressibility has been corrected through a back analysis of field measurements by using the numerical simulation. The results show a relation between the amount of compressibility increase and the void ratio of the sample. Finally, the effect of rockfill permeability on the dam settlements is explored as well.

7.2 Recommendations for future research

The field measurement data for Denis-Perron is only available for the period between 1997 and 2003. This does not allow assessing the performance of the numerical model regarding long term deformations. Gaining access to records between 2003 and 2017 would give valuable information and means compare long term simulation results to the field measurements.

Another direction for future research is studying and quantifying the effect of particle size on rockfill compressibility, using the approach adopted in this thesis. Modeling rockfill structures with available records of instrument measurements and laboratory data, could help establish even further the relation between particle size and the void ratio of the material. The scale effect could also be examined through simulations of oedometer and triaxial tests, using the Discrete Element Method (DEM). Unlike large scale testing apparatus, DEM is not limited by the size of the particle tested, even thought the level of complexity revolving around the model creation is very high.

Finally, large scale oedometer and triaxial tests with existing or newly constructed laboratory equipment could be performed, to continue the research on the different types of rockfill. Although rockfill's collapse is governed by a crack propagation mechanism, it is highly dependent on the type of minerals and structure of the rockfill. Therefore, it is necessary for future researchers to carry on a comprehensive set of tests to characterize the different rockfill materials.

Bibliography

Alonso, E. E., Gens, A. and Josa, A. (1990), 'A constitutive model for partially saturated soils', *Géotechnique* **40**(3), 405–430.

Alonso, E. E., Olivella, S. and Pinyol, N. M. (2005), 'A review of beliche dam', *Géotechnique* **55**(4), 267–285.

Alonso, E. E., Olivella, S., Pinyol, N. M., Soriano, A. and Esteban, F. (2012), 'Modelling the response of lechago earth and rockfill dam', *Gotéchnique* **61**, 387–407.

Alonso, E. E., Tapias, M. and Gili, J. (2013), 'Particle crushing, scale effects and delayed behaviour of rockfill: A dem investigation', Presentation at Alert Workshop. Degradation in geomaterials. Aussois, France.

Alonso, E., Tapias, M. and Gili, J. (1977), 'Scale effects in rockfill behaviour', *Géotechnique Letter* **2**, 155–160.

Atkinson, B. K. and Meredith, P. G. (1984), 'Subcritical crack growth in geological materials', *J. Geophys. Res* **89**(No. B6), 4077–4114.

Bigras, A. and Tournier, J. (2000), Construction du barrage sainte-marguerite-3, *in* 'Proceedings of the 53rd Canadian Geotechnical Conference: Geotechnical engineering at the dawn of the 3rd millennium', Canadian Geotechnical Society, Montreal, QC, Canada, pp. 239–246.

Cardoso, R. and Alonso, E. (2010), 'Behavior of materials for earth and rockfill dams: Perspective from unsaturated soil mechanics', *Frontiers of Architecture and Civil Engineering in China* **4**(1), 1–39.

Charles, R. J. (1958), 'Static fatique of glass', *J. Appl. Phys.* **29**(11), 1549–1560.

Code_Bright (2015), *A 3D program for thermo-hydro-mechanical analysis in geological media*, 5.2 edn, Department of Geotechnical Engineering and Geo-Sciences of the Polytechnic University of Catalonia (UPC), https://www.etcg.upc.edu/recerca/webs/code_bright/code_bright.

Coll, A., Ribó, R., Pasenau, M., Escolano, E., Perez, J., Melendo, A., Monros, A. and Gárate, J. (2016), *GiD v.12 User Manual*, 12 edn, CIMNE, Barcelona, Spain.

Cristian, J. N. G. (2011), Mechanical behavior of rockfill materials - Application to concrete face rockfill dams., PhD thesis, Engineering Sciences. Ecole Centrale Paris, Paris, France.

Duncan, J. M., Byrne, P., Wong, K. S. and Mabry, P. (1979), Development of lg4, study of the behavior of the lg4 dam with finite elements, Technical report, University of California, Berkley, California, USA.

Duncan, J. M. and Chang, K. S. (1970), 'Nonlinear analysis of stress and strain in soils', *Journal of the Soil Mechanics and Foundations Division* **96**, 1629–1653.

Duncan, J., Wong, K. and Ozawa, Y. (1980), *FEADAM: A computer program for finite element analysis of dams, Users Manual*, College of Engineering, University of California, Berkley, California, USA.

Errecalde, I. A. (2012), Modelling the SM-3 dam, Québec, Canada, Master's thesis, Polytechnic University of Catalonia, Barcelona, Spain.

Hammamjil, Y. (2003), Rapport synthese de comportement amenagement sainte-marguerite-3 barrage denis-perron, Technical report, Hydro-Québec, Québec, Canada.

Hydro-Québec (1990), Rivière sainte-marguerite énoncé d'envergure: Barrage sm 3, Note technique gt-110, contraintes et déformations, Hydro-Québec Aménagements de Centrales, Québec, QC, Canada.

Hydro-Québec (1999), 'Lamnagement hydrolectrique de la sainte-marguerite-3 en accord avec le milieu', Web Bulletin. https://web.archive.org/web/20030328200903/http://www.hydroquebec.com/sm3/documentation/pdf/SM3_bulletin_f.pdf.

Kolev, B., Taiebat, M., Lizcano, A. and Pak, A. (2016), Numerical simulation of the effect of particle breakage in rockfill dams, *in* 'Proceedings of the 69$^{\text{th}}$ Canadian Geotechnical Conference', Canadian Geotechnical Society, Vancouver, BC, Canada, p. 7 pages (Paper number 4223).

Konrad, J. M., Ctł, J. and Filionl, M. H. (2011), 'Intrinsic permeability of materials ranging from sand to rock-fill using natural air convection tests', *Canadian Geotechnial Journal* **48**, 679–690.

Lafleur, J. (1998), Projet sainte-marquerite (site sm3) échantillons de matriaux utilisés dans le noyau du barrage (zone 1)., Technical report, Centre de développement technologique (C.D.T), École Polytechnique de Montréal, Montreal, Canada.

Marachi, N. D., Chan, C. K., Seed, H. B. and Duncan, J. M. (1969), Strength and deformation characteristics of rockfill materials, Technical report, Department of Civil Engineering, University of California, Berkley, California, USA.

Michalske, T. and Freiman, S. (1982), 'A molecular interpretation of stress corrosion in silica', *Nature* **295**, 511–512.

Naylor, D. J., Maranha, J. R., Neves, E. M. and Pinto, A. A. (1997), 'A back-analysis of beliche dam', *Géotechnique* **47**(2), 221–233.

Oldecop, L. A. and Alonso, E. (2007), 'Theoretical investigation of the time-dependent behaviour of rockfill', *Géotechnique* **57**(3), 289–301.

Oldecop, L. A. and Alonso, E. E. (2001), 'A model for rockfill compressibility', *Géotechnique* **51**(2), 127–139.

Oldecop, L. A. and Alonso, E. E. (2004), 'Testing rockfill under relative humidity control', *Geotechnical Testing Journal* **27**(3), 269–278.

Oldecop, L. A. and Alonso, E. E. (2013*a*), Rockfill mechanics, *in* 'Advances in Unsaturated Soils', Taylor & Francis Group, London, UK.

Oldecop, L. A. and Alonso, E. E. (2013*b*), 'Rockfill mechanics', Presentation at First Pan–American Conference on Unsaturated Soils (UNSAT2010). Cartagena de Indias, Colombia.

Parkin, A. (1977), 'The compression of rockfill', *Australian Geomechanics Journal* **G7**(4), 33 – 39.

Péloquin, E. (2015), Call for proposalworkshop on numerical analysis for embankment and rockfill dams; verification & validation for better prediction, Technical report, Hydro-Québec, Québec, Canada.

Saboya Jr., F. and Byrne, P. (1993), 'Parameters for stress and deformation analysis of rockfill dams', *Canadian Geotechnical Journal* **30**, 690–701.

SNC-Shawinigan (1996), Aménegament hydro-élecetrique sainte-marquerite-3 site sm-3: Barrage et travaux connexes, Rapport de conception, lot 3040, Hydro-Québec, Québec, QC, Canada.

van Genuchten, M. T. (1980), 'A closed-form equation for predicting the hydraulic conductivity of unsaturated soils', *Soil science society of America journal* **44**(5), 892–898.

Vaunat, J. (2015), 'Mechanical constitutive laws, behaviour of unsaturated soils', Short Course Notes. Department of Geotechnical Engineering and Geosciences, UPC, Barcelona, Spain.

Watabe, Y., Leroueil, S. and Le Bihan, J. P. (2000), 'Influence of compaction conditions on pore-size distribution and saturated hydraulic conductivity of a glacial till', *Canadian Geotechnial Journal* **37**, 1184–1194.

Appendix A

Validation Problem – Beliche dam simulation

A.1 Problem information

The problem chosen for validation of using Code_Bright and the constitutive models successfully is the Beliche Dam. The dam is 54 m high and has a standard design: central clay core and two rockfill shells. The size of the dam is significantly smaller compared to the Denis-Perron dam and the geometry less complicated. The reason for choosing this dam is due to the numerous studies conducted on it and, in specific, the work of Alonso et al. (2005). In the study, the dam was modelled using Code_Bright and the implemented Rockfill Model (RM). The goal is to reproduce the simulation results by Alonso et al. (2005), using the calibrated material parameters from the paper and the simulation methodology.

Figure A.1 shows the layers and mesh of the performed simulation in 2005. In comparison, Figure A.2 shows the validation layers and mesh used. The material parameters used are extracted from the same paper and are summarized in Tables A.1, A.2 and A.3. The values in not available in the study from 2005 and were estimated.

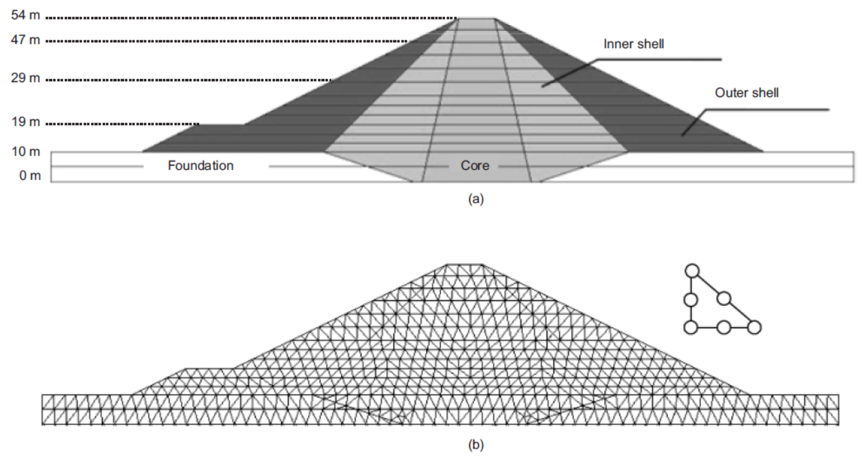

Figure A.1: (a) Simulation layers and (b) Mesh from (Alonso et al., 2005)

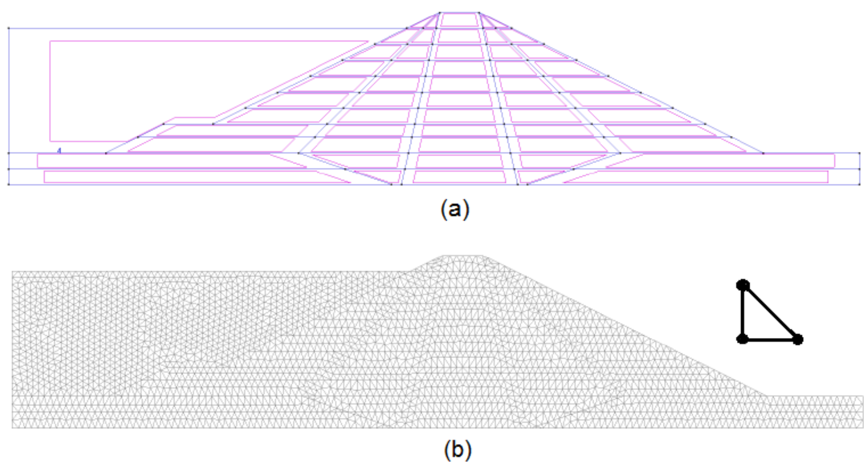

Figure A.2: (a) Simulation layers and (b) Mesh from validation problem

Table A.1: Mechanical parameters for rockfill.

Definition of Parameters	Symbol	Units	Rockfill Shoulders	
			Outer Shell	Inner Shell
Elastic behaviour				
Elastic Modulus	E	MPa	180	150
Poisson's ratio	ν	–	0.3	0.3
Plastic behaviour				
Plastic virgin instantaneous compressibility	$\lambda^i - \kappa$	MPa^{-1}	0.010	0.025
Virgin clastic compressibility for saturated conditions	λ_0^d	MPa^{-1}	0.01	0.028
Parameter describing the rate of change of clastic compressibility with total suction	α_s	–	0.003	0.01
Slope of critical-state strength envelope for dry conditions	M_{dry}	–	1.9	1.75
Slope of critical-state strength envelope for saturated conditions	M_{sat}	–	1.8	1.3
Parameter that controls the increase in cohesion with suction	k_s	–	0	0
Threshold yield mean stress for the onset of clastic phenomena	p_y	MPa	0.01	0.01
Parameter that defines the non-associativeness of plastic potential	α	–	0.3	0.3
Creep				
Creep coefficient for saturated conditions	μ	MPa^{-1}	0.0012	0.0012
Parameter that controls the influence of suction on creep rate	β^c	–	0.083	0.083
Viscoplasticity				
Fluidity parameter	Γ	s^{-1}	100	100
Flow function exponent	N	–	5	5

Table A.2: Mechanical parameters for the till core.

Definition of parameter	Symbol	Units	Value
Elastic behaviour			
Elastic modulus	E	MPa	100
Poissons ratio	ν	–	0.4
Plastic behaviour			
Virgin compressibility for saturated conditions	$\lambda(0)-\kappa$	MPa^{-1}	0.02
Parameter that establishes the minimum value of the compressibility coefficient for high values of suction	r	–	0.7
Parameter that controls the rate of increase in stiffness with suction	β	MPa^{-1}	1.2
Reference stress	p_c	MPa	0.02
Slope of critical-state strength line	M	–	0.88
Parameter that controls the increase in cohesion with suction	k_s	–	0.1
Parameter that defines the non-associativeness of plastic potential	α	–	0.3
Viscoplasticity			
Fluidity parameter	Γ	s^{-1}	1000
Flow function exponent	N	-	6

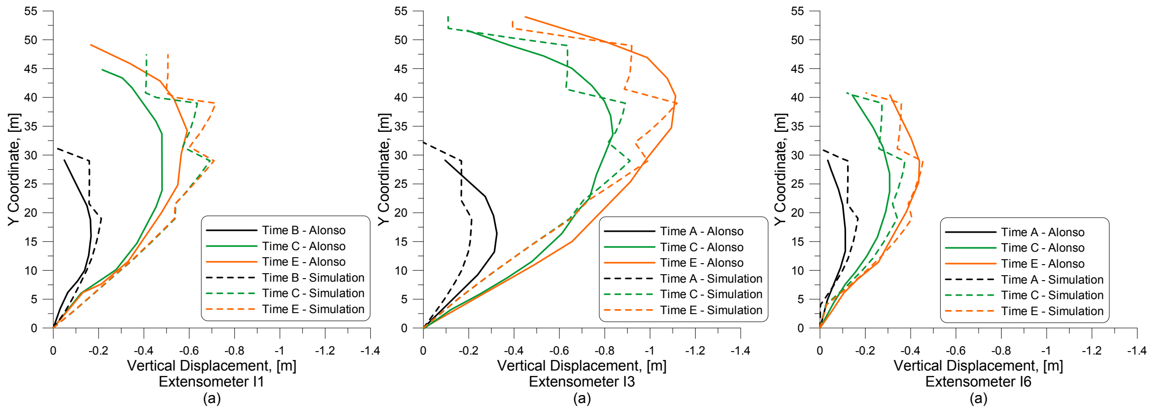

Figure A.3: Vertical displacements at position for extensometers (a) I1, (b) I3 and (c) I6 for construction stages [A] to [E]. Validation simulation results and computed results from Alonso et al. (2005)

Table A.3: Hydraulic parameters for rockfill, till core and foundation

Definition of parameter	Symbol	Units	Value		
			Rockfill	Till Core	Foundation
Intrinsic Permeability	k	m^2	2×10^{-11}	8×10^{-15}	3×10^{-12}
Water Retention Curve (Van Genuchten, 1980)					
Pressure at $T = 20°$	P_0	MPa	0.01	0.5	0.01
Maximum Saturation	S_{ls}	–	1	1	1
Residual Saturation	S_{lr}	–	0	0	0
Exponent Defining Curve Shape	λ	–	0.6	0.27	0.3
Initial Suction (applied as an initial condition to model)	s_0	MPa	20	0.5	0

A.2 Simulation results comparison

Two figures have been chosen to be reproduced from the paper of 2005. The first one is Figure 20, showing vertical settlements for extensometers in the upstream rockfill (I1), the core (I3) and the downstream rockfill (I6). The results are compared in Figure A.3. Time [A] to [E] are defined below.

A Construction to elevation 29 m (t=0-180 days)

B Construction to elevation 47 m (t=180-360 days)

C Impounding of the reservoir to elevation 29m (t=360-420 days)

D Completion of construction to elevation 55 m (t=420-450 days)

E Impounding of reservoir to elevation 49 m (t=450-1500 days)

The results for extensometer I1 in the dry rockfill over-predicts the settlements for times [A] and [C]. This is probably due to the difference in the retention curves used, generating more compressibility of the rockfill in the impounding stage. At time [E], the two simulations match well because the rockfill material is fully saturated. At full saturation the compressibility is at its maximum, $\lambda_i + \lambda_0^d$, because the suction $s = 0$ and the water retention curve does not have any effect. For extensometer I3, the differences for times [A] and [C] probably come from the layer thickness'.

The second figure chosen is Figure 22 (a) from the work of Alonso et al. (2005). It is chosen in order to monitor if the stress prediction of the two simulations match along a horizontal cut 13 m above the boundary of the model. Figure 22 (a) reproduced for times [A], [B] and [E]. The comparison in results can be seen on Figure A.4.

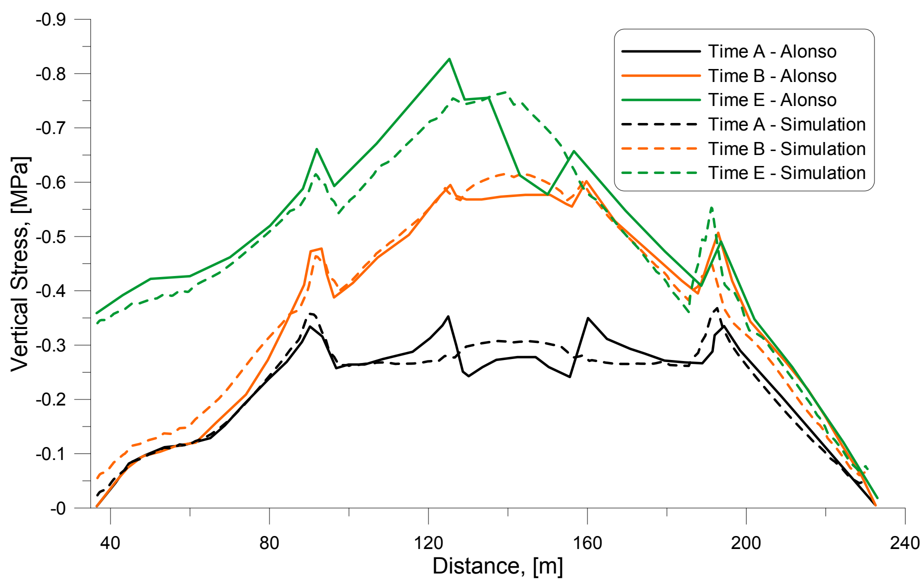

Figure A.4: Validation simulation and simulation results from Alonso et al. (2005) of vertical stresses for stages [A], [B] and [E] on a horizontal plane at elevation 13 m above boundary of clay core.

The shape of the stress plot is illustrated effectively and the differences come from the discretization and layering of the model. The abrupt transitions captured by the model come from the change in materials and the collapse of the rockfill and are captured by the validation simulation. Generally, the results are satisfactory and bring a level of confidence in the use of the software and its features to begin modelling the response of the Denis-Perron dam.

A.3 Simulation method differences

There were a few differences in the simulation methodology that cause deviations in the results. These are listed below.

- Geometry and layering differences. Precise CAD drawings or coordinates of the dam are not available and therefore are estimated. The numerical model layers in Alonso et al. (2005) are smaller than the ones represented. This could cause a difference in the stress and therefore the settlements. This can be seen from the comparison of Figures A.1 (a) and A.2 (a)

- Reproducing the same mesh is not possible. The two meshes can be seen on Figures A.1 (b) and A.2 (b)

- Way of simulating impoundment. In the current version of Code_Bright, a simpler and more effective way of simulating reservoir filling is available. The method is by simulating the water as a material with linear elastic properties. Details of this method can be found in Chapter 4. In 2005, the way of simulating water impoundment is by applying the water pressure variations on the surface of the dam.

- Some missing material parameters. In particular, the exact parameters for the water retention curves for both the core and the rockfill are not available. The BBM and RM models are sensitive to the water retention curves, because they govern the liquid pressure determinations, which results in changes of the compressibility of the materials, especially in the rockfill. The water retention curves in the current problem are reproduced using the Van Genuchten model and the water retention curves are approximated.

- Some missing constitutive model parameters for the till core. In particular, the fluidity parameter Γ for the till core is not available.

Appendix B

Rockfill mechanics

This appendix aims to summarize some of the key components of rockfill response, that are incorporated in the constitutive model following. The appendix begins with observations made exploring field and laboratory data, followed by an analysis of the rockfill response from a fracture mechanics perspective. After that, the key mechanism known as particle breakage and key factors affecting it are presented. Finally, testing apparatus and techniques used in laboratory setting are explored.

B.1 Field and laboratory observations

Due to the rockfill's "free draining" nature, it remains in an unsaturated or partially saturated state unless fully submerged in water (Oldecop and Alonso, 2013*a*). Partial saturation can occur due to multiple reasons with the most common being interaction with the atmosphere, i.e. rainfall. Water action has a significant effect on the behaviour of rockfill according to Parkin (1977),Atkinson and Meredith (1984) and Oldecop and Alonso (2004). However, the nature of the effect differs from the one in unsaturated soils. The influence of water on rockfill behaviour is physiochemical, rather than purely mechanical (Oldecop and Alonso, 2013*a*).

To establish the differences between rockfill and unsaturated soils, first the definition of suction has to be defined. For unsaturated soils, the suction, s, has a definite mechanical meaning and is identified with the matric component of suction. In the case of rockfill, suction is identified with the total suction, which governs the speed of crack propagation (Alonso et al., 2005). The clear distinction between the two definitions can be seen in Figure B.1. Figure B.1 (a) conveys a particle of a low-plasticity soil, where the suction acts in the inter-particle space; whereas Figure B.1 (b) shows a rockfill particle with a crack, where the suction acts at the tip of the crack of the particle.

The terms relative humidity and suction have been used interchangeably in the body of this thesis.

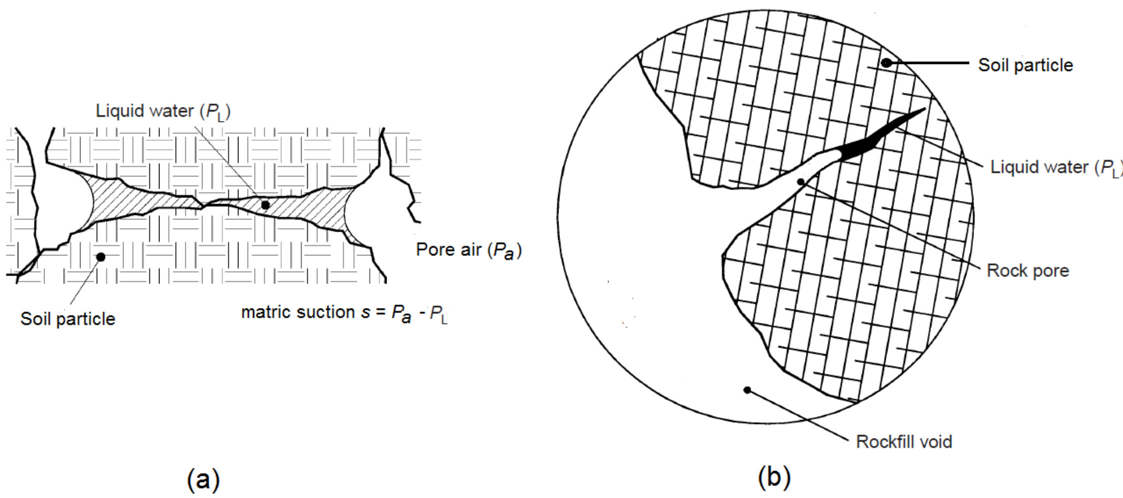

Figure B.1: (a) Particles of an unsaturated low-plasticity soil, adopted from Oldecop and Alonso (2004) (b) Rockfill particle with a crack (pore), modified from Oldecop and Alonso (2001).

They are related through a psychrometric relationship defined by Oldecop and Alonso (2004) as

$$RT\,Ln(\mathbf{RH}) = -vs \tag{B.1}$$

where R is the gas constant, T is the absolute temperature, v is the molar volume of water and s is the total suction. Figure B.2 shows an idealised particle with a crack in the middle. Each rockfill particle hosts multiple defects of different size and orientation, such as the one showed. When applying stress to a particle, the crack tip acts as a stress concentration zone and could begin to propagate due to different factors. Oldecop and Alonso (2013*a*) provides an insight from a fracture mechanics point of view and interprets existing laboratory data based on this.

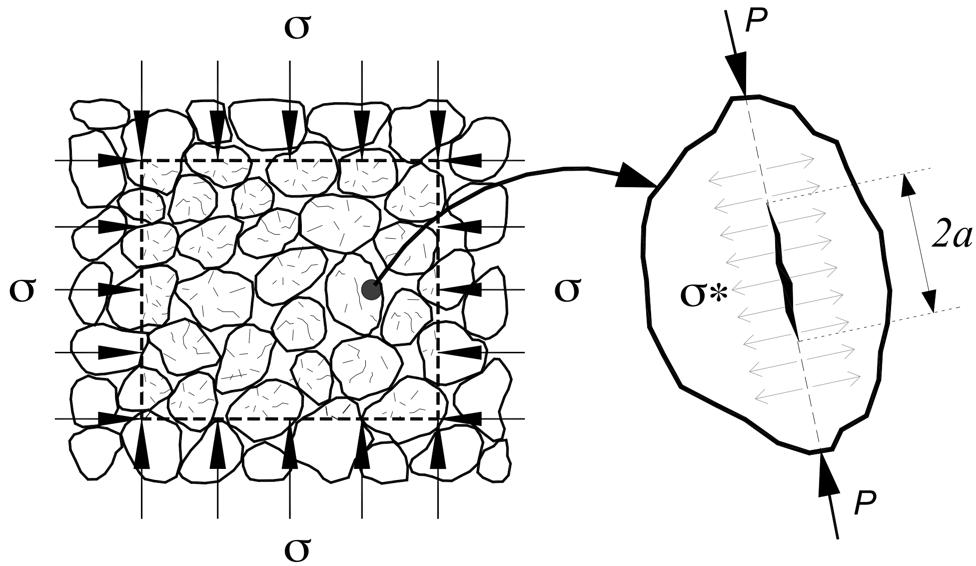

Figure B.2: Sketch of a simplified volume of rockfill and a rockfill particle containing a crack that eventually propagates and causes particle breakage. Modified from Oldecop and Alonso (2013*a*).

A crack develops under a uniform tensile stress field of magnitude σ^* and propagates at a high speed, when the stress intensity factor K reaches a threshold value known as the fracture toughness of the material K_c. Linear elastic fracture mechanics applies for this type of failure and therefore could be defined as

$$K = K_c = \sigma^* \beta \sqrt{\pi a} \tag{B.2}$$

where β depends on the particle geometry and a a is the crack length. Figure B.3 presents a plot of crack propagation velocity varying with both relative humidity and the stress intensity factor. Figure B.3 is divided into three regions. In region three, the $K > K_c$ causes immediate breakage of the particle in a catastrophic manner. This region is responsible for deformations occurring right after load applications. Cracks in region two grow simultaneously due to increase in relative humidity and increase in the cracks length.

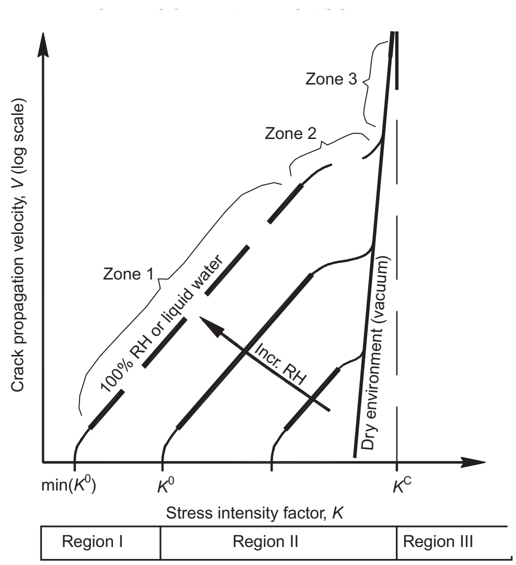

Figure B.3: Typical stress intensity curve. Modified from Oldecop and Alonso (2007).

This region is usually referred to as "subcritical crack propagation" region. As the crack increases in size, it starts increasing the propagation velocity and begins approaching region three, where eventually the particle breaks. This breakage is responsible for the time dependent deformations in rockfill and is determined by relative humidity (or total suction) and the stress level. Increasing of moisture content under a constant rate would also increase the crack propagation velocity, hence it is responsible for the "creep" effect in rockfill. More details for the "creep" effect are explored in Chapter 6. In region one, $K < K_0$, no propagation occurs.

The increase of crack propagation velocity has been established to depend on the relative humidity. The physiochemical phenomenon causing this effect is known as stress corrosion. The process begins by a water molecule entering the tip of the crack in the form of vapour or liquid as shown on Figure B.4 (a).

Then, water reacts with the strained silicium bond at the crack tip (Figure B.4 (b), 1). After the reaction, the bond is weakened (Figure B.4 (b), 2) and under the applied load it finally breaks (Figure B.4 (b), 3).

Water content and stress levels are the most significant factors affecting the breaking of particles through a crack propagation mechanism. However, there are other factors that influence the breaking of particles and they are explored in the next section.

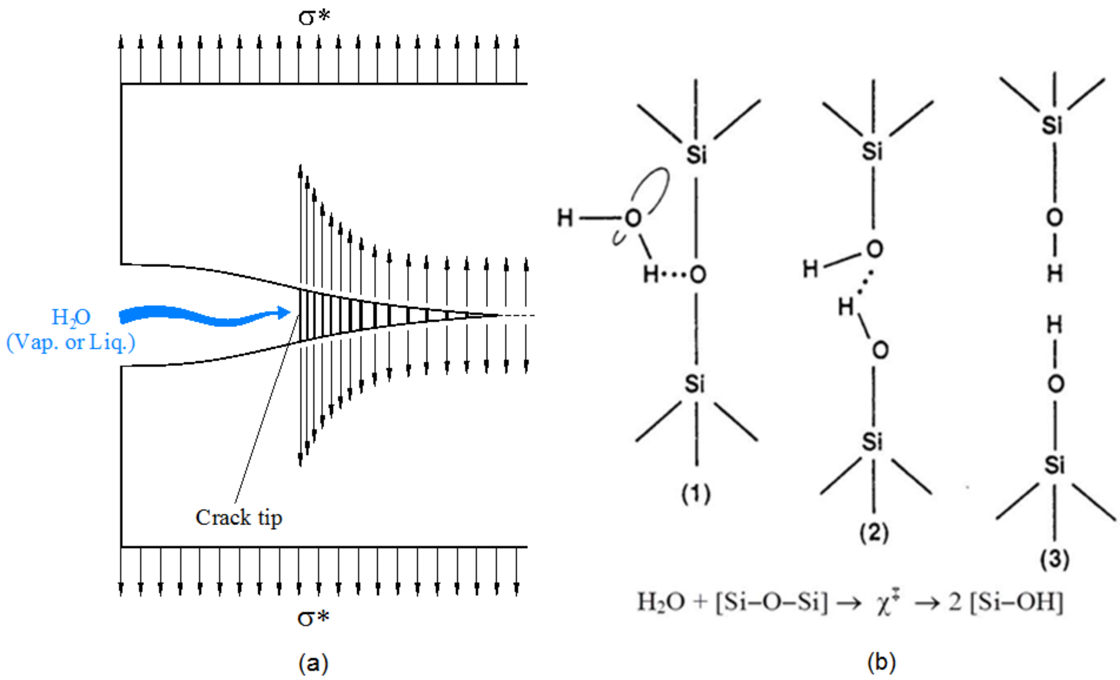

Figure B.4: (a) Water vapour entering an idealised crack, modified from Oldecop and Alonso (2013*b*) (b) Reaction between a water molecule and a strained silicium dioxide molecule. Modified from Michalske and Freiman (1982).

B.2 Particle breakage

Cristian (2011) summarized all the factors affecting particle breakage. They are divided into three general categories *i*) factors connected to the particles *ii*) factors connected to the particle assembly *iii*) factors connected to conditions.

Particle mineral composition

The influence of the mineral composition is related to the strength of the particle and thus the amount of breakage. Researchers like Marachi et al. (1969) and Atkinson and Meredith (1984) have conducted tests on different geological materials. Atkinson and Meredith (1984) found that silicates' particle breakage increases as their environment becomes depleted in hyroxyl species. On the other hand, quarts tends to experience low amount of cracking in basic environments and basalt experiences higher cracking in moist air.

Particle shape

The second factor related to the particles is the shape of the particles. Generally, angular particles experience higher amounts of breakage compared to rounded ones. This is because the angular edges serve as stress concentration zones and tend to break at contact. Figure B.5 shows a particle split in two with one failure surface and some crushing at the contact zones.

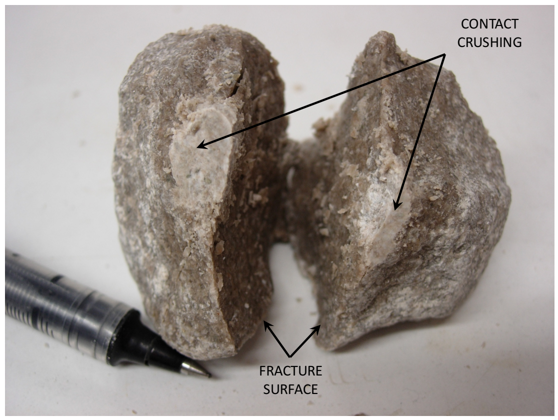

Figure B.5: Rockfill particle with contact crushing zone and a single fracture surface, Alonso et al. (2013).

Particle size

The final factor related to the particles is the size of the particle. This has been reported by Alonso et al. (1977), among others. The reason for this effect lies in the statistical distribution of flaws within the particle. Therefore, for the same material with a homogeneous distribution of flaws, particles with bigger diameters have more defects compared to smaller ones. This results in particles breaking under lower tensile stress. Figure B.6 shows the reduction in failure stress σ_f with the increase of the particle size diameter d_N for different materials tested. This phenomenon is examined more thoroughly in Chapter 6.

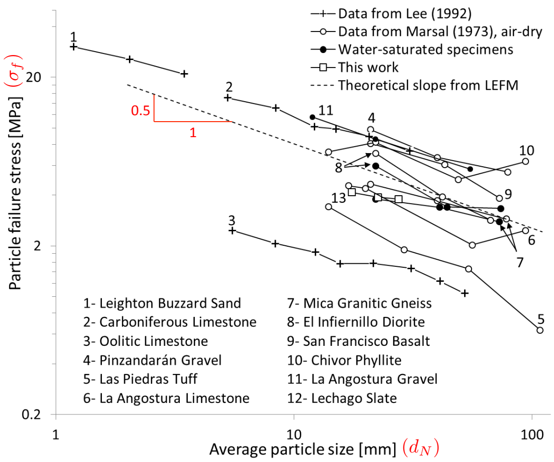

Figure B.6: Rockfill particle with contact crushing zone and a single fracture surface, Alonso et al. (2013).

Gradation

The first factor related to the assembly of the particles is their gradation. Cristian (2011) summarize shear strength data relating the coefficient of uniformity $C_u = D_{60}/D_{10}$ and the breakage factor B defined as

$$B = \frac{1}{2}\int_{D_M}^{D_m} |f_0(D) - f_f(D)| dD \tag{B.3}$$

where $f_0(D)$ and $f_f(D)$ are the initial and post-test retained mass for a given sieve of size D. The factor B is commonly used in soil mechanics practice for characterizing the amount of crushing of granular materials. The plot of C_u versus B is shown on Figure B.7 and exhibits lower amounts of crushing for higher values of C_u, or in other words for well graded soils. This could be explained by observation of stress chains in the soils. Well graded soils have identical stress states and upon breakage, the stress redistribution causes other particles with similar size to experience a higher amount of stress and thus cause additional breakage.

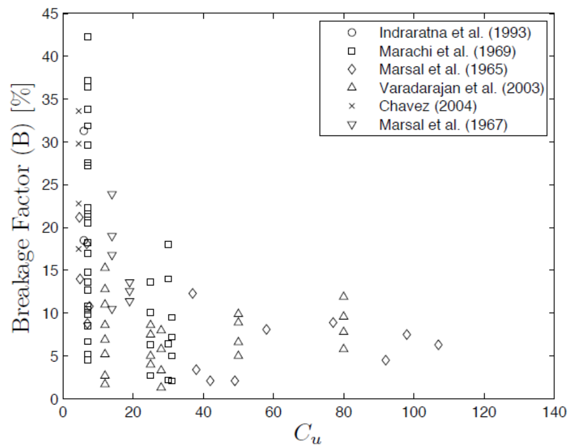

Figure B.7: Variation of breakage index with change of the coefficient of uniformity, adapted from Cristian (2011).

Compaction

Compaction of particles with same diameters but different initial void ratios experience the same amount of breakage but under different amounts of stress. Higher void ratios causes breakage under smaller stresses and lower void ratios at higher stresses. According to Cristian (2011) eventually, after applying sufficient amount of stress, both samples tend to reach the same void ratios. Another observation by Oldecop and Alonso (2013*a*) is that void ratio plays a part in determining the amount of compressibility experienced by larger particles. Quantification of this effect is explored in Chapter 6.

Water content

Moisture content (relative humidity) affects the speed of crack propagation and is one of the most significant factors governing particle breakage, as already discussed.

Stress level

Naturally, higher stress levels tend to increase the breakage of particles. The breakage coefficient *B* is observed to increase with higher stress levels as stated by Cristian (2011).

Time dependency and "creep"

The two dominant mechanisms governing rockfill response are particle re-arrangement and particle breakage. Particle re-arrangement occurs when particles roll and slide past each other, causing immediate strain increments upon loading. Particle breakage, on the other hand, is a delayed mechanism. This time-dependency is a result the stress corrosion mechanism, which is observed by many researchers to depend on time. In the works of Oldecop and Alonso (2007), data of long term oedometer tests performed under different suction and stress conditions confirm the observations in the field.

The "creep" in rockfill refers to the gradual propagation of cracks causing small strain increments, which is considered as a long time dependent process. This behaviour is different from the conventional definition of creep, where water is expelled from the soil over a long period of time due to higher permeability of soils.

Researchers like Oldecop and Alonso (2007) suggest that the time dependent strain follows a linear relationship in logarithmic space. Those observations are based on field settlement records of multiple rockfill dams. In the constitutive formulation of the RM, an expression is suggested to capture the behaviour observed in both the field and laboratory oedometer tests. The logarithmic deformation equation suggests an indefinite accumulation of settlement of the rockfill. Such behaviour may seem odd from a physical point of view, but observing the data of rockfill dam settlements, shown on Figure 1.1 for more than forty years of operation, communicates the same. Due to the crack propagation nature of the "creep" mechanism, it is natural that the behaviour is dependent on the suction within the cracks. Therefore, the compressibility λ^t associated with the "creep" strains is dependent on suction. Lower suction causes a faster rate of λ^t increase with stress as suggested by Oldecop and Alonso (2013*a*).

Figure B.8 (a) shows the dependency of the time dependent parameter λ^t with suction and applied stress for compacted gravel of a quartzitic shale.

It has been also established that during the two stages of rockfill response, clastic yielding and clastic hardening, the parameter λ^t is proportional to the conventional compressibility λ as shown below

$$\frac{\lambda^t}{\lambda} \cong \frac{1}{n} \tag{B.4}$$

where n is parameter in Charles law (Charles, 1958) that describes the crack propagation velocity associated with the stress corrosion effect. The test results from Figure B.8 (a) were re-plotted as λ^t vs λ and two envelopes were plotted with higher bound for $n = 20$ and lower bound $n = 200$.

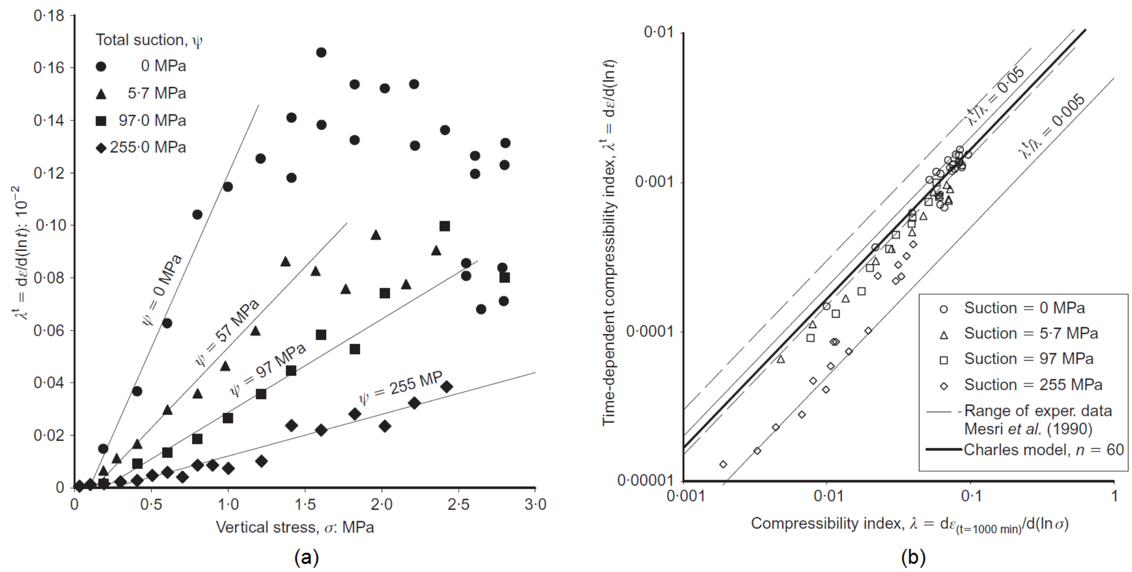

Figure B.8: (a) Time-dependent compressibility index against applied stress for different constant suction values (b) Correlation between time-dependent compressibility index and compressibility index for tested rockfill. Adopted from Oldecop and Alonso (2007).

Atkinson and Meredith (1984) summarize experimental data for variety of rocks, showing the change of the subcritical crack growth index n and its variability with relative humidity. For the quartzitic shale, the best fit to the data is reached for $n = 60$ as seen on Figure B.8 (b). This is congruent with the findings of Atkinson for this type of rock.

As mentioned, the time dependent parameter λ^t is dependent on time, applied pressure, compressibility of the material and suction. The parameter varies linearly with applied vertical stress up to stresses of 1 MPa. Additionally, there is a linear dependence of the parameter with suction in natural logarithmic space.

B.3 Testing apparatus

As previously mentioned, relative humidity within the rockfill cracks is one of the governing factors dictating the amount of breakage that occurs upon loading. Determination of rockfill response requires three laboratory tests.

The first test determines the relation between the relative humidity and the suction within the cracks. In unsaturated soils (and rockfill), this is known as a water retention curve and is a fundamental material property. In the case of rockfill, determining this requires three different approaches depending on the level of suction. For high suctions, usually up to 250 MPa, a vapour equilibrium technique is used, and the rock sample is stored in an isolated container, where the relative humidity (RH) is controlled by saturated saline solution. For the low-suction range, initially a ceramic suction plate is used to apply a negative water pressure in the pores, also known as the "tensiometer technique". After this, the final stage is the "axis translation technique", where an air overpressure is applied to the rock sample (Oldecop and Alonso, 2001). This water retention curve establishes the basis of connecting the microscopic response to a global problem, such a dam.

The second test is a RH controlled oedometer test, where the sample is compressed at different levels of relative humidity (suction). The device works in a similar way as the one for determining the water retention curve. An air flow with a controlled amount of relative humidity percolates through the rockfill pores and different levels of stress is applied. The device can be seen on Figure B.9.

The third tests is performed with the same suction controlled oedometer device, with the difference that the volumetric strains are measured under a constant load over a period of 0 - 1000 minutes to establish the time-dependent behaviour of the rockfill. This test is performed under different levels of stress and different levels of relative humidity, because the "creep" effect is dependent on both stress and suction.

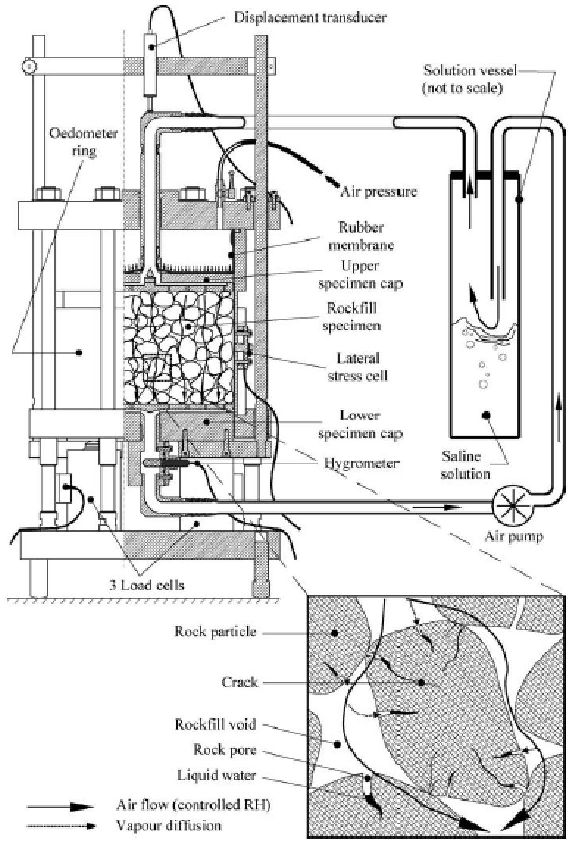

Figure B.9: Relative humidity (RH) controlled oedometer test and water transport scheme circulation inside rockfill particle, adopted from Oldecop and Alonso (2004).